$(Ga_{1-x}Zn_x)(N_{1-x}O_x)$ Nanocrystals: Photochemical H_2 Production and Spatial Characterization of Electronic Structure

by

Leah Margaret Graham Hall

B.S., University of Montana, 2014

A thesis submitted to the

Faculty of the Graduate School of the

University of Colorado in partial fulfillment

of the requirement for the degree of

Doctor of Philosophy

Department of Chemistry and Biochemistry

2019

This thesis entitled:

$(Ga_{1-x}Zn_x)(N_{1-x}O_x)$ Nanocrystals: Photochemical H_2 Production and Spatial Characterization of Electronic Structure

written by Leah Margaret Graham Hall

has been approved for the Department of Chemistry and Biochemistry by:

____
Gordana Dukovic

____
Sadegh Yazdi

Date __________________

The final copy of this thesis has been examined by the signatories, and we find that both the content and the form meet acceptable presentation standards of scholarly work in the above mentioned discipline.

Hall, Leah Margaret Graham (Ph.D., Chemistry)

$(Ga_{1-x}Zn_x)(N_{1-x}O_x)$ Nanocrystals: Photochemical H_2 Production and Spatial Characterization of Electronic Structure

Thesis directed by Associate Professor Gordana Dukovic

Solar fuel generation via artificial photosynthesis is a promising pathway to a clean and sustainable source of energy. Nanoscale $(Ga_{1-x}Zn_x)(N_{1-x}O_x)$ has been synthesized in the solid state in order to answer the call for new multinary semiconductors for use in solar fuel generation. Herein, the solid-state mechanism of $(Ga_{1-x}Zn_x)(N_{1-x}O_x)$ nanocrystal formation involving phase transformation of cubic spinel $ZnGa_2O_4$ to wurtzite $(Ga_{1-x}Zn_x)(N_{1-x}O_x)$ and diffusion of the elements combined with nitrogen incorporation will be discussed. Understanding how multinary semiconductor compounds function and drive multi-electron photochemical reactions is of the utmost importance for potentially using them in solar applications. One goal is to utilize $(Ga_{1-x}Zn_x)(N_{1-x}O_x)$ nanocrystals for solar photochemistry and understand why their efficiencies have been historically low. The use of $(Ga_{1-x}Zn_x)(N_{1-x}O_x)$ nanocrystals for photochemical H_2 generation in an aqueous system with a redox mediator will be discussed. The four-part H_2 generation system uses $(Ga_{1-x}Zn_x)(N_{1-x}O_x)$ nanocrystals as a light absorber, methyl viologen as an electron relay, Pt nanoparticles as a cocatalyst, and dithioerythritol as a sacrificial hole scavenger. Each charge-transfer step is studied in isolation in order to evaluate the factors that determine the overall photochemical efficiency. It is concluded that electron transfer from $(Ga_{1-x}Zn_x)(N_{1-x}O_x)$ to MV^{2+} is likely the most limiting step for the overall system. To date, little analysis has been done on the electronic structure of $(Ga_{1-x}Zn_x)(N_{1-x}O_x)$, particularly for samples with different elemental distributions. How the electronic structure changes when comparing homogeneous and heterogeneous $(\mathrm{Ga}_{1-x}\mathrm{Zn}_x)(\mathrm{N}_{1-x}\mathrm{O}_x)$ nanocrystals and how the electronic structure changes spatially throughout a single particle will be investigated. It is found that the heterogeneous $(\mathrm{Ga}_{1-x}\mathrm{Zn}_x)(\mathrm{N}_{1-x}\mathrm{O}_x)$ nanocrystals show two energy transitions, one in the UV region and one in the visible region, while the homogeneous particles only show a visible transition. Additionally, the shape of the energy loss spectrum stays constant throughout a particle indicating that the electronic structure is constant in a single particle.

Acknowledgements

Throughout writing this dissertation, I have had the privilege of reflecting on the people that have helped me down this path and supported me unconditionally. The difficulties and challenges faced during this journey have only served to highlight the amazing group of people who have been my support system. To my family, friends, and colleagues, thank you for your unyielding support over the years. I know this hasn’t been an easy journey for me or for you. I will always be tremendously grateful for your loving support.

I would like to thank Professor Chris Palmer and Dr. Jesse Hyslop for opening my eyes to the wonderful world of research. Chris and Jesse, you are both incredible advisors and mentors, thank you for making my time at the University of Montana so extraordinarily enjoyable and for inspiring me to pursue a PhD. Your kind encouragement and unwavering support over the years have meant the world to me.

To my family, Mom, Dad, Matthew, and Aunt Sue, thank you for keeping me sane, for making sure I took the time to enjoy life, for the epic Christmases, and for always being there for me. To my legendary friends, Aroob, Otha, Ivane, and Erin, thank you for being my soulmates, for understanding me on a level I never thought was possible, for taking care of me, and for bringing joy into my life.

All of this work would not have been possible without my brilliant, awesome, hilarious, wonderful research group. Thank you to my advisor Prof. Gordana Dukovic and to all Dukovic Group members past and present. Dr. Hayden Hamby, you were the most amazing mentor. You taught me how to be an independent researcher, you gave me the confidence to believe in myself, and without you none of this would have been possible. Thank you for being a wonderful friend and my mentor when I needed it the most. Prof. Pornthip Tongying, you are such a brilliant and inspiring scientist. You were an exceptional role model and I am so lucky to have had you as a postdoc to look up to. Thank you for teaching me so much and being a joy to work with. Marta Sulima, my partner from the very beginning until the very end, I can't believe we're done! Thank you for being my partner in crime throughout this crazy experience, it was a pleasure to share this with you and to grow with you as a friend and as a scientist. A huge thank you goes to Dr. Orion Pearce for helping me through my PhD journey, but especially at the end when I needed help with my dissertation. Orion, thank you for all of the coffee trips and for helping me get through this dissertation experience, you were incredibly helpful and inspirational. Kristina Vrouwenvelder, thank you for being a wonderful friend, colleague, and confidant. Your writing and editing skills are unparalleled and I can't thank you enough for all the help you've given me over the years. Dr. Amanda Grennell, Dr. James Utterback, Jesse Ruzicka, Helena Keller, Lauren Pellows, and Madison Jilek, thank you for always being willing to chat with me and discuss life, I will miss our daily conversations immensely. Shelby Beer, Nicholas Pogranichniy, Ben Hohman, Prof. Kyle Schnitzenbaumer, Prof. Molly Wilker, Dr. Kyureon Lee, Dr. Katherine Shinopoulos, Dr. Yinggang Lu, Dr. Chi-Hung Chuang, and Dr. Tais Labrador, thank you for being outstanding group members and creating a fun and innovative working environment.

It was a pleasure to have the opportunity to collaborate with Prof. Sadegh Yazdi, Prof. Mathias Weber, and Curtis Beimborn. Thank you for the chance to expand my horizons and learn exciting new science. Thank you to Dr. Nate Neale for giving me the opportunity to use the instrumentation at NREL. Lastly, thank you to the sources of funding that allowed me to do this research: the Arnold and Mabel Beckman Foundation, the University of Colorado Boulder, and U.S. Department of Education Graduate Assistantship in Areas of National Need program.

Contents

Figures

Chapter 1: Introduction

1.1 Motivation

1.1.1 Solar Fuel Production

As overpopulation and a lack of sufficient natural resources are a growing problem, the need for clean and renewable energy is increasing. Humans rely mainly on fossil fuels to power their lives, from cars and household power to the production of meat and plastics. However, in recent years technological strides have made solar energy and other renewable and sustainable forms of energy generation more feasible. With the population on Earth growing exponentially, it is incredibly important to support renewable energy research so that we can stop relying on the Earth's finite resources and start relying on sustainable resources like the sun. In order to accomplish this, it is necessary to make technological advances and continue researching renewable energy.[1]

One promising direction that scientists are investigating that uses the sun's energy to produce power is artificial photosynthesis to produce solar fuels. Solar fuel production generally relies on the Sun's light energy to drive a chemical reaction, producing a useable fuel. One of the most popular fuels is hydrogen gas (H_2). H_2 is an excellent fuel source because the only chemical byproduct of the combustion of hydrogen and oxygen is water.[2] Most other fuels produce some kind of hydrocarbon or carbon dioxide upon combustion; these byproducts can have unwanted consequences when released, such as pollution and the greenhouse gas effect. H_2 is usually produced by water splitting, where a molecule of water is split into H_2 and O_2. There are a variety of different methods to do this reaction, but almost all use energy in the form of electric current or sunlight to split water molecules into H_2 and O_2. The two gas products can then be separated and H_2 used as a fuel.

One popular scheme used to perform water splitting is to use a semiconductor material which can serve a reaction site for the water reduction and water oxidation reactions, lowering the barrier to the reaction.[2-3] However, the conduction band (CB) and valence band (VB) of the semiconductor material must be at the proper energy levels in order to participate in the water oxidation and reduction reactions, and to find a semiconductor whose bands align for both reactions is rare. Figure 1.1, from reference 4, shows two possible configurations for a photocatalytic H_2 production system. The first shows a single light absorber with CB and VB aligned so that they span both the water oxidation and reduction reactions. The other configuration shows a two-part photocatalytic system using two separate light absorbers, one with bands that are only aligned for the water oxidation reaction and one with bands that are only aligned for the water reduction reaction.[4] The importance of band alignment for water splitting has led to a large body of research dedicated to synthesizing materials with or altering materials to have ideal band alignments for water splitting.[2-3, 5-15]

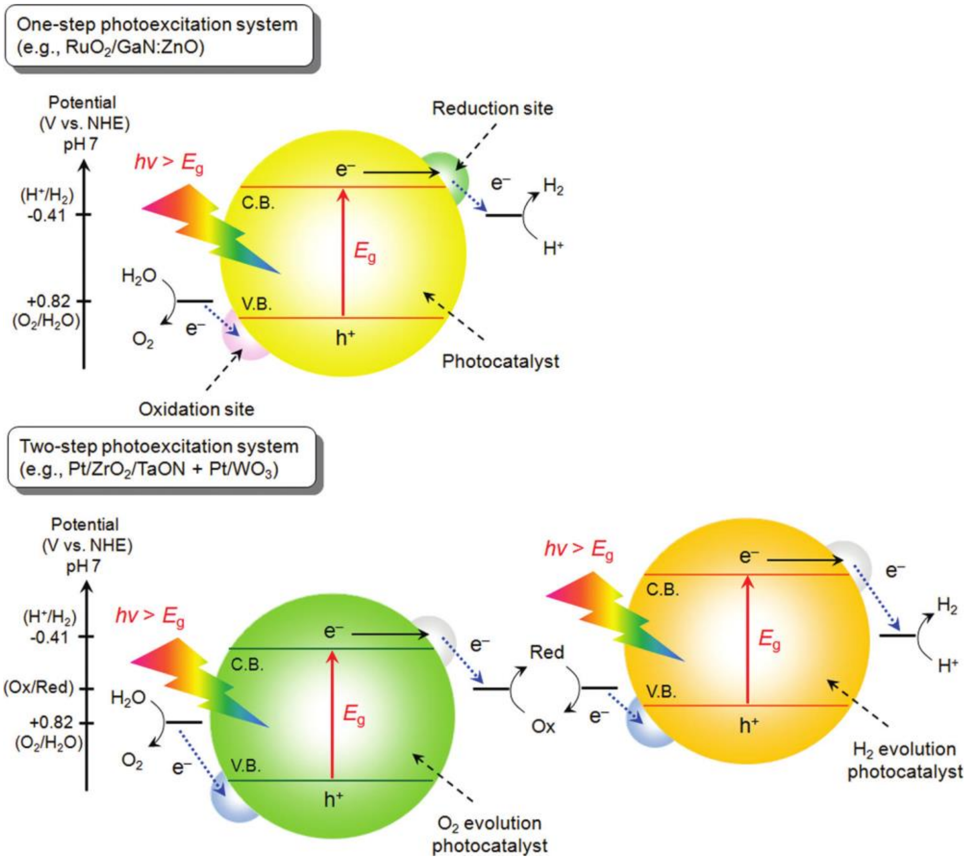

Figure 1.1: Energy diagrams showing two different photocatalytic H_2 production schemes, a one-step and a two-step photocatalytic system. C.B. indicates the conduction band, V.B. the valence band, and E_g the band gap. From reference 4.

1.2 Background

1.2.1 $(Ga_{1-x}Zn_x)(N_{1-x}O_x)$ Nanocrystals

One semiconductor that has been proposed for water splitting is Gallium Zinc Oxynitride, $(Ga_{1-x}Zn_x)(N_{1-x}O_x)$.[16] Oxynitride materials are useful for photocatalysis because oxides are resistant to oxidation while nitrides absorb in the visible region. Mixing an oxide and a nitride together has the potential to benefit from both the stability characteristics of oxides and the visible absorption characteristics of nitrides. [15, 17-18] $(Ga_{1-x}Zn_x)(N_{1-x}O_x)$ is a semiconductor that is a solid solution of GaN and ZnO. It has a wurtzite crystal structure, can be made at the nanoscale, and can have the amounts of GaN and ZnO in the material tuned to different ratios.[19] As $(Ga_{1-x}Zn_x)(N_{1-x}O_x)$ is a solid solution, its atoms all exist in the same crystal lattice without any phase differences. Since the Domen group's first successful synthesis of bulk $(Ga_{1-x}Zn_x)(N_{1-x}O_x)$ in 2005,[16] many researchers have published various methods of $(Ga_{1-x}Zn_x)(N_{1-x}O_x)$ bulk synthesis and nanoscale synthesis.[16, 20-29]

In addition to the synthesis of $(Ga_{1-x}Zn_x)(N_{1-x}O_x)$, researchers have also investigated the photochemical and water splitting potential of $(Ga_{1-x}Zn_x)(N_{1-x}O_x)$, including the Domen group.[9, 30-35] A common use for $(Ga_{1-x}Zn_x)(N_{1-x}O_x)$ today is as a light absorber for photochemical H_2 generation, often through proton reduction instead of water splitting.[18, 27, 36-38] Many researchers have used bulk $(Ga_{1-x}Zn_x)(N_{1-x}O_x)$ for photochemical H_2 production;[24, 27, 30, 34, 39-40] however, nanoscale $(Ga_{1-x}Zn_x)(N_{1-x}O_x)$ was of great interest for these applications, since nanoparticles tend to exhibit more reactivity and a higher surface-to-volume ratio than bulk materials.

With the goal of exploring the potential of nanoscale $(Ga_{1-x}Zn_x)(N_{1-x}O_x)$, our group developed a solid-state synthesis method using nanoscale precursors which produced $(Ga_{1-x}Zn_x)(N_{1-x}O_x)$ nanoparticles.[19] One discovery that the Domen group made in their early work was that during $(Ga_{1-x}Zn_x)(N_{1-x}O_x)$ synthesis, the reaction goes through an intermediate phase, which was identified as spinel $ZnGa_2O_4$.[28] Our group used knowledge of the $ZnGa_2O_4$ intermediate to designed a solid state reaction using nanoscale $ZnGa_2O_4$ and ZnO as precursors. Both nanoscale precursors were synthesized in separate solution phase reactions and then dried into a powder. The two powders were physically mixed and then heated in a quartz tube furnace under a flow of NH_3 (g). The resulting reaction produced $(Ga_{1-x}Zn_x)(N_{1-x}O_x)$ nanoparticles. The mechanism, shown in Figure 1.2, is thought to involve topotactic nucleation between the ZnO and $ZnGa_2O_4$ nanoparticle precursors, with ZnO serving as the wurtzite template and $ZnGa_2O_4$ diffusing into the ZnO particles, along with nitrogen being incorporated from the reactive NH_3 (g).[41] One major benefit of using nanoscale precursors is that nanoparticles are more reactive due to the large surface-to-volume ratio, which allows the nanoscale solid state reaction to be performed at lower temperatures than the original bulk syntheses. Lower synthesis temperatures played a key role in the ability to synthesize $(Ga_{1-x}Zn_x)(N_{1-x}O_x)$ particles in a full range of x-values, since Zn becomes volatile at higher temperatures.[9, 25, 35] Previously, the bulk synthesis methods only allowed for synthesis of x-values in the 0-0.4 range,[4, 9, 35, 42] whereas the nanoscale solid state synthesis allows for a full range of x-values to be synthesized, $0.06<x<0.98$.[20, 27, 43]

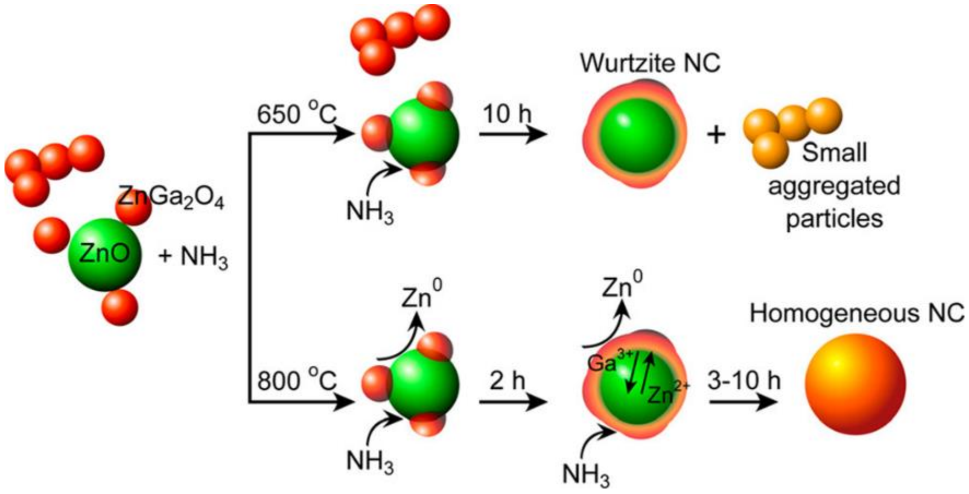

Figure 1.2: Scheme showing the proposed formation mechanism of $(Ga_{1-x}Zn_x)(N_{1-x}O_x)$ nanocrystals at 650 °C and 800 °C with ZnO, $ZnGa_2O_4$ and NH_3 as precursors. From reference 41.

The ability to synthesize $(Ga_{1-x}Zn_x)(N_{1-x}O_x)$ in the full range of x-values allowed us to study the different physical and photochemical properties of $(Ga_{1-x}Zn_x)(N_{1-x}O_x)$ at different x-values. Transmission electron microscopy (TEM) studies played a key role in our group's research into how the elements are distributed in the $(Ga_{1-x}Zn_x)(N_{1-x}O_x)$ particles and how the physical elemental distribution affects the energy levels important for photochemical H_2 generation. Scanning transmission electron microscopy-energy dispersive X-ray spectroscopy (STEM-EDS) studies done by our group helped characterize the elemental composition of the particles, leading to the discovery that when synthesized at 650 °C, a heterogeneous “core/shell” like elemental distribution results, but when synthesized at 800 °C, a homogeneous elemental distribution is produced.[41] The overall goal of studying $(Ga_{1-x}Zn_x)(N_{1-x}O_x)$ nanoparticles is to investigate how and why they can be used to produce solar fuels by understanding their optical properties and their relationship to solar fuel production.

1.2.2 Photochemical H_2 Generation with Redox Mediators

In Chapter 3, efforts to understand how $(Ga_{1-x}Zn_x)(N_{1-x}O_x)$ nanocrystals can be used for photochemical H_2 generation will be described. Photochemical H_2 generation can be accomplished with a variety of different systems. One type of system architecture consists of a light absorber (usually a nanoparticle semiconductor), a redox mediator (like methyl viologen), a solution-phase cocatalyst (Pt nanoparticles), and a hole scavenger (like 3-mercaptopropionic acid (3-MPA) or dithioerythritol (DTE)).[44-45] In this system, the semiconductor nanoparticles absorb light, producing an excited electron and hole. The electron then transfers to the redox mediator, which subsequently transfers the electron to the cocatalyst where proton reduction occurs. The photoexcited hole is consumed by the hole scavenger; the system can then turn over again. A system like this benefits from having the photoexcited electron and hole removed from the light absorber very quickly, protecting the light absorber from photooxidation and degradation as well as allowing it to efficiently excite more carriers. However, having so many components in a system means that there may be multiple rate-limiting steps. For example, these systems can be limited by the hole scavenger if it is not removing holes fast enough.[44, 46] Alternatively, even if the electron and hole transfer from the light absorber are both optimized, often the cocatalyst can limit performance, as Zhu et al. saw in their system with CdS, methyl viologen, 3-MPA, and Pt.[44]

One of the main characteristics governing the efficiencies of redox mediated H_2 production systems is the driving force and band potential alignments, illustrated in Figure 1.3. Ideally, the CB of the semiconductor light absorber would be more negative than the redox potential of the mediator, which would be more negative than the band potential/Fermi level of the cocatalyst. This allows for the electron to flow "down-hill", or in a thermodynamically favorable direction. The VB of the semiconductor light absorber should be more positive than the redox potential of the hole scavenger so that the hole can flow "up-hill", which is most favorable. When the driving forces for charge transfer are optimized, the system can perform at its highest efficiency.

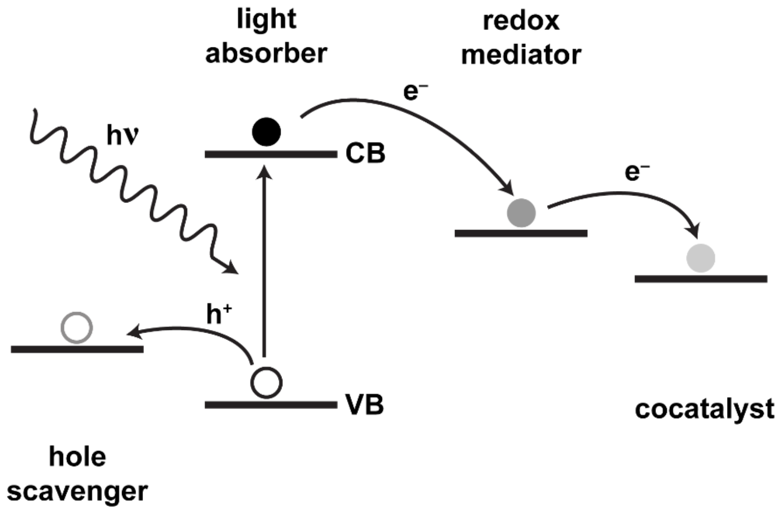

Figure 1.3: Band diagram showing the ideal band alignment and photoexcited electron and hole transfer in a H_2 production system with a light absorber, redox mediator, cocatalyst, and hole scavenger.

There are some complicating factors that can affect system performance and lead to non-ideal band alignments. One thing to consider is the pH of the system. Depending on the semiconductor being used as the light absorber, pH changes can cause the CB and/or VB to shift in energy, leading to non-ideal band alignment with the redox mediator and/or the hole scavenger.[47-50] Certain redox mediators like methyl viologen have redox potentials that are pH independent,[51-54] but the redox potential of the hole scavenger could change with pH, causing the driving force for hole scavenging to increase or decrease.[55] The Fermi level of the cocatalyst can also change with pH. For example, the Fermi level of Pt nanoparticles can shift with pH, causing the driving force for electron transfer from the redox mediator to change.[56-57] Additional complications that can affect system performance include degradation of the light absorber, H_2-consuming back reactions on the cocatalyst, and minor electron and hole transfer pathways that take away a small percentage of the electrons and holes from the main H_2 production pathway. These limitations will be studied and discussed as they pertain to the $(Ga_{1-x}Zn_x)(N_{1-x}O_x)$ H_2 production system in Chapter 3.

1.2.3 Electron Energy Loss Spectroscopy

Chapter 4 will discuss electron energy loss spectroscopy (EELS) studies done on $(Ga_{1-x}Zn_x)(N_{1-x}O_x)$ nanocrystals to investigate the single particle electronic band structure. EELS is a technique in electron microscopy that is typically paired with STEM and used to measure the spatially-resolved electronic structure of a sample.[58-60] EELS is performed by inserting a sample into a TEM and collecting the inelastically scattered electrons from the primary electron beam with an EELS detector. Figure 1.4, from reference 61, shows how an EELS detector can be interfaced with a TEM instrument, with the EELS detector attached below the viewing chamber.[61]

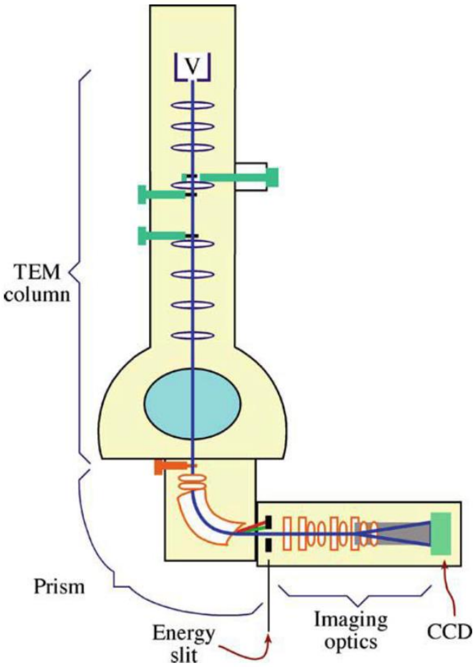

Figure 1.4: Diagram showing how an EELS detector can be interfaced with a TEM column. This figure is from reference 61.

At the top of the TEM column, an electron gun produces a beam of electrons, which pass through various lenses and apertures designed to focus the beam before hitting the sample. After the electron beam hits the sample, the TEM camera can detect which electrons were absorbed by the sample and which were transmitted, creating a transmission image of the sample. In addition to normal TEM imaging, when the electron beam hits the sample, various other events can occur, as shown in Figure 1.5 from reference 61.

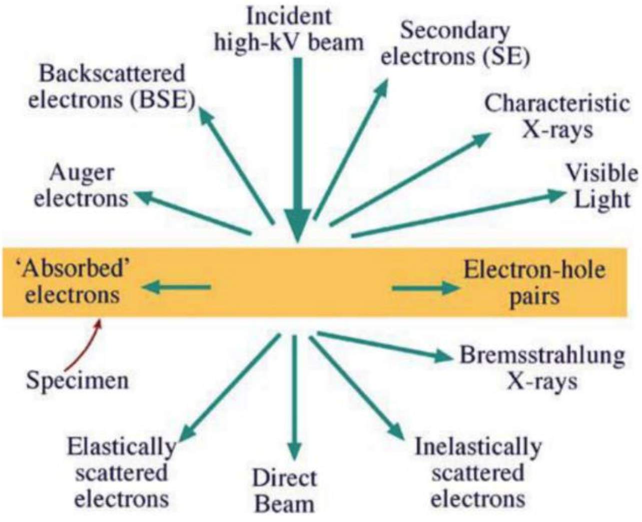

Figure 1.5: A diagram showing signals that can be generated when an electron beam interacts with a sample. This figure is from reference 61.

The events in Figure 1.5 generate a variety of signals that can be collected with the proper detectors. Characteristic X-rays can be collected with an EDS detector and used to create elemental composition maps.[41, 62-64] The visible light emitted can be collected for cathodoluminescence measurement, which give information on low-energy phenomena like the band gap and defect states.[65] Another example is the EELS signal, when electrons from the primary electron beam collide with the electrons in the sample inelastically, lose energy, and are scattered. The inelastically scattered electrons can be collected and an EELS spectrum can be generated. An example of an EELS spectrum is given in Figure 1.6, which shows the various regions in an EELS spectrum and the possible excitation processes that can occur.[66]

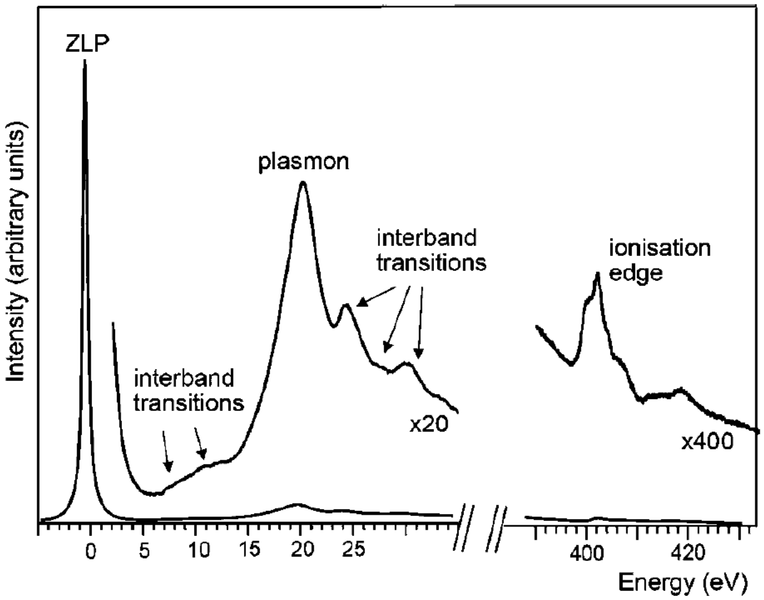

Figure 1.6: EELS spectrum of GaN, which shows the different excitation processes that can occur in electron energy loss spectroscopy. This figure is from reference 66.

The first and most obvious feature in an EELS spectrum is the zero-loss peak (ZLP), which is due to the electrons from the primary electron beam that did not lose energy, instead passing straight through the sample. The region from about 0-50 eV is called the low-loss region and it contains information about the bandgap, interband transitions, and plasmon excitations. The higher energy region from ~100 eV and above is the core-loss region, which gives information on the elemental composition of the sample due to the higher energy core electron ionization.[59] EELS helps characterize the energy transitions between the energy levels of the particles for both the heterogeneous and homogeneous $(Ga_{1-x}Zn_x)(N_{1-x}O_x)$ nanoparticles, providing an understanding of the electronic structure of $(Ga_{1-x}Zn_x)(N_{1-x}O_x)$ nanoparticles, allowing us to develop a suitable system for photochemically producing H_2, as discussed in Chapter 3. The low-loss EELS spectra of $(Ga_{1-x}Zn_x)(N_{1-x}O_x)$ nanocrystals will be discussed and analyzed in Chapter 4.

1.3 Summary

Solar fuel production via artificial photosynthetic systems can be an alternative to fossil fuel use, allowing us to potentially avoid catastrophically damaging Earth's ecosystems further. However, further investigation is needed in order to improve efficiencies. Ideal photocatalytic materials must have the proper band alignment for one or both water splitting half reactions and a band gap capable of utilizing large portions of solar irradiation, in addition to resistance to photooxidation. Efforts are still being made to find ideal photocatalytic materials; solid-state synthesis offers a promising avenue to produce new materials with optimally engineered band gaps and stability.

The purpose of the research in this dissertation is to understand how solid-state synthesis can be used to create novel materials for use in photochemical solar fuel production, how those materials function as light absorbers, and to characterize the physical and electronic properties of the materials. Chapter 2 will discuss the synthesis and surface functionalization of $(Ga_{1-x}Zn_x)(N_{1-x}O_x)$ nanocrystals, while Chapter 3 will detail their use as a light absorber for a photochemical H_2 production system. Chapter 4 includes electron energy loss spectroscopy studies of $(Ga_{1-x}Zn_x)(N_{1-x}O_x)$ nanocrystals, which shed light on the electronic band structure of the material with implications for its use as a light absorber in solar fuel production systems.

1.4 References

(1) Lewis, N. S.; Nocera, D. G., Powering the planet: Chemical challenges in solar energy utilization. *Proceedings of the National Academy of Sciences of the United States of America* **2006**, *103*, 15729-15735.

(2) Walter, M. G.; Warren, E. L.; McKone, J. R.; Boettcher, S. W.; Mi, Q. X.; Santori, E. A.; Lewis, N. S., Solar Water Splitting Cells. *Chemical Reviews* **2010**, *110*, 6446-6473.

(3) Kudo, A.; Miseki, Y., Heterogeneous Photocatalyst Materials for Water Splitting. *Chemical Society Reviews* **2009**, *38*, 253-278.

(4) Maeda, K.; Domen, K., Photocatalytic Water Splitting: Recent Progress and Future Challenges. *Journal of Physical Chemistry Letters* **2010**, *1*, 2655-2661.

(5) Zhou, M.; Bao, J.; Xu, Y.; Zhang, J.; Xie, J.; Guan, M.; Wang, C.; Wen, L.; Lei, Y.; Xie, Y., Photoelectrodes Based upon Mo:$BiVO_4$ Inverse Opals for Photoelectrochemical Water Splitting. *ACS Nano* **2014**, *8*, 7088-7098.

(6) Zhang, G.; Zhang, W.; Minakata, D.; Chen, Y.; C. Crittenden, J.; Wang, P., The pH effects on H2 evolution kinetics for visible light water splitting over the Ru/(CuAg)0.15In0.3Zn1.4S2 photocatalyst. *International Journal of Hydrogen Energy* **2013**, *38*, 11727-11736.

(7) Sivula, K.; Zboril, R.; Le Formal, F.; Robert, R.; Weidenkaff, A.; Tucek, J.; Frydrych, J.; Grätzel, M., Photoelectrochemical Water Splitting with Mesoporous Hematite Prepared by a Solution-Based Colloidal Approach. *Journal of the American Chemical Society* **2010**, *132*, 7436-7444.

(8) Sabio, E. M.; Chamousis, R. L.; Browning, N. D.; Osterloh, F. E., Photocatalytic Water Splitting with Suspended Calcium Niobium Oxides: Why Nanoscale is Better than Bulk – A Kinetic Analysis. *Journal of Physical Chemistry C* **2012**, *116*, 3161-3170.

(9) Maeda, K.; Teramura, K.; Takata, T.; Hara, M.; Saito, N.; Toda, K.; Inoue, Y.; Kobayashi, H.; Domen, K., Overall Water Splitting on $(Ga_{1-x}Zn_x)(N_{1-x}O_x)$ Solid Solution Photocatalyst: Relationship between Physical Properties and Photocatalytic Activity. *Journal of Physical Chemistry B* **2005**, *109*, 20504-20510.

(10) Maeda, K.; Ohno, T.; Domen, K., A copper and chromium based nanoparticulate oxide as a noble-metal-free cocatalyst for photocatalytic water splitting. *Chemical Science* **2011**, *2*, 1362-1368.

(11) Li, Y.; Takata, T.; Cha, D.; Takanabe, K.; Minegishi, T.; Kubota, J.; Domen, K., Vertically Aligned Ta3N5 Nanorod Arrays for Solar-Driven Photoelectrochemical Water Splitting. *Advanced Materials* **2013**, *25*, 125-131.

(12) Kumagai, N.; Ni, L.; Irie, H., A visible-light-sensitive water splitting photocatalyst composed of Rh3+ in a 4d6 electronic configuration, Rh3+-doped ZnGa2O4. *Chemical Communications* **2011**, *47*, 1884-1886.

(13) Ikeda, T.; Xiong, A.; Yoshinaga, T.; Maeda, K.; Domen, K.; Teranishi, T., Polyol Synthesis of Size-Controlled Rh Nanoparticles and Their Application to Photocatalytic Overall Water Splitting under Visible Light. *Journal of Physical Chemistry C* **2013**, *117*, 2467-2473.

(14) Berto, T. F.; Sanwald, K. E.; Byers, J. P.; Browning, N. D.; Gutiérrez, O. Y.; Lercher, J. A., Enabling Overall Water Splitting on Photocatalysts by CO-Covered Noble Metal Co-catalysts. *The Journal of Physical Chemistry Letters* **2016**, *7*, 4358-4362.

(15) Adeli, B.; Taghipour, F., Reduced Graphene Oxide Composite of Gallium Zinc Oxynitride Photocatalyst with Improved Activity for Overall Water Splitting. *Chemical Engineering & Technology* **2016**, *39*, 142-148.

(16) Maeda, K.; Takata, T.; Hara, M.; Saito, N.; Inoue, Y.; Kobayashi, H.; Domen, K., GaN:ZnO Solid Solution as a Photocatalyst for Visible-Light-Driven Overall Water Splitting. *Journal of the American Chemical Society* **2005**, *127*, 8286-8287.

(17) Xie, R.-J.; Hintzen, H. T., Optical Properties of (Oxy)Nitride Materials: A Review. *Journal of the American Ceramic Society* **2013**, *96*, 665-687.

(18) Li, X.; Zhang, Q.; Wang, H.; Li, Y., Synthesis of Mesoporous $(Ga_{1-x}Zn_x)(N_{1-x}O_x)$ Using Layered Double Hydroxides as Precursors for Enhanced Visible-Light Driven H2 Production. *Chinese Journal of Chemistry* **2017**, *35*, 196-202.

(19) Lee, K.; Tienes, B. M.; Wilker, M. B.; Schnitzenbaumer, K. J.; Dukovic, G., $(Ga_{1-x}Zn_x)(N_{1-x}O_x)$ Nanocrystals: Visible Absorbers with Tunable Composition and Absorption Spectra. *Nano Letters* **2012**, *12*, 3268-3272.

(20) Wang, J.; Huang, B.; Wang, Z.; Wang, P.; Cheng, H.; Zheng, Z.; Qin, X.; Zhang, X.; Dai, Y.; Whangbo, M.-H., Facile Synthesis of Zn-rich $(GaN)_{1-x}(ZnO)_x$ Solid Solutions Using Layered Double Hydroxides as Precursors. *Journal of Materials Chemistry* **2011**, *21*, 4562-4567.

(21) Ren, B.; Zhang, X.; Zhao, M.; Wang, X.; Ye, J.; Wang, D., Significant enhancement in photocatalytic activity of $(GaN)_{1-x}(ZnO)_x$ nanowires via solubility and crystal facet tailoring. *AIP Advances* **2018**, *8*, 015206.

(22) RajaAmbal, S.; Yadav, A. K.; Jha, S. N.; Bhattacharyya, D.; Gopinath, C. S., Electronic structure-sunlight driven water splitting activity correlation of $(Zn_{1-y}Ga_y)(O_{1-z}N_z)$. *Physical Chemistry Chemical Physics* **2014**, *16*, 23654-23662.

(23) Martha, S.; Reddy, K. H.; Parida, K. M.; Satapathy, P. K., Enhanced photocatalytic activity over N-doped GaZn mixed oxide under visible light irradiation. *International Journal of Hydrogen Energy* **2012**, *37*, 115-124.

(24) Hisatomi, T.; Maeda, K.; Lu, D.; Domen, K., The Effects of Starting Materials in the Synthesis of $(Ga_{1-x}Zn_x)(N_{1-x}O_x)$ Solid Solution on Its Photocatalytic Activity for Overall Water Splitting under Visible Light. *ChemSusChem* **2009**, *2*, 336-343.

(25) Han, W.-Q.; Liu, Z.; Yu, H.-G., Synthesis and Optical Properties of GaN/ZnO Solid Solution Nanocrystals. *Applied Physics Letters* **2010**, *96*, 183112.

(26) Hahn, C.; Fardy, M. A.; Nguyen, C.; Natera-Comte, M.; Andrews, S. C.; Yang, P. D., Synthesis and Photocatalytic Properties of Single Crystalline $(Ga_{1-x}Zn_x)(N_{1-x}O_x)$ Nanotubes. *Israel Journal of Chemistry* **2012**, *52*, 1111-1117.

(27) Dharmagunawardhane, H. A. N.; James, A.; Wu, Q.; Woerner, W. R.; Palomino, R. M.; Sinclair, A.; Orlov, A.; Parise, J. B., Unexpected visible light driven photocatalytic activity without

cocatalysts and sacrificial reagents from a $(GaN)_{1-x}(ZnO)_x$ solid solution synthesized at high pressure over the entire composition range. *RSC Advances* **2018**, *8*, 8976-8982.

(28) Chen, H.; Wen, W.; Wang, Q.; Hanson, J. C.; Muckerman, J. T.; Fujita, E.; Frenkel, A. I.; Rodriguez, J. A., Preparation of $(Ga_{1-x}Zn_x)(N_{1-x}O_x)$ Photocatalysts from the Reaction of NH_3 with Ga_2O_3/ZnO and $ZnGa_2O_4$: *In Situ* Time-Resolved XRD and XAFS Studies. *Journal of Physical Chemistry C* **2009**, *113*, 3650-3659.

(29) Adeli, B.; Taghipour, F., A Review of Synthesis Techniques for Gallium-Zinc Oxynitride Solar-Activated Photocatalyst for Water Splitting. *ECS J. Solid State Sci. Technol.* **2013**, *2*, Q118-Q126.

(30) Maeda, K.; Teramura, K.; Masuda, H.; Takata, T.; Saito, N.; Inoue, Y.; Domen, K., Efficient Overall Water Splitting under Visible-Light Irradiation on $(Ga_{1-x}Zn_x)(N_{1-x}O_x)$ Dispersed with Rh−Cr Mixed-Oxide Nanoparticles: Effect of Reaction Conditions on Photocatalytic Activity. *Journal of Physical Chemistry B* **2006**, *110*, 13107-13112.

(31) Maeda, K.; Teramura, K.; Domen, K., Development of Cocatalysts for Photocatalytic Overall Water Splitting on $(Ga_{1-x}Zn_x)(N_{1-x}O_x)$ Solid Solution. *Catalysis Surveys from Asia* **2007**, *11*, 145-157.

(32) Maeda, K.; Hashiguchi, H.; Masuda, H.; Abe, R.; Domen, K., Photocatalytic Activity of $(Ga_{1-x}Zn_x)(N_{1-x}O_x)$ for Visible-Light-Driven H_2 and O_2 Evolution in the Presence of Sacrificial Reagents. *Journal of Physical Chemistry C* **2008**, *112*, 3447-3452.

(33) Maeda, K.; Teramura, K.; Domen, K., Effect of Post-Calcination on Photocatalytic Activity of $(Ga_{1-x}Zn_x)(N_{1-x}O_x)$ Solid Solution for Overall Water Splitting under Visible Light. *Journal of Catalysis* **2008**, *254*, 198-204.

(34) Hisatomi, T.; Maeda, K.; Takanabe, K.; Kubota, J.; Domen, K., Aspects of the Water Splitting Mechanism on $(Ga_{1-x}Zn_x)(N_{1-x}O_x)$ Photocatalyst Modified with $Rh_{2-y}Cr_yO_3$ Cocatalyst. *The Journal of Physical Chemistry C* **2009**, *113*, 21458-21466.

(35) Maeda, K.; Domen, K., Solid Solution of GaN and ZnO as a Stable Photocatalyst for Overall Water Splitting under Visible Light. *Chemistry of Materials* **2010**, *22*, 612-623.

(36) Xiong, A.; Yoshinaga, T.; Ikeda, T.; Takashima, M.; Hisatomi, T.; Maeda, K.; Setoyama, T.; Teranishi, T.; Domen, K., Effect of Hydrogen and Oxygen Evolution Cocatalysts on Photocatalytic Activity of GaN:ZnO. *European Journal of Inorganic Chemistry* **2014**, *2014*, 767-772.

(37) Menon, S. S.; Kuppulingam, B.; Baskar, K.; Sairam, T. N.; Ravindran, T. R.; Gupta, B.; Singh, S., Realization of high photocatalytic hydrogen generation activity by nanostructured $Ga_{1-x}Zn_xO_{1-z}N_z$ solid-solution without co-catalyst. *International Journal of Hydrogen Energy* **2015**, *40*, 13901-13908.

(38) Zhou, Y.; Chen, G.; Yu, Y.; Zhao, L.; Yu, Q.; He, Q., Effects of La-doping on charge separation behavior of ZnO:GaN for its enhanced photocatalytic performance. *Catalysis Science & Technology* **2016**, *6*, 1033-1041.

(39) Maeda, K.; Teramura, K.; Saito, N.; Inoue, Y.; Domen, K., Improvement of Photocatalytic Activity of $(Ga_{1-x}Zn_x)(N_{1-x}O_x)$ Solid Solution for Overall Water Splitting by Co-loading Cr and Another Transition Metal. *Journal of Catalysis* **2006**, *243*, 303-308.

(40) Hirai, T.; Maeda, K.; Yoshida, M.; Kubota, J.; Ikeda, S.; Matsumura, M.; Domen, K., Origin of Visible Light Absorption in GaN-Rich $(Ga_{1-x}Zn_x)(N_{1-x}O_x)$ Photocatalysts. *Journal of Physical Chemistry C* **2007**, *111*, 18853-18855.

(41) Tongying, P.; Lu, Y.-G.; Hall, L. M. G.; Lee, K.; Sulima, M.; Ciston, J.; Dukovic, G., Control of Elemental Distribution in the Nanoscale Solid-State Reaction That Produces $(Ga_{1-x}Zn_x)(N_{1-x}O_x)$ Nanocrystals. *ACS Nano* **2017**, *11*, 8401-8412.

(42) Maeda, K.; Domen, K., New Non-Oxide Photocatalysts Designed for Overall Water Splitting under Visible Light. *Journal of Physical Chemistry C* **2007**, *111*, 7851-7861.

(43) Li, Y.; Zhu, L.; Yang, Y.; Song, H.; Lou, Z.; Guo, Y.; Ye, Z., A Full Compositional Range for a $(Ga_{1-x}Zn_x)(N_{1-x}O_x)$ Nanostructure: High Efficiency for Overall Water Splitting and Optical Properties. *Small* **2015**, *11*, 871-876.

(44) Zhu, H.; Song, N.; Lv, H.; Hill, C. L.; Lian, T., Near Unity Quantum Yield of Light-Driven Redox Mediator Reduction and Efficient H_2 Generation Using Colloidal Nanorod Heterostructures. *Journal of the American Chemical Society* **2012**, *134*, 11701-11708.

(45) Miller, D. S.; Bard, A. J.; McLendon, G.; Ferguson, J., Catalytic water reduction at colloidal metal "microelectrodes". 2. Theory and experiment. *Journal of the American Chemical Society* **1981**, *103*, 5336-5341.

(46) Pellegrino, F.; Sordello, F.; Minella, M.; Minero, C.; Maurino, V., The Role of Surface Texture on the Photocatalytic H2 Production on TiO2. *Catalysts* **2019**, *9*.

(47) Yan, S. G.; Lyon, L. A.; Lemon, B. I.; Preiskorn, J. S.; Hupp, J. T., Energy Conversion Chemistry: Mechanisms of Charge Transfer at Metal-Oxide Semiconductor/Solution Interfaces. *Journal of Chemical Education* **1997**, *74*, 657.

(48) She, C.; Anderson, N. A.; Guo, J.; Liu, F.; Goh, W.-H.; Chen, D.-T.; Mohler, D. L.; Tian, Z.-Q.; Hupp, J. T.; Lian, T., pH-Dependent Electron Transfer from Re-bipyridyl Complexes to Metal Oxide Nanocrystalline Thin Films. *The Journal of Physical Chemistry B* **2005**, *109*, 19345-19355.

(49) Lyon, L. A.; Hupp, J. T., Energetics of the Nanocrystalline Titanium Dioxide/Aqueous Solution Interface: Approximate Conduction Band Edge Variations between H0 = −10 and H- = +26. *The Journal of Physical Chemistry B* **1999**, *103*, 4623-4628.

(50) Lemon, B. I.; Liu, F.; Hupp, J. T., Electrochemical, spectral, and quartz crystal microgravimetric assessment of conduction band edge energies for nanocrystalline zirconium dioxide/solution interfaces. *Coordination Chemistry Reviews* **2004**, *248*, 1225-1230.

(51) Zhang, J.; Yu, J.; Jaroniec, M.; Gong, J. R., Noble Metal-Free Reduced Graphene Oxide-$Zn_xCd_{1-x}S$ Nanocomposite with Enhanced Solar Photocatalytic H_2-Production Performance. *Nano Letters* **2012**, *12*, 4584-4589.

(52) Van Dijk, C.; Veeger, C., The Effects of pH and Redox Potential on the Hydrogen Production Activity of the Hydrogenase from Megasphaera elsdenii. *European Journal of Biochemistry* **1981**, *114*, 209-219.

(53) Li, Q.; Meng, H.; Zhou, P.; Zheng, Y.; Wang, J.; Yu, J.; Gong, J., $Zn_{1-x}Cd_xS$ Solid Solutions with Controlled Bandgap and Enhanced Visible-Light Photocatalytic H_2-Production Activity. *ACS Catalysis* **2013**, *3*, 882-889.

(54) Li, Q.; Guo, B.; Yu, J.; Ran, J.; Zhang, B.; Yan, H.; Gong, J. R., Highly Efficient Visible-Light-Driven Photocatalytic Hydrogen Production of CdS-Cluster-Decorated Graphene Nanosheets. *Journal of the American Chemical Society* **2011**, *133*, 10878-10884.

(55) Cleland, W. W., Dithiothreitol, a New Protective Reagent for SH Groups*. *Biochemistry* **1964**, *3*, 480-482.

(56) Yoshida, M.; Yamakata, A.; Takanabe, K.; Kubota, J.; Osawa, M.; Domen, K., ATR-SEIRAS Investigation of the Fermi Level of Pt Cocatalyst on a GaN Photocatalyst for Hydrogen Evolution under Irradiation. *Journal of the American Chemical Society* **2009**, *131*, 13218-13219.

(57) Scanlon, M. D.; Peljo, P.; Méndez, M. A.; Smirnov, E.; Girault, H. H., Charging and discharging at the nanoscale: Fermi level equilibration of metallic nanoparticles. *Chemical Science* **2015**, *6*, 2705-2720.

(58) Hachtel, J. A.; Lupini, A. R.; Idrobo, J. C., Exploring the capabilities of monochromated electron energy loss spectroscopy in the infrared regime. *Scientific Reports* **2018**, *8*, 5637.

(59) Egerton, R. F., Electron energy-loss spectroscopy in the TEM. *Reports on Progress in Physics* **2009**, *72*, 016502.

(60) Crozier, P. A., Vibrational and valence aloof beam EELS: A potential tool for nondestructive characterization of nanoparticle surfaces. *Ultramicroscopy* **2017**, *180*, 104-114.

(61) Williams, D. B.; Carter, C. B., *Transmission Electron Microscopy*; Springer: New York, 1996.

(62) Yoshida, M.; Hirai, T.; Maeda, K.; Saito, N.; Kubota, J.; Kobayashi, H.; Inoue, Y.; Domen, K., Photoluminescence Spectroscopic and Computational Investigation of the Origin of the Visible Light Response of $(Ga_{1-x}Zn_x)(N_{1-x}O_x)$ Photocatalyst for Overall Water Splitting. *The Journal of Physical Chemistry C* **2010**, *114*, 15510-15515.

(63) Yang, M.; Huang, Q.; Jin, X., Microwave synthesis of porous ZnGaNO solid solution for improved visible light photocatalytic performance. *Solid State Sciences* **2012**, *14*, 465-470.

(64) Liu, B.; Bando, Y.; Liu, L.; Zhao, J.; Masanori, M.; Jiang, X.; Golberg, D., Solid–Solution Semiconductor Nanowires in Pseudobinary Systems. *Nano Letters* **2013**, *13*, 85-90.

(65) Kociak, M.; Zagonel, L. F., Cathodoluminescence in the scanning transmission electron microscope. *Ultramicroscopy* **2017**, *176*, 112-131.

(66) Keast, V. J.; Bosman, M., New developments in electron energy loss spectroscopy. *Microscopy Research and Technique* **2007**, *70*, 211-219.

Chapter 2: Synthesis and Surface Functionalization of $(Ga_{1-x}Zn_x)(N_{1-x}O_x)$ Nanocrystals

2.1 Introduction

$(Ga_{1-x}Zn_x)(N_{1-x}O_x)$ is a solid solution of GaN and ZnO that is capable of splitting water under visible light irradiation.[1-6] Originally $(Ga_{1-x}Zn_x)(N_{1-x}O_x)$ was made via a typical solid-state synthesis with powder precursors being heated in a furnace under a flow of ammonia.[7] Since then, many researchers have come up with various other solid state methods to synthesize $(Ga_{1-x}Zn_x)(N_{1-x}O_x)$.[8-16] This exploration of solid-state synthesis technique has created an interesting survey of synthesis options for this one material that could potentially be used to create other more compositionally complex multinary materials with more than four components.[17-19]

In this chapter, the synthesis mechanism of nanoscale $(Ga_{1-x}Zn_x)(N_{1-x}O_x)$ is studied, the precursor choice is analyzed and varied, and the surface functionalization of the nanoscale product is investigated in various ways. Understanding the synthesis mechanism can help inform whether or not this specific synthesis path can be used to create $(Ga_{1-x}Zn_x)(N_{1-x}O_x)$ of different size and shape and would allow the investigation of whether differently sized and shaped nanoscale $(Ga_{1-x}Zn_x)(N_{1-x}O_x)$ would show different photocatalytic properties. Additionally, surface functionalization plays a key role in product utilization; surface ligands will determine in which solvents the product can be dispersed in, how the product can be studied, and how it can be used in different systems and devices.

Throughout the investigation, the data supported a synthesis mechanism involving topotactic nucleation of $(Ga_{1-x}Zn_x)(N_{1-x}O_x)$ at the interface between the nanoscale precursors of

ZnO and $ZnGa_2O_4$. Data suggests that the ZnO acts as the template for the Ga from the $ZnGa_2O_4$ precursor and the N from NH_3 to diffuse into.[20] Following the natural next step, a different size and shape of ZnO was tested as a precursor and it was found that changing the size and shape of ZnO at that scale did not change the $(Ga_{1-x}Zn_x)(N_{1-x}O_x)$ product morphology. Additionally, the surface functionalization of the nanoscale $(Ga_{1-x}Zn_x)(N_{1-x}O_x)$ was experimented with in an attempt to solubilize the product in multiple different solvents. To date, only one functionalization attempt has been successful for our group and it uses trimethoxy(octadecyl)silane (ODTMS) as a ligand that attaches to OH groups on the $(Ga_{1-x}Zn_x)(N_{1-x}O_x)$ surface resulting in the product being semi-soluble in toluene.[21]

What follows are synthesis and surface functionalization procedures, both successful and unsuccessful. The synthesis procedures include three different kinds of ZnO precursors, which were used to test the effect of precursor size and shape on the final $(Ga_{1-x}Zn_x)(N_{1-x}O_x)$ product. These precursors are 10 nm ZnO nanoparticles, 4 nm ZnO particles, and ZnO nanorods. I tried six different surface functionalizations to improve solubilization yield, and I tried two different methods of attaching a Pt cocatalyst for H_2 production experiments described in Chapter 3.

2.2 Materials and Methods

2.2.1 Chemicals

Zinc acetate ($Zn(OAc)_2$, 99.99%), nitrosyl tetrafluoroborate (95%), trioctylphosphine oxide (TOPO, 99%), (3-aminopropyl)triethoxysilane (98.0%), butylamine (99.5%), L-ascorbic acid (AA, 99.0%), trimethoxy(octadecyl)silane (ODTMS, 90%), trichloro(octadecyl)silane (OTS, 90%), 3-mercaptopropionic acid (3-MPA, ≥99.0%), hexane (99%), toluene (99.5%), 1,2-hexadecanediol (90%), dioctyl ether (99%), benzyl ether (98%), 1-undecanol (99%), oleic acid

(≥99.0%), oleylamine (70%), pyridine (99.8%), tetramethylammonium hydroxide pentahydrate (TMAH, ≥97%), chloroplatinic acid hydrate (H_2PtCl_6, 99.9%), potassium tetrachloroplatinate(II) (98%, K_2PtCl_4), zinc acetylacetonate hydrate ($Zn(acac)_2$, 99.995%), gallium acetylacetonate ($Ga(acac)_3$, 99.99%), and zinc chloride ($ZnCl_2$, ≥98%), were purchased from Sigma-Aldrich. Dichloromethane (Certified ACS), dimethylformamide (Certified ACS), dimethyl sulfoxide (Certified ACS), 2-propanol (99.9%), methanol (99.9%), and sodium hydroxide (NaOH pellets, 99.3%) were purchased from Fisher. Octadecylphosphonic acid (ODPA, 99%) and tetradecylphosphonic acid (TDPA, 99%) were purchased from PCI Synthesis. 1,2-ethanediol (99.8%) was purchased from Macron Fine Chemicals. Ethyl acetate (99.5%) was purchased from EMD. Ethanol (95%) was purchased from Decon Labs. Ammonia (99.99%) was purchased from Airgas. All chemicals were purchased commercially and used without further purification.

2.2.2 ZnO Nanocrystal Synthesis (10 nm diameter)

As published previously,[22] 10 nm ZnO NCs were synthesized as follows. 40 mmol of $ZnCl_2$ was added to 200 mL of 1,2-ethanediol and stirred until dissolved. The mixture was heated to 150 °C in air. Once at 150 °C, 16 mL of 5 M NaOH in water was added dropwise at a rate of about 1 drop/second while stirring and maintaining the reaction temperature at 150 °C. When all the 5 M NaOH was added the solution was removed from heat and cooled to room temperature. The white powder product was washed in the reaction beaker initially via sedimentation, discarding the supernatant, and filling the beaker with 18 MΩ water to remove NaCl. The sedimentation process was repeated five times. The resulting white powder was collected via centrifugation (5000 rpm for 20 minutes) and washed an additional three times with water. After the supernatant was discarded for the final time, the remaining white powder was dried in the centrifuge tube in a vacuum desiccator.

2.2.3 ZnO Nanocrystal Synthesis (4 nm diameter)

4 nm ZnO NCs were synthesized following the procedure of Schwartz et al.[23] 90 mL of 0.101 M $Zn(OAc)_2$ in DMSO was prepared in a tall ~400 mL beaker with a stir bar. Next, 30 mL of 0.552 M TMAH in ethanol was prepared and added dropwise to the $Zn(OAc)_2$ solution at a rate of ~2 mL/min under constant stirring. Once all the TMAH was added, the ZnO NCs were crashed out using ethyl acetate. ~300 mL of ethyl acetate was added to the reaction beaker while stirring. A cloudy white precipitate forms. Using two 50 mL centrifuge tubes, equal amounts of the crashed-out ZnO solution was poured into each tube and centrifuged at 5000 rpm for ~5 min. The supernatant liquid was discarded and more crashed-out ZnO solution was added until all crashed out ZnO particles were at the bottom of the two centrifuge tubes. The ZnO NCs were washed once with ethyl acetate by adding ~45 mL of ethyl acetate to each centrifuge tube and sonicating for ~30 min to break-up the solid at the bottom of the tube, then the tubes were centrifuged and the liquid discarded. The ZnO NCs at the bottom of the centrifuge tubes were dried under vacuum in a vacuum desiccator.

2.2.4 ZnO Nanorod Synthesis

ZnO nanorods were synthesized as published previously.[24] 1 mmol $Zn(OAc)_2$, 0.45 mmol TDPA, 3 mmol TOPO, and 7.5 mL of dioctyl ether were combined in a 25 mL 3-neck round bottom flask with a stir bar under Ar (g). Next, O_2 and H_2O were removed by putting the reaction under vacuum and heating to 100 °C for 30 min. Then, the reaction was put back under Ar (g) and heated to 200 °C and held at 200 °C for 1 hour. The reaction was then cooled to 60 °C and 6 mmol of 1-undecanol was injected into the reaction via an Ar (g) purged syringe. Next, the reaction was heated to 250 °C and held at 250 °C for 2 hours. The reaction was then cooled to room temperature and the ZnO nanorods were transferred to a 50 mL centrifuge tube, washing the reaction flask with methanol three times (~20-25 mL of methanol total). The tube was centrifuged at 5000 rpm for 15 min. The methanol was discarded and ~20 mL of hexanes was added and the tube was sonicated until the solid at the bottom broke up (~2 min). Then the tube was centrifuged at 5000 rpm for 10 min. After centrifugation, the ZnO nanorod product was contained in the supernatant liquid layer.

2.2.5 $ZnGa_2O_4$ Nanocrystal Synthesis

As reported previously,[22] to synthesize $ZnGa_2O_4$ NCs, 1 mmol $Zn(acac)_2$, 2 mmol $Ga(acac)_3$, 5 mmol 1,2-hexadecanediol, 6 mmol oleic acid, and 6 mmol oleylamine were combined in 10 mL of benzyl ether in a 3-neck round bottom flask, stirred under Ar (g) until combined and heated to 40 °C. Then, the reaction was put under vacuum and the temperature was increased to 100 °C to remove O_2 and H_2O. Once bubbling of the reaction was minimal, the reaction was put back under Ar (g) and the temperature was increased to 200 °C. After the reaction was at 200 °C for 30 minutes, the temperature was increased to 280 °C and held for 2 hours. After 2 hours, the reaction was cooled to room temperature and the NC product was collected by centrifugation and washed three times by dissolving in 5 mL of hexanes and precipitating with 45 mL of ethanol.

2.2.6 $(Ga_{1-x}Zn_x)(N_{1-x}O_x)$ Nanocrystal Synthesis

$(Ga_{1-x}Zn_x)(N_{1-x}O_x)$ NCs were synthesized as reported previously.[22] Briefly, a total of ~200 mg of $ZnGa_2O_4$ NC capped with 3-MPA and ZnO NC precursors was heated in a quartz tube furnace at 650°C for 10 hours or 800 °C for 2-10 hours under a flow of NH_3 (g) at ~150 mL/min. The furnace was set to turn off after the desired reaction time and the sample was left in the furnace overnight to cool under flowing NH_3 (g). In the morning, the NH_3 (g) was turned off and the furnace was purged with Ar (g) before opening. The alumina boats containing the product were removed from the furnace and the product in the boats was carefully poured into a 4 mL borosilicate vial. For $(Ga_{1-x}Zn_x)(N_{1-x}O_x)$ NC synthesis using ZnO nanorods as the ZnO precursor, the ZnO nanorods and the $ZnGa_2O_4$ nanocrystals were mixed together as liquids first, then the mixed liquid was dried on a glass slide on a hotplate and scrapped off the glass slide into the alumina boat for nitridation. The $(Ga_{1-x}Zn_x)(N_{1-x}O_x)$ NCs were characterized using inductively coupled plasma-mass spectrometry (ICP-MS) to analyze for the content of Zn and Ga, diffuse reflectance spectroscopy (DR) to obtain a reflectance spectrum which was converted using the Kubelka-Munk equation into the equivalent of an absorbance spectrum, powder X-ray diffraction (XRD) to analyze the crystal structure and crystallite domain size, and transmission electron microscopy (TEM) to obtain particle size and morphology data.

2.2.7 Functionalization with ODTMS

The procedure for functionalizing the $(Ga_{1-x}Zn_x)(N_{1-x}O_x)$ NC surface with ODTMS ligands is from Chuang et al.,[21] and is as follows. About 20 mg of $(Ga_{1-x}Zn_x)(N_{1-x}O_x)$ powder is measured into a 15 mL centrifuge tube and 6 mL of toluene is added. The mixture of $(Ga_{1-x}Zn_x)(N_{1-x}O_x)$ and toluene is sonicated for 25 minutes at room temperature. Then 0.40 mL of ODTMS is added with continuous sonication. After 5 minutes, 0.15 mL of butylamine is added and the reaction is sonicated for 4.5 hours at 25-40°C. The water in the sonicator bath heats up over time, so periodically the sonicator water bath is changed out so that the temperature does not exceed 40 °C. After the 4.5 hours of sonication, the reaction is centrifuged at 5000 rpm for 2 minutes. The liquid layer is saved and any precipitate at the bottom is leftover $(Ga_{1-x}Zn_x)(N_{1-x}O_x)$ that was not successfully solubilized. The collected liquid layer is washed using 14 mL of isopropyl alcohol, which precipitates the $(Ga_{1-x}Zn_x)(N_{1-x}O_x)$ NCs and leaves excess ligand in solution. The precipitated solution is centrifuged at 5000 rpm for 10 minutes and the liquid layer is discarded, while the crashed out $(Ga_{1-x}Zn_x)(N_{1-x}O_x)$ NC product is resuspended in 1 mL of toluene.

2.2.8 Functionalization with APTES and attachment of metal cocatalyst

To functionalize the $(Ga_{1-x}Zn_x)(N_{1-x}O_x)$ NC surface with APTES ligands various procedures were consulted and modified.[25-28] Overall, 100 mg of $(Ga_{1-x}Zn_x)(N_{1-x}O_x)$ powder is weighed into a 3-neck round bottom flask with a stir bar. 10 mL of toluene is added and the mixture is stirred. 0.2 mL of APTES is added and the reaction is refluxed for 4 hours at 100 °C under Ar (g). Then, the reaction is cooled to room temperature and washed with ethanol, which crashes out the $(Ga_{1-x}Zn_x)(N_{1-x}O_x)$ product. The crashed-out product is dried under a vacuum.

Following the functionalization with APTES, a metal cocatalyst can be attached to the end of the APTES ligand. To accomplish this, 100 mg of APTES-$(Ga_{1-x}Zn_x)(N_{1-x}O_x)$ powder is measured into a 15 mL centrifuge tube with a stir bar and 10 mL of water is added. 0.02 g of K_2PtCl_4 is added to the tube, the lid is secured, and the entire centrifuge tube is wrapped in Al foil. The tube is set in a rack on top of a stir plate and the mixture is stirred for 12 hours, or overnight. The reaction is washed with water by filling the tube to the top with water, mixing, and then centrifuging for 2 minutes at 5000 rpm. The liquid is discarded and the solid is washed with ethanol. After centrifuging for 2 minutes and discarding the liquid, the resulting solid is dried under vacuum.

2.2.9 Functionalization with $NOBF_4$

The procedure for the experiments done to try and functionalize $(Ga_{1-x}Zn_x)(N_{1-x}O_x)$ using $NOBF_4$ was adapted from Dong et al.,[29] and involved dispersing 25 mg of $(Ga_{1-x}Zn_x)(N_{1-x}O_x)$ powder in 5 mL of either hexanes, acetonitrile, or dimethyl formamide. Separately, between 6 and 14 mg of $NOBF_4$ was dissolved in either dichloromethane, ethanol, acetonitrile, or dimethyl formamide. The $NOBF_4$ solution was added to the $(Ga_{1-x}Zn_x)(N_{1-x}O_x)$ dispersion and mixed in various ways. The first attempt shook the vial for 5 minutes, the second sonicated for 2 hours, the third sonicated for 6 hours and stirred overnight, and the last one stirred for 23 hours. After mixing, the reaction is centrifuged and the solid collected contains the unsuccessfully solubilized particles. To the remaining liquid, a 1:1 mixture of toluene and hexane is added to crash out the successfully solubilized particles. The mixture is centrifuged for 5 minutes and the liquid is discarded, and the precipitated particles can be dispersed in acetonitrile or dimethyl formamide.

2.2.10 Functionalization with OTS

The procedure used for the OTS functionalization experiments were adapted from the ODTMS procedure[21] and involved measuring out 10 mg of $(Ga_{1-x}Zn_x)(N_{1-x}O_x)$ powder into a plastic vial or 15 mL centrifuge tube. Note, glass cannot be used because the OTS will react with the glass surface. OTS is a very reactive chemical in general, so any water or air will cause it to polymerize. A stir bar was added to the plastic centrifuge tube and the tube was capped with a rubber septum. The tube was flushed with Ar (g) for 20-30 minutes. Anhydrous toluene was injected into the tube and the toluene-$(Ga_{1-x}Zn_x)(N_{1-x}O_x)$ mixture was stirred for 25 minutes. 0.12 mL of OTS was added and after about 2 minutes, 0.23 mL of anhydrous pyridine was added. The vent needle and Ar (g) needle were removed from the tube and the reaction was stirred for a total of 20-40 hours. The stirring was stopped, and the reaction was left to settle for about 45 minutes. The Ar (g) and vent needles were put back into the centrifuge tube with the reaction and another 15 mL centrifuge tube was purged with Ar (g). Transfer the supernatant from the reaction into the newly Ar-purged centrifuge tube. About 10-11 mL of chloroform is added to the supernatant and the tube is centrifuged for 2 minutes at 5000 rpm. The Ar (g) and vent needles are reinserted into the tube and the chloroform is removed with an Ar-purged needle and syringe. Then, 3 mL of toluene is added and the tube is sonicated for 5-10 seconds. Once the toluene is added, the Ar (g) and vent needles can be removed.

2.2.11 Functionalization with ODPA

The procedure followed for ODPA functionalization experiments is from Yee et al.,[30] and is as follows. A 1:1 or 1:2 mole ratio of $(Ga_{1-x}Zn_x)(N_{1-x}O_x)$ powder to ODPA was measured out into separate 50 mL centrifuge tubes and 20 mL of ethanol was added to the ODPA to dissolve it. The ethanol-ODPA solution was added to the $(Ga_{1-x}Zn_x)(N_{1-x}O_x)$ powder and sonicated for 30 minutes. A large and a small stir bar were added to the centrifuge tube and the reaction stirred overnight (16-20 hours). After stirring overnight, the tube was centrifuged for 13 minutes at 5000 rpm and then washed with ethanol four times. After the last wash with ethanol, the ethanol was decanted, and 5 mL of hexanes or toluene was added and the tube was sonicated to disperse the particles.

2.2.12 Surface Hydroxylation of $(Ga_{1-x}Zn_x)(N_{1-x}O_x)$

The procedure used to attempt to hydroxylate the surface of $(Ga_{1-x}Zn_x)(N_{1-x}O_x)$ was as follows. About 9 g of NaOH was dissolved in 20 mL of water in a beaker. Once the NaOH solution had cooled to room temperature, it was added to 5 mg of $(Ga_{1-x}Zn_x)(N_{1-x}O_x)$ powder in a 50 mL centrifuge tube. The tube was shaken gently for 10 minutes and briefly sonicated twice for 1 minute each time. Next, the particles were centrifuged for 10 minutes and washed with 20 mL of water three times and then the powder was dried in a vacuum desiccator.

2.2.13 Pt Photodeposition on $(Ga_{1-x}Zn_x)(N_{1-x}O_x)$

The Pt photodeposition, from Carabineiro et al.[31] and Cavalca et al.,[32] was performed by measuring 1 mg of $(Ga_{1-x}Zn_x)(N_{1-x}O_x)$ powder into a small 1.5 mL glass vial and secured with a rubber septum. The vial was transferred into a glovebox where 10 µL of the Pt precursor solution (20 mg of H_2PtCl_6 in 2 mL of methanol) was added along with 290 µL of methanol and a stir bar. The septum was secured on the vial and the vial was removed from the glovebox. Next, the vial was sonicated for 30 minutes and then illuminated for 1 hour with a 405 nm diode laser at a power of 88 mW.

2.3 Observations and Hypotheses

One of the main goals when studying the $(Ga_{1-x}Zn_x)(N_{1-x}O_x)$ solid-state synthesis was to try and change the size or shape of the final product by changing the synthesis conditions and components. Some of the different conditions and components we have control over in the synthesis are the furnace temperature, the amount of precursor, and the identity of the two nanoscale precursors, ZnO and $ZnGa_2O_4$.

2.3.1 Temperature Dependence of $(Ga_{1-x}Zn_x)(N_{1-x}O_x)$ Synthesis

In our group's 2017 ACS Nano publication,[20] we discuss the $(Ga_{1-x}Zn_x)(N_{1-x}O_x)$ solid-state synthesis mechanism of topotactic nucleation and growth and how reaction temperature plays a key role in the final elemental distribution in the product. One key takeaway from that publication is that during topotactic nucleation, the ZnO precursor acts as the template for Ga and N to diffuse into. Another key takeaway is that the reaction temperature determines the amount of diffusion of Ga and N that is possible in the ZnO precursor. We found that at a reaction temperature of 650 °C there is not enough thermal energy for Ga and N to diffuse fully through the ZnO particle; however, we saw that at 800 °C there was enough thermal energy for Ga and N to diffuse fully throughout the ZnO precursor. Therefore, at reaction temperatures like 650 °C, we are left with heterogeneous "core/shell-like" nanocrystal products and at a reaction temperature of 800 °C the result is a homogeneous nanocrystal with Zn, Ga, N, and O all distributed evenly throughout the particle. This difference is depicted in Figure 1, which shows EDS maps of $(Ga_{1-x}Zn_x)(N_{1-x}O_x)$ synthesized at 650 °C and 800 °C.[20]

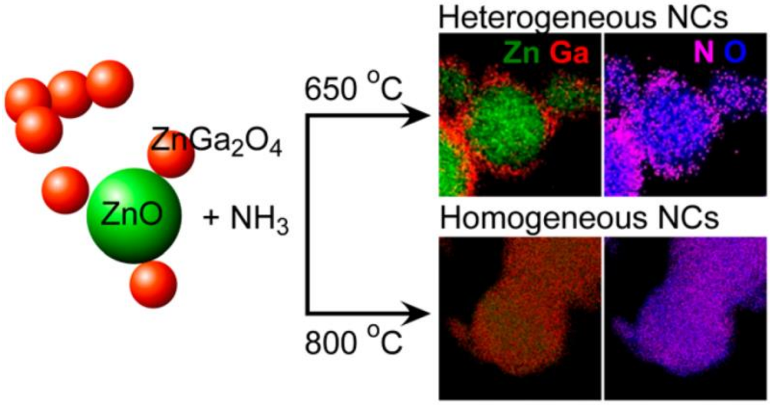

Figure 2.1: Schematic illustration showing the different elemental distributions in the (Ga1-xZnx)(N1-xOx) product that can result when different synthesis temperatures (650 °C and 800 °C) are used.20

At 650 °C we see a $(Ga_{1-x}Zn_x)(N_{1-x}O_x)$ product that has a heterogeneous distribution of Ga and N in the ZnO template. In general, the Ga and N concentrates towards the edges of the particle, while the ZnO is concentrated in the core. We hypothesize that this happens because there is not enough thermal energy at 650 °C for the Ga and N to fully diffuse through the ZnO particle. Conversely, at 800 °C we see homogeneous $(Ga_{1-x}Zn_x)(N_{1-x}O_x)$ particles, where the Ga, N, Zn, and O are all evenly distributed throughout the particle. We hypothesize that this is the case because at 800 °C there is enough vacancies, NH_3 decomposition, and thermal energy for the Ga and N to diffuse fully throughout the ZnO particle.

In conclusion, we have observed that different reaction temperatures can be used to alter the elemental distribution in $(Ga_{1-x}Zn_x)(N_{1-x}O_x)$ nanocrystals, with 650 °C resulting in heterogeneous “core/shell-like” particles and 800 °C resulting in homogeneous particles due to the difference in thermal energy available for ion diffusion. However, the reaction temperature did not appear to change the size or shape of the $(Ga_{1-x}Zn_x)(N_{1-x}O_x)$ product, it only changed the elemental distribution, so in our continued quest to change the size and shape of the $(Ga_{1-x}Zn_x)(N_{1-x}O_x)$ product, we moved on to changing the precursor size and shape.

2.3.2 Dependence on ZnO Precursor Size and Shape

One of the other ways we can change the synthesis conditions is to change the precursor size and shape. We targeted the ZnO precursor since we believe that it is the template which Ga and N diffuse into. Our aim is to see if the $(Ga_{1-x}Zn_x)(N_{1-x}O_x)$ product will change shape or size if the ZnO precursor template's shape or size is changed.

The first attempt to change the ZnO precursor involved synthesizing 4 nm ZnO nanoparticles which were used in the synthesis in place of the 10 nm ZnO nanoparticles. Some considerations for smaller nanoparticle precursors are whether or not the zinc will evaporate faster if the particle is smaller, also whether more or less $ZnGa_2O_4$ particles come in contact with ZnO nanoparticles if they are smaller. The $(Ga_{1-x}Zn_x)(N_{1-x}O_x)$ synthesis was done with both the 10 nm and the 4 nm ZnO precursors and the results were compared. Figure 2 shows TEM images of the 4 nm ZnO nanoparticles and both final $(Ga_{1-x}Zn_x)(N_{1-x}O_x)$ products.

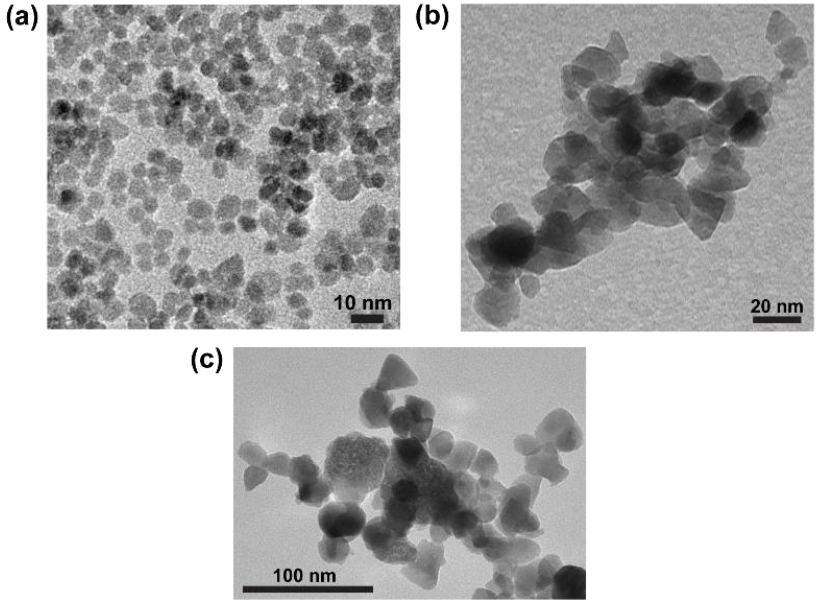

Figure 2.2: TEM images of (a) 4 nm ZnO nanoparticle precursor, (b) x=0.56 $(Ga_{1-x}Zn_x)(N_{1-x}O_x)$ synthesized using the 4 nm ZnO, and (c) x=0.54 $(Ga_{1-x}Zn_x)(N_{1-x}O_x)$ synthesized using the 10 nm ZnO.

By analyzing the TEM images taken, samples of which are shown in Figure 2, it was determined that using the 4 nm ZnO instead of the 10 nm ZnO did not seem to make a difference in the size or shape of the final $(Ga_{1-x}Zn_x)(N_{1-x}O_x)$ product, shown in Figure 2(b) and (c). We hypothesized that the reason changing the size of the ZnO nanoparticle precursor had no effect is because at such high synthesis temperatures the precursors must fuse together in some way. So, having a slightly smaller ZnO nanoparticle may not have made a difference if, for example, two 4 nm ZnO nanoparticles fused together, in which case the starting size of the ZnO precursor effectively would not have changed much. Moving forward, we aimed to study if changing the shape of the ZnO precursor could change the $(Ga_{1-x}Zn_x)(N_{1-x}O_x)$ product.

The attempt at changing the ZnO precursor shape was accomplished by synthesizing ZnO nanorods and attempting to use them in place of the 10 nm nanoparticles. We hypothesized that perhaps the $ZnGa_2O_4$ would attach at multiple points along the ZnO nanorod allowing not only for a different product shape, but also perhaps a different elemental distribution in the product. The ZnO nanorods were synthesized via a solution phase hot-injection synthesis which produced the carrot-shaped nanorods, seen in Figure 3(a). The ZnO nanorods in Figure 3(a) were used as the ZnO precursor for a $(Ga_{1-x}Zn_x)(N_{1-x}O_x)$ synthesis, the product of which is shown in the TEM image in Figure 3(b).

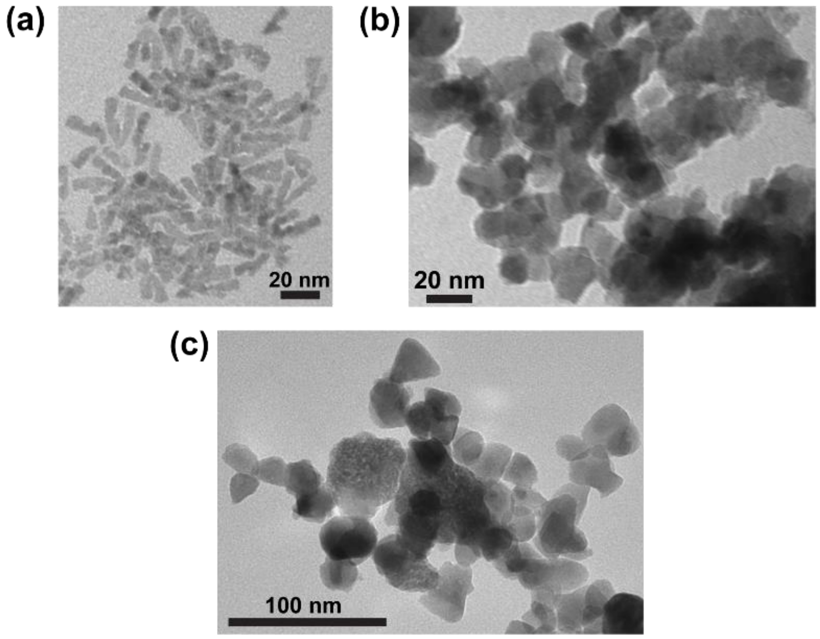

Figure 2.3: TEM images of (a) ZnO nanorod precursor made via hot-injection synthesis, (b) x=0.52 $(Ga_{1-x}Zn_x)(N_{1-x}O_x)$ product synthesized with ZnO nanorods as the ZnO precursor, and (c) x=0.54 $(Ga_{1-x}Zn_x)(N_{1-x}O_x)$ synthesized using the 10 nm ZnO nanoparticles.

Comparing the $(Ga_{1-x}Zn_x)(N_{1-x}O_x)$ product in Figure 3(b) and (c), there do not appear to be any major differences, which is similar to what we saw when 4 nm ZnO was used as the ZnO precursor. The $(Ga_{1-x}Zn_x)(N_{1-x}O_x)$ product made with the ZnO nanorods (Figure 3(b)) does not show any size or shape difference from the $(Ga_{1-x}Zn_x)(N_{1-x}O_x)$ made with 4 nm ZnO (Figure 3(b)) or from the $(Ga_{1-x}Zn_x)(N_{1-x}O_x)$ made with 10 nm ZnO (Figure 3(c)). This finding supports the hypothesis that at such high reaction temperatures, all of the precursors may be fusing together, so changing the ZnO precursor size or shape might not affect the $(Ga_{1-x}Zn_x)(N_{1-x}O_x)$ product, since multiple ZnO precursors could be fusing together, or the ZnO nanorod could fuse into a more spherical particle shape at the high reaction temperatures.

2.3.3 Surface Functionalization of $(Ga_{1-x}Zn_x)(N_{1-x}O_x)$ with Ligands

In addition to investigating the $(Ga_{1-x}Zn_x)(N_{1-x}O_x)$ synthesis, we also wanted to investigate how we can functionalize the $(Ga_{1-x}Zn_x)(N_{1-x}O_x)$ surface. In nanoscience this usually means attaching some kind of ligand to the surface of the nanocrystal, but it can also mean attaching a cocatalyst or metal nanoparticle. One of the biggest challenges throughout our research into $(Ga_{1-x}Zn_x)(N_{1-x}O_x)$ has been trying to attach a ligand to the nanocrystal surface. We have found two ligands that will bind to the surface to some extent which allows some solution dispersion, but even those ligands do not result in fully soluble particles. Below we will investigate what worked, what did not work, and why we are having trouble functionalizing the surface.

2.3.3.1 ODTMS

We will begin with ODTMS because it has been the most successful ligand and the one we use the most in our experiments. As depicted in Figure 4, the ODTMS molecule has a long alkane tail with 18 carbons and a head group of Si with three methoxy groups attached. The long alkane chain is what allows the modified particles to be soluble in non-polar solvents, while the head group is the part of the molecule that attaches to the $(Ga_{1-x}Zn_x)(N_{1-x}O_x)$ surface.

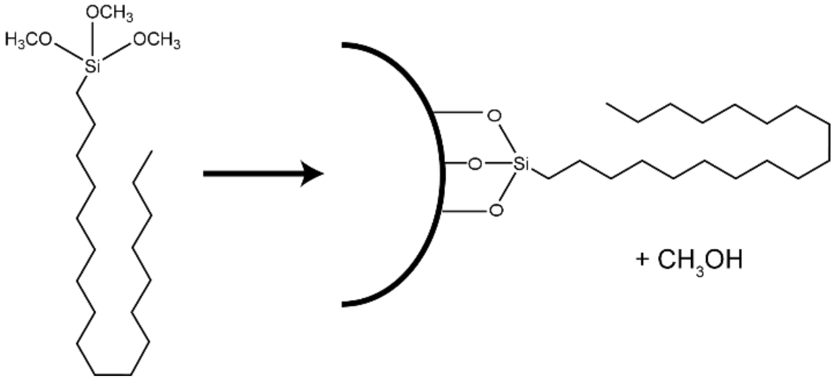

Figure 2.4: Illustration of how the ODTMS molecule attaches to the $(Ga_{1-x}Zn_x)(N_{1-x}O_x)$ surface.

Functionalization with ODTMS was semi successful for our purposes because it reacts with the OH groups on the $(Ga_{1-x}Zn_x)(N_{1-x}O_x)$ surface. However, it was only partially successful considering that we see about a 20-30% yield of solubilization. We hypothesize that this low yield of solubilization is because there are most likely NH groups on the $(Ga_{1-x}Zn_x)(N_{1-x}O_x)$ surface in addition to the OH groups and the ODTMS does not react with the NH groups. One of the benefits of ODTMS is that it is in an ideal reactivity range of silanes because it is reactive enough to interact with the $(Ga_{1-x}Zn_x)(N_{1-x}O_x)$ surface, but not so reactive that it prefers to polymerize instead of attaching to the $(Ga_{1-x}Zn_x)(N_{1-x}O_x)$ surface.

2.3.3.2 APTES

APTES is a similar ligand to ODTMS. They both have very similar reactivities, similar head groups, but different tail groups – APTES has an aminopropyl tail. The main use we have for the APTES ligand is to use it to functionalize the $(Ga_{1-x}Zn_x)(N_{1-x}O_x)$ surface and then deposit a metal nanoparticle cocatalyst on the amine at the end of the APTES tail group. This is an indirect way to attach a metal nanoparticle cocatalyst to the $(Ga_{1-x}Zn_x)(N_{1-x}O_x)$ surface and can be useful for comparisons in photocatalytic studies. Figure 5 shows an example of how APTES can be used to functionalize a surface and then have Pt attached to the amine end of the APTES ligand. ZnO is used in place of $(Ga_{1-x}Zn_x)(N_{1-x}O_x)$ as a model system.

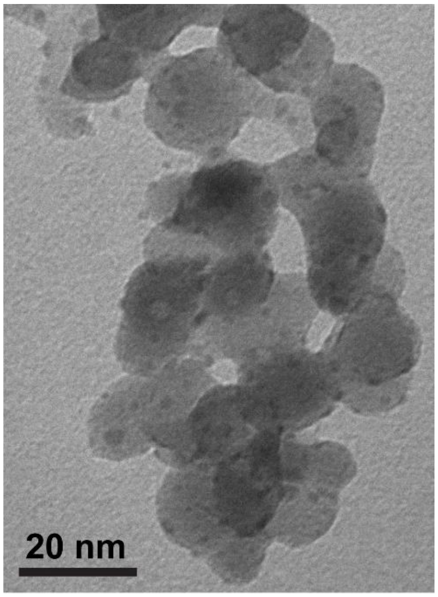

Figure 2.5: TEM image of ZnO functionalized with APTES ligands which subsequently had Pt attached to the amine end of the APTES ligand.

2.3.3.3 OTS

OTS was investigated as a possible ligand for $(Ga_{1-x}Zn_x)(N_{1-x}O_x)$ due to ODTMS having low yields. The initial hypothesis was that since OTS is more reactive than ODTMS it might have a greater number of successful molecules that would bind to the $(Ga_{1-x}Zn_x)(N_{1-x}O_x)$ surface than ODTMS. However, this was not the case. In fact, due to OTS being more reactive than ODTMS, it preferred to react with itself and polymerize than to react with the $(Ga_{1-x}Zn_x)(N_{1-x}O_x)$ surface. This was evidence that the poor yield of ODTMS attachment did not have to do with the reactivity of the ligand and led us to wonder if it was more to do with what was on the $(Ga_{1-x}Zn_x)(N_{1-x}O_x)$ surface. This supported our thoughts that maybe there were not enough OH groups on the $(Ga_{1-x}Zn_x)(N_{1-x}O_x)$ surface because there were also NH groups that the OTS and ODTMS could not react with.

2.3.3.4 NOBF$_4$

$NOBF_4$ functionalization experiments were based on the paper by Dong et al.,[29] which offered a facile way to ligand exchange colloidal nanocrystals from non-polar to polar phases and back. The premise is that if one has nanocrystals already soluble in a non-polar solvent, most likely because they have native ligands on them, then $NOBF_4$ can be added to the solution and it will exchange with the non-polar ligand and make the nanocrystals soluble in a polar solvent. From there the researcher is free to ligand exchange the nanocrystal to a different ligand, or to keep the $NOBF_4$ functionalized particles. $NOBF_4$ functionalization was not successful with $(Ga_{1-x}Zn_x)(N_{1-x}O_x)$, no soluble particles were obtained. Our hypothesis for why the $NOBF_4$ functionalization did not work for $(Ga_{1-x}Zn_x)(N_{1-x}O_x)$ is because the nanocrystals were not soluble to begin with, so there was no ligand exchange that could happen. The only groups available for exchange would be OH and/or NH and it would be unlikely for the OH or NH groups on the $(Ga_{1-x}Zn_x)(N_{1-x}O_x)$ surface to participate in a ligand exchange process considering it would be less favorable for the OH and NH groups to detach from the $(Ga_{1-x}Zn_x)(N_{1-x}O_x)$ surface and be free in solution than it would be for them to stay on the surface. Conversely, when colloidal Cd chalcogenide nanocrystals, for example, are synthesized they tend to be functionalized with long-chain alkane ligands that are more stable as free molecules in solution, so would be more likely to ligand exchange with something like $NOBF_4$.

2.3.3.5 ODPA

Surface modification using ODPA as a ligand was attempted using a previously reported process by Yee et al.,[30] which states that a sulfonic acid group binds to the Fe_2O_3 nanoparticle surface through an acid-base reaction between the Fe-OH and S-OH groups, and the reader is left to assume that the binding of the phosphonic acid group may occur through an acid-base reaction between Fe-OH and P-OH groups as well. Since Yee et al.[30] reported the successful functionalization of the Fe_2O_3 surface with ODPA, we hypothesized that we might be able to use ODPA to functionalize the $(Ga_{1-x}Zn_x)(N_{1-x}O_x)$ surface. However, just like other techniques failed, the ODPA did not appear to bind to the $(Ga_{1-x}Zn_x)(N_{1-x}O_x)$ surface and no usable functionalized $(Ga_{1-x}Zn_x)(N_{1-x}O_x)$ particles were produced. Again, the hypothesis for why this functionalization failed is based on the assumption that there probably are not enough OH groups on the $(Ga_{1-x}Zn_x)(N_{1-x}O_x)$ surface to react with the ODPA ligands. We presume that ODTMS and APTES are semi-successful because they may be more reactive with the few OH groups that are on the $(Ga_{1-x}Zn_x)(N_{1-x}O_x)$ surface than the other ligands are. The failure of ODPA functionalization heavily emphasized the need to hydroxylate the $(Ga_{1-x}Zn_x)(N_{1-x}O_x)$ surface with more OH groups.

2.3.3.6 Hydroxylating the $(Ga_{1-x}Zn_x)(N_{1-x}O_x)$ Surface

Due to the lack of any ligands besides ODTMS and APTES successfully attaching to the $(Ga_{1-x}Zn_x)(N_{1-x}O_x)$ surface, we investigated the possibility of hydroxylating the $(Ga_{1-x}Zn_x)(N_{1-x}O_x)$ surface by treatment with concentrated NaOH. Treating the $(Ga_{1-x}Zn_x)(N_{1-x}O_x)$ surface with concentrated NaOH was the simplest procedure for hydroxylating the surface that could be found considering that other procedures involved either plasma treatment or treatment with Piranha (H_2SO_4 and H_2O_2). However, it is important to note that $(Ga_{1-x}Zn_x)(N_{1-x}O_x)$ will be digested by concentrated NaOH with long enough exposure times (>18 hours). The hydroxylation experiments were attempted but a balance between enough time for hydroxylation and not enough time for digestion was not found. The hydroxylation experiments were attempted in conjunction with other functionalization experiments whose mechanisms involved reaction with OH groups, but the NaOH treatment did not appear to help any of the other functionalization processes succeed. The final assumption was that the amount of concentrated NaOH and time necessary to start to hydroxylate the $(Ga_{1-x}Zn_x)(N_{1-x}O_x)$ surface was too close to the point where the $(Ga_{1-x}Zn_x)(N_{1-x}O_x)$

would start to be digested by the base. It is possible that the plasma treatment or the Piranha treatment might be more successful because those treatments are much more intense than NaOH, and it might be possible to do them for significantly less time, which could help avoid the digestion of the $(Ga_{1-x}Zn_x)(N_{1-x}O_x)$ particles.

2.3.3.7 Pt Photodeposition on $(Ga_{1-x}Zn_x)(N_{1-x}O_x)$ Surface

Another option for surface functionalization besides attaching ligands is to deposit a metal nanoparticle cocatalyst on the $(Ga_{1-x}Zn_x)(N_{1-x}O_x)$ surface. This was accomplished by photodepositing Pt nanoparticles on the $(Ga_{1-x}Zn_x)(N_{1-x}O_x)$ surface. Figure 6(a) shows high-resolution TEM images of Pt nanoparticles photodeposited on $(Ga_{1-x}Zn_x)(N_{1-x}O_x)$ particles and Figure 6(b) shows the crystal lattice of the Pt nanoparticle attached to the crystal lattice of the $(Ga_{1-x}Zn_x)(N_{1-x}O_x)$ with the lattice lines emphasized in yellow. The d-spacing measured for $(Ga_{1-x}Zn_x)(N_{1-x}O_x)$ is 2.6 Å and for Pt is 2.28 Å.

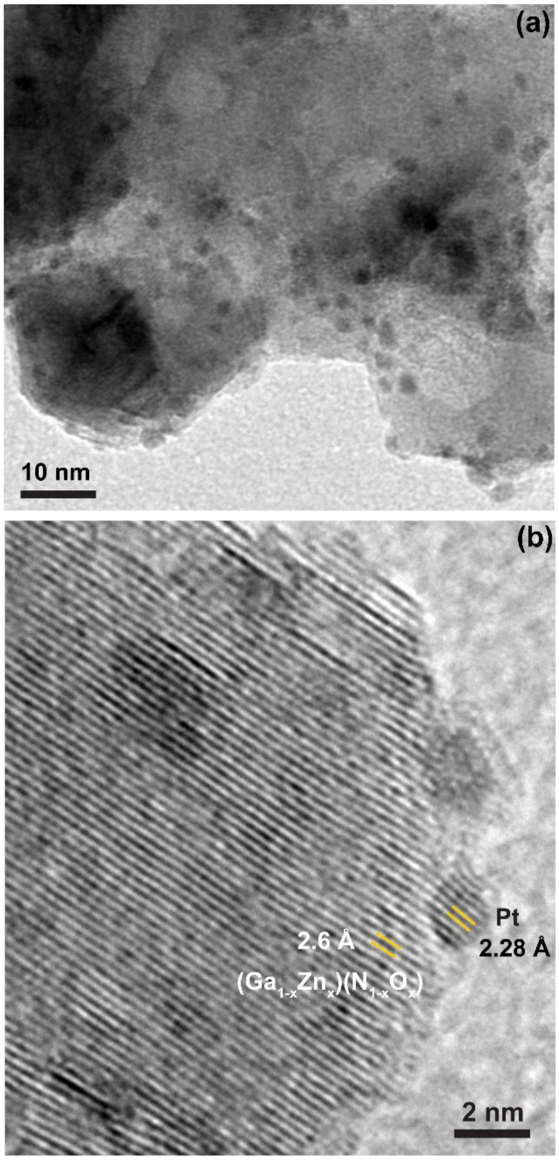

Figure 2.6: (a) High-resolution TEM image showing Pt nanoparticles photodeposited on $(Ga_{1-x}Zn_x)(N_{1-x}O_x)$ particles. (b) High-resolution TEM image showing the Pt nanoparticle crystal lattice attached to the $(Ga_{1-x}Zn_x)(N_{1-x}O_x)$ crystal lattice. The lattice lines are emphasized in yellow and the d-spacings are notated, 2.6 Å for $(Ga_{1-x}Zn_x)(N_{1-x}O_x)$ and 2.28 Å for Pt.

Figure 6(b) shows that the Pt photodeposition was successful, with the crystal lattices of the Pt and the $(Ga_{1-x}Zn_x)(N_{1-x}O_x)$ clearly merging. Unfortunately, H_2 production attempted with the photodeposited sample was not successful. The lack of H_2 production success was likely due to the lack of an efficient hole scavenger and being in a non-ideal pH range. Follow up experiments with more efficient hole scavengers in a pH 3 buffer are predicted to yield better H_2 production results, however these experiments have not been attempted yet.

2.4 Conclusion and Outlook

Throughout the study of $(Ga_{1-x}Zn_x)(N_{1-x}O_x)$ synthesis and surface functionalization we have learned that the reaction temperature can change the elemental distribution in the $(Ga_{1-x}Zn_x)(N_{1-x}O_x)$ particles, with lower temperatures (650 °C) resulting in heterogeneous "core/shell-like" particles and higher temperatures (800 °C) resulting in homogeneous particles. We also learned that changing the ZnO precursor size and shape does not affect the size or shape of the $(Ga_{1-x}Zn_x)(N_{1-x}O_x)$ product. Two separate syntheses were attempted, one using 4 nm ZnO nanoparticles and the other using ZnO nanorods, neither of which resulted in a different $(Ga_{1-x}Zn_x)(N_{1-x}O_x)$ product than the original synthesis using 10 nm ZnO nanoparticles. Attempts to functionalize the $(Ga_{1-x}Zn_x)(N_{1-x}O_x)$ surface led to the hypothesis that the surface may have NH groups in addition to OH groups on it, which can limit the effectiveness of surface functionalization techniques that depend on a reaction with a OH group. The two semi-successful surface functionalization procedures use ODTMS and APTES as ligands, and it is hypothesized that these ligands were successful because they may react more strongly with the OH groups that were present than the other ligands that were investigated. The ligands that failed to functionalize the $(Ga_{1-x}Zn_x)(N_{1-x}O_x)$ surface include ODPA, $NOBF_4$ and OTS. Additionally, attempting to hydroxylate the $(Ga_{1-x}Zn_x)(N_{1-x}O_x)$ surface with concentrated NaOH was also unsuccessful because it digested the $(Ga_{1-x}Zn_x)(N_{1-x}O_x)$ particles before it effectively hydroxylated their surface. Lastly, functionalizing the $(Ga_{1-x}Zn_x)(N_{1-x}O_x)$ surface with a metal nanoparticle cocatalyst was successful. Pt nanoparticles were successfully photodeposited on the $(Ga_{1-x}Zn_x)(N_{1-x}O_x)$ surface using a photochemical deposition technique.[31-32] It was confirmed that the Pt nanoparticles were directly attached to the $(Ga_{1-x}Zn_x)(N_{1-x}O_x)$ through HRTEM, which showed the two crystal lattices merging. These studies have served to emphasize the need to more successfully functionalize the $(Ga_{1-x}Zn_x)(N_{1-x}O_x)$ surface, whether it is by finding a ligand that will react with both NH and OH groups, or whether it is by finding a way to successfully hydroxylate the $(Ga_{1-x}Zn_x)(N_{1-x}O_x)$ surface without destroying the particles. Additionally, the limitations of the solid-state synthesis have been highlighted by the inability to change the size or shape of the $(Ga_{1-x}Zn_x)(N_{1-x}O_x)$ product. It is necessary to investigate other synthesis techniques like solution-phase and solvothermal synthesis in order to be able to control the size and shape of the $(Ga_{1-x}Zn_x)(N_{1-x}O_x)$ product more readily.

2.5 References

(1) Maeda, K.; Teramura, K.; Takata, T.; Hara, M.; Saito, N.; Toda, K.; Inoue, Y.; Kobayashi, H.; Domen, K., Overall Water Splitting on $(Ga_{1-x}Zn_x)(N_{1-x}O_x)$ Solid Solution Photocatalyst: Relationship between Physical Properties and Photocatalytic Activity. *Journal of Physical Chemistry B* **2005**, *109*, 20504-20510.

(2) Maeda, K.; Teramura, K.; Lu, D.; Takata, T.; Saito, N.; Inoue, Y.; Domen, K., Characterization of Rh−Cr Mixed-Oxide Nanoparticles Dispersed on $(Ga_{1-x}Zn_x)(N_{1-x}O_x)$ as a Cocatalyst for Visible-Light-Driven Overall Water Splitting. *Journal of Physical Chemistry B* **2006**, *110*, 13753-13758.

(3) Maeda, K.; Teramura, K.; Lu, D. L.; Takata, T.; Saito, N.; Inoue, Y.; Domen, K., Photocatalyst releasing hydrogen from water - Enhancing catalytic performance holds promise for hydrogen production by water splitting in sunlight. *Nature* **2006**, *440*, 295-295.

(4) Maeda, K.; Teramura, K.; Masuda, H.; Takata, T.; Saito, N.; Inoue, Y.; Domen, K., Efficient Overall Water Splitting under Visible-Light Irradiation on $(Ga_{1-x}Zn_x)(N_{1-x}O_x)$ Dispersed with Rh−Cr Mixed-Oxide Nanoparticles: Effect of Reaction Conditions on Photocatalytic Activity. *Journal of Physical Chemistry B* **2006**, *110*, 13107-13112.

(5) Maeda, K.; Domen, K., New Non-Oxide Photocatalysts Designed for Overall Water Splitting under Visible Light. *Journal of Physical Chemistry C* **2007**, *111*, 7851-7861.

(6) Maeda, K.; Hashiguchi, H.; Masuda, H.; Abe, R.; Domen, K., Photocatalytic Activity of $(Ga_{1-x}Zn_x)(N_{1-x}O_x)$ for Visible-Light-Driven H_2 and O_2 Evolution in the Presence of Sacrificial Reagents. *Journal of Physical Chemistry C* **2008**, *112*, 3447-3452.

(7) Maeda, K.; Takata, T.; Hara, M.; Saito, N.; Inoue, Y.; Kobayashi, H.; Domen, K., GaN:ZnO Solid Solution as a Photocatalyst for Visible-Light-Driven Overall Water Splitting. *Journal of the American Chemical Society* **2005**, *127*, 8286-8287.

(8) Chen, H.; Wen, W.; Wang, Q.; Hanson, J. C.; Muckerman, J. T.; Fujita, E.; Frenkel, A. I.; Rodriguez, J. A., Preparation of $(Ga_{1-x}Zn_x)(N_{1-x}O_x)$ Photocatalysts from the Reaction of NH_3 with Ga_2O_3/ZnO and $ZnGa_2O_4$: *In Situ* Time-Resolved XRD and XAFS Studies. *Journal of Physical Chemistry C* **2009**, *113*, 3650-3659.

(9) Han, W.-Q.; Liu, Z.; Yu, H.-G., Synthesis and Optical Properties of GaN/ZnO Solid Solution Nanocrystals. *Applied Physics Letters* **2010**, *96*, 183112.

(10) Wang, J.; Huang, B.; Wang, Z.; Wang, P.; Cheng, H.; Zheng, Z.; Qin, X.; Zhang, X.; Dai, Y.; Whangbo, M.-H., Facile Synthesis of Zn-rich $(GaN)_{1-x}(ZnO)_x$ Solid Solutions Using Layered Double Hydroxides as Precursors. *Journal of Materials Chemistry* **2011**, *21*, 4562-4567.

(11) Hahn, C.; Fardy, M. A.; Nguyen, C.; Natera-Comte, M.; Andrews, S. C.; Yang, P. D., Synthesis and Photocatalytic Properties of Single Crystalline $(Ga_{1-x}Zn_x)(N_{1-x}O_x)$ Nanotubes. *Israel Journal of Chemistry* **2012**, *52*, 1111-1117.

(12) Martha, S.; Reddy, K. H.; Parida, K. M.; Satapathy, P. K., Enhanced photocatalytic activity over N-doped GaZn mixed oxide under visible light irradiation. *International Journal of Hydrogen Energy* **2012**, *37*, 115-124.

(13) Adeli, B.; Taghipour, F., A Review of Synthesis Techniques for Gallium-Zinc Oxynitride Solar-Activated Photocatalyst for Water Splitting. *ECS J. Solid State Sci. Technol.* **2013**, *2*, Q118-Q126.

(14) RajaAmbal, S.; Yadav, A. K.; Jha, S. N.; Bhattacharyya, D.; Gopinath, C. S., Electronic structure-sunlight driven water splitting activity correlation of $(Zn_{1-y}Ga_y)(O_{1-z}N_z)$. *Physical Chemistry Chemical Physics* **2014**, *16*, 23654-23662.

(15) Dharmagunawardhane, H. A. N.; James, A.; Wu, Q.; Woerner, W. R.; Palomino, R. M.; Sinclair, A.; Orlov, A.; Parise, J. B., Unexpected visible light driven photocatalytic activity without cocatalysts and sacrificial reagents from a $(GaN)_{1-x}(ZnO)_x$ solid solution synthesized at high pressure over the entire composition range. *RSC Advances* **2018**, *8*, 8976-8982.

(16) Ren, B.; Zhang, X.; Zhao, M.; Wang, X.; Ye, J.; Wang, D., Significant enhancement in photocatalytic activity of $(GaN)_{1-x}(ZnO)_x$ nanowires via solubility and crystal facet tailoring. *AIP Advances* **2018**, *8*, 015206.

(17) Ford, G. M.; Guo, Q.; Agrawal, R.; Hillhouse, H. W., Earth Abundant Element Cu2Zn(Sn1−xGex)S4 Nanocrystals for Tunable Band Gap Solar Cells: 6.8% Efficient Device Fabrication. *Chemistry of Materials* **2011**, *23*, 2626-2629.

(18) Fan, F.-J.; Wu, L.; Yu, S.-H., Energetic I–III–VI2 and I2–II–IV–VI4 nanocrystals: synthesis, photovoltaic and thermoelectric applications. *Energy & Environmental Science* **2014**, *7*, 190-208.

(19) Wei, S.-Y.; Liao, Y.-C.; Hsu, C.-H.; Cai, C.-H.; Huang, W.-C.; Huang, M.-C.; Lai, C.-H., Achieving high efficiency Cu2ZnSn(S,Se)4 solar cells by non-toxic aqueous ink: Defect analysis and electrical modeling. *Nano Energy* **2016**, *26*, 74-82.

(20) Tongying, P.; Lu, Y.-G.; Hall, L. M. G.; Lee, K.; Sulima, M.; Ciston, J.; Dukovic, G., Control of Elemental Distribution in the Nanoscale Solid-State Reaction That Produces $(Ga_{1-x}Zn_x)(N_{1-x}O_x)$ Nanocrystals. *ACS Nano* **2017**, *11*, 8401-8412.

(21) Chuang, C.-H.; Lu, Y.-G.; Lee, K.; Ciston, J.; Dukovic, G., Strong Visible Absorption and Broad Time Scale Excited-State Relaxation in $(Ga_{1-x}Zn_x)(N_{1-x}O_x)$ Nanocrystals. *Journal of the American Chemical Society* **2015**, *137*, 6452-6455.

(22) Lee, K.; Tienes, B. M.; Wilker, M. B.; Schnitzenbaumer, K. J.; Dukovic, G., $(Ga_{1-x}Zn_x)(N_{1-x}O_x)$ Nanocrystals: Visible Absorbers with Tunable Composition and Absorption Spectra. *Nano Letters* **2012**, *12*, 3268-3272.

(23) Schwartz, D. A.; Norberg, N. S.; Nguyen, Q. P.; Parker, J. M.; Gamelin, D. R., Magnetic Quantum Dots: Synthesis, Spectroscopy, and Magnetism of Co2+- and Ni2+-Doped ZnO Nanocrystals. *Journal of the American Chemical Society* **2003**, *125*, 13205-13218.

(24) Tienes, B. M.; Perkins, R. J.; Shoemaker, R. K.; Dukovic, G., Layered Phosphonates in Colloidal Synthesis of Anisotropic ZnO Nanocrystals. *Chemistry of Materials* **2013**, *25*, 4321-4329.

(25) Saengdee, P.; Chaisriratanakul, W.; Bunjongpru, W.; Sripumkhai, W.; Srisuwan, A.; Jeamsaksiri, W.; Hruanun, C.; Poyai, A.; Promptmas, C., Surface modification of silicon dioxide, silicon nitride and titanium oxynitride for lactate dehydrogenase immobilization. *Biosensors and Bioelectronics* **2015**, *67*, 134-138.

(26) Rabin Nurun, N., et al., Surface Modification of the ZnO Nanoparticles with γ-Aminopropyltriethoxysilane and Study of Their Photocatalytic Activity, Optical Properties and Antibacterial Activities. In *International Journal of Chemical Reactor Engineering*, 2016; Vol. 14, p 785.

(27) Liu, Y.; Li, Y.; Li, X.-M.; He, T., Kinetics of (3-Aminopropyl)triethoxylsilane (APTES) Silanization of Superparamagnetic Iron Oxide Nanoparticles. *Langmuir* **2013**, *29*, 15275-15282.

(28) Grasset, F.; Saito, N.; Li, D.; Park, D.; Sakaguchi, I.; Ohashi, N.; Haneda, H.; Roisnel, T.; Mornet, S.; Duguet, E., Surface modification of zinc oxide nanoparticles by aminopropyltriethoxysilane. *Journal of Alloys and Compounds* **2003**, *360*, 298-311.

(29) Dong, A.; Ye, X.; Chen, J.; Kang, Y.; Gordon, T.; Kikkawa, J. M.; Murray, C. B., A Generalized Ligand-Exchange Strategy Enabling Sequential Surface Functionalization of Colloidal Nanocrystals. *Journal of the American Chemical Society* **2011**, *133*, 998-1006.

(30) Yee, C.; Kataby, G.; Ulman, A.; Prozorov, T.; White, H.; King, A.; Rafailovich, M.; Sokolov, J.; Gedanken, A., Self-Assembled Monolayers of Alkanesulfonic and -phosphonic Acids on Amorphous Iron Oxide Nanoparticles. *Langmuir* **1999**, *15*, 7111-7115.

(31) Carabineiro, S. A. C.; Machado, B. F.; Dražić, G.; Bacsa, R. R.; Serp, P.; Figueiredo, J. L.; Faria, J. L., Photodeposition of Au and Pt on ZnO and TiO2. In *Studies in Surface Science and Catalysis*, Gaigneaux, E. M.; Devillers, M.; Hermans, S.; Jacobs, P. A.; Martens, J. A.; Ruiz, P., Eds. Elsevier: 2010; Vol. 175, pp 629-633.

(32) Cavalca, F.; Laursen, A. B.; Kardynal, B. E.; Dunin-Borkowski, R. E.; Dahl, S.; Wagner, J. B.; Hansen, T. W., In situtransmission electron microscopy of light-induced photocatalytic reactions. *Nanotechnology* **2012**, *23*, 075705.

Chapter 3: Understanding Photochemical H_2 Generation from $(Ga_{1-x}Zn_x)(N_{1-x}O_x)$ Nanocrystals

3.1 Introduction

As the demand for renewable energy intensifies, a variety of different semiconductors are being synthesized for use in renewable energy production.[1] Semiconductors are widely used in renewable energy applications ranging from battery development and photovoltaics to solar fuel generation.[2-5] Recently, solid-state, multinary compounds have become a popular path for synthetic investigation for use in these applications.[6] One of these modern, multinary compounds is $(Ga_{1-x}Zn_x)(N_{1-x}O_x)$, a solid solution of GaN and ZnO, first synthesized in the bulk by the Domen group in 2005.[7] Early studies of $(Ga_{1-x}Zn_x)(N_{1-x}O_x)$ showed optimistic performance in light-driven water splitting when modified with appropriate cocatalysts.[8-18] $(Ga_{1-x}Zn_x)(N_{1-x}O_x)$ has a bandgap in the visible region, even though the parent materials, GaN and ZnO, have bandgaps in the UV region.[19-31] A visible bandgap is more useful for solar fuel and photovoltaic applications than a bandgap in the UV because it allows the material to use a greater percentage of solar radiation.[32] $(Ga_{1-x}Zn_x)(N_{1-x}O_x)$ is also interesting in terms of synthesis because most researchers who have synthesized it have used solid state techniques.[15, 33-36] These syntheses afford diverse options for synthetic control over materials such as elemental and compositional distribution control. Learning how to implement materials synthesized via solid state techniques in solar applications could unlock a new category of materials for solar energy applications.

We recently succeeded in synthesizing nanoscale $(Ga_{1-x}Zn_x)(N_{1-x}O_x)$, in the form of wurtzite nanocrystals (NCs) that are ~20 nm in diameter.[37] After successfully synthesizing nanoscale $(Ga_{1-x}Zn_x)(N_{1-x}O_x)$ in the solid state and characterizing the NC product,[38] we ventured into studying $(Ga_{1-x}Zn_x)(N_{1-x}O_x)$ as a light absorber for photochemical H_2 generation. While, $(Ga_{1-x}Zn_x)(N_{1-x}O_x)$ is a promising light absorber for photochemical systems due to its relatively large molar absorptivity,[39] it has so far shown poor solar conversion efficiencies and researchers report poor quantum yields (QYs) of water splitting.[14, 40-43] One contributor to the poor QY of water splitting by $(Ga_{1-x}Zn_x)(N_{1-x}O_x)$ could be a lack of catalytic surface sites to catalyze the H^+ reduction and water oxidation reactions. However, researchers found that even when both water oxidation and H^+ reduction reactions are catalyzed, the QYs of water splitting were still low compared to other results from the solar community.[44] Therefore, we investigated the factors that determine the overall efficiency.

In this Chapter, we quantify the rates of the elementary charge-transfer steps involved in photochemical H_2 production by $(Ga_{1-x}Zn_x)(N_{1-x}O_x)$ in order to evaluate the factors that determine the overall QY. The H_2 production system consists of $(Ga_{1-x}Zn_x)(N_{1-x}O_x)$ as the light absorber, methyl viologen (MV) as the electron shuttle/redox mediator, Pt as the cocatalyst, and dithioerythritol (DTE) as the sacrificial hole scavenger. H_2 production in this system relies on several elementary steps: electron transfer from $(Ga_{1-x}Zn_x)(N_{1-x}O_x)$ to MV^{2+}, subsequent electron transfer from $MV^{+\bullet}$ to Pt nanoparticle (NP) cocatalyst, H_2 production catalyzed by the Pt NP cocatalyst, and hole scavenging by DTE. We isolate each of these processes and determine the rates of each charge-transfer event as well as the catalysis. We find that while electron transfer from the redox mediator to the cocatalyst is fast and efficient, electron transfer from the $(Ga_{1-x}Zn_x)(N_{1-x}O_x)$ NP to the redox mediator is inefficient and the turnover of the cocatalyst to produce H_2 is average. We hypothesize that this inefficiency is due to a conduction band minimum energy that is too low to drive efficient electron transfer. This indicates that electron transfer from the

$(Ga_{1-x}Zn_x)(N_{1-x}O_x)$ NP to the redox mediator is the most significant contributor to the overall poor efficiency of H_2 production.

3.2 Materials and Methods

3.2.1 Chemicals

3-mercaptopropionic acid (3-MPA, ≥99.0%), 1,2-hexadecanediol (90%), benzyl ether (98%), oleic acid (≥99.0%), oleylamine (70%), tetramethylammonium hydroxide pentahydrate (≥97%), zinc acetylacetonate hydrate ($Zn(acac)_2$, 99.995%), gallium acetylacetonate ($Ga(acac)_3$, 99.99%), zinc chloride ($ZnCl_2$, ≥98%), poly(vinyl alcohol) (avg MW 13,000-23,000 Da, 98% hydrolyzed), sodium oxalate (99.99)%, oxalic acid (98%), sodium formate (99.998%), L-cysteine (98%), 1,4-dithioerythritol (DTE) (≥99.0%), triethanolamine (≥99.0%), 2-mercaptoethanol (≥98%), chloroplatinic acid hydrate (99.9%), citric acid trisodium salt (≥98%), methyl viologen dichloride hydrate (98%), sodium hydrosulfite (dithionite) (85%), hexane (99%), toluene (99.5%), 4-(2-hydroxyethyl)-1-piperazineethanesulfonic acid (HEPES, ≥99.5%), and tris(hydroxymethyl)methylamino]propanesulfonic acid (TAPS, ≥99.5%) were purchased from Sigma-Aldrich. 2-(N-morpholino)ethanesulfonic acid (MES Free Acid Monohydrate, 98%), 2-propanol (99.9%), methanol (99.9%), and sodium hydroxide (NaOH pellets, 99.3%) were purchased from Fisher. 1,2-ethanediol (99.8%) was purchased from Macron Fine Chemicals. Ethanol (95%) was purchased from Decon Labs. Ammonia (99.99%) was purchased from Airgas. Sodium borohydride (≥98%) was purchased from VWR. D, L-dithiothreitol (DTT) (≥99%) was purchased from Research Products International. All chemicals were purchased commercially and used without further purification.

3.2.2 $ZnGa_2O_4$ Nanocrystal Synthesis

$ZnGa_2O_4$ NCs were synthesized as detailed in Chapter 2.

3.2.3 $(Ga_{1-x}Zn_x)(N_{1-x}O_x)$ Nanocrystal Synthesis

$(Ga_{1-x}Zn_x)(N_{1-x}O_x)$ NCs and precursors were synthesized as reported previously.[37] Briefly, ~200 mg of $ZnGa_2O_4$ NC precursor was heated in a quartz tube furnace at 650°C for 10 hours under a flow of NH_3 (g) at ~150 mL/min. After 10 hours, the furnace was set to turn off and the sample was left in the furnace overnight to cool with NH_3 (g) still flowing. The next morning, the NH_3 (g) flow was turned off and the furnace was purged with Ar (g) before opening the furnace. The boats containing the product were removed from the furnace and the powder product in the boats was carefully poured into a 4 mL borosilicate vial. Once synthesized, the $(Ga_{1-x}Zn_x)(N_{1-x}O_x)$ NCs were characterized using inductively coupled plasma-mass spectrometry (ICP-MS) to analyze the Zn and Ga content, diffuse reflectance (DR) to obtain a reflectance spectrum which was converted using the Kubelka-Munk equation into the equivalent of an absorbance spectrum, powder X-ray diffraction (XRD) to analyze the crystal structure and crystallite domain size, and transmission electron microscopy (TEM) to obtain particle size and morphology data.

3.2.4 PVA-capped Pt Nanoparticle Synthesis

Poly(vinyl alcohol) (PVA)-capped Pt NPs were synthesized following the procedure by Wu and coworkers.[45] Briefly, 38 mL of 18 MΩ water was added to a beaker along with 1 mL of 16 mM H_2PtCl_6, and 1 mL of 40 mM trisodium citrate. The contents of the beaker were stirred for 30 minutes at room temperature and then 200 µL of 50 mM $NaBH_4$ was added dropwise and the mixture was allowed to stir and react at room temperature for 1 hour. Next, the Pt NPs were ligand exchanged from citrate to the protective agent PVA. PVA was added in a 1:1 mass ratio with Pt by first dissolving the solid PVA in water using sonication and then adding it to the completed reaction vessel and stirring overnight to ligand exchange. Lastly, the ligand-exchanged particles were purified with water using molecular weight (MW) cutoff filters and centrifugation. The Pt NP product was added to a 30 kDa MW cutoff filter and centrifuged at 4000 rpm for 10 minutes to concentrate the Pt NP product. This step was repeated until all of the NP product was in the top part of the filter and then the concentrated product was washed five times with 18 MΩ water, centrifuging at 4000 rpm for 10 minutes each time. The washed, concentrated product was diluted in 18 MΩ water and used without further modification.

3.2.5 Characterization

XRD patterns were collected with a PANalytical Empyrean diffractometer utilizing a Cu Kα radiation source (λ=0.15406 nm). Patterns were collected with a 2θ range of 20-85° and a step size of 0.029° 2θ. Diffuse reflectance spectra were collected using an Agilent Cary 60 UV-Vis spectrophotometer with the Agilent Cary 60 Remote Diffuse Reflectance Accessory (DRA). A Spectralon puck was used as the reference and the diffuse reflectance spectra were converted to Kubelka-Munk plots using the Kubelka-Munk equation: $F(R_\infty)=(1-R_\infty)^2/2R_\infty$, where $R_\infty=R_{sample}/R_{reference}$. UV-visible absorption spectra were collected on an Agilent Cary 60 UV-Vis spectrophotometer using 1 cm quartz cuvettes. A Thermo Finnigan Element2 magnetic sector ICP-MS was used to determine the amount of Zn and Ga in the sample, which was used to calculate the x-value. High-resolution TEM images were taken on a FEI Tecnai ST20 microscope operating at 200 kV. Low-magnification TEM images were taken on a FEI Tecnai T12 Spirit microscope operating at 100 kV.

3.2.6 Photocurrent onset and open circuit potential measurements

Experiments estimating the flat band potential via photocurrent onset were performed as described previously,[46] with a three-electrode cell utilizing $(Ga_{1-x}Zn_x)(N_{1-x}O_x)$/FTO as the working electrode, a Pt counter electrode, and Ag/AgCl as the reference electrode. The light source was a 300 W Xe-arc lamp (Newport 67005). An intensity of 1 sun was approximated by adjusting the distance between the working electrode and the light source using a $GaP_{0.98}N_{0.02}$ detector to determine the electrode location. The distance between the lamp and the electrode was set by choosing the distance at which the $GaP_{0.98}N_{0.02}$ detector read the same current as when it is under AM1.5G illumination. Next, the light was passed through a 435 nm long pass filter. The photocurrents were recorded from an oxidation sample in an aqueous 0.5 M Na_2SO_4 solution in phosphate buffer at pH 7.0. The photocurrent was collected by scanning the voltage from +1.0 V to -1.0 V at a rate of 10 mV/s with the light being chopped manually. Flat band potential values were calculated where the dark current and photocurrent intersected. Experiments estimating the flat band potential using open circuit potential measurements were performed in 0.1 M Na_2SO_4 at pH 7 in phosphate buffer with the same three electrode system described for the photocurrent onset experiments. A fiber optic illuminator was used as the light source which had tunable power between 0-8 sun. Open circuit potential values were gathered as the light power was increased. A final open circuit potential value was taken when the light power was strong enough to make the band bending flat. Flat band potentials were estimated by subtracting the difference between the final open circuit potential and the dark open circuit potential from the potential of the hydrogen half cell.

3.2.7 Light absorption by $(Ga_{1-x}Zn_x)(N_{1-x}O_x)$ and electron transfer to MV^{2+}

Experiments studying the reduction of MV^{2+} by $(Ga_{1-x}Zn_x)(N_{1-x}O_x)$ were performed in a 2 mm, air-free cuvette with a Kontes valve screw top cap and a stir bar. The total volume of the samples was 600 µL and each sample contained 2 mg of $(Ga_{1-x}Zn_x)(N_{1-x}O_x)$ powder, 5 mM MV^{2+}, 200 mM DTE, dispersed in either pH 3, 6, 7, or 8 100 mM MES/HEPES/TAPS buffer. Each sample was stirred while it was illuminated with a 447 nm diode laser (Laserglow LRD-0447 Collimated Diode Laser). Periodically, a UV-vis spectrum of the sample was collected using an Agilent Cary 60 UV-vis spectrophotometer. Using the absorbance at 604 nm of the characteristic $MV^{+\bullet}$ peak (ε_{604}=13,600 $M^{-1}cm^{-1}$)[47] and Beer's Law, a [$MV^{+\bullet}$] vs. time plot can be created. The UV-vis spectra were gathered at different time spacings depending on the sample pH. Since the higher pH samples reduced MV^{2+} more quickly than the pH 3 sample, spectra were gathered more quickly (30 seconds to 1 or 2 minutes between spectra) at high pH than the spectra for the lower pH samples (15 minutes between spectra). The time spacings also elongated as the illumination time increased and the [$MV^{+\bullet}$] started to saturate.

3.2.8 Electron transfer from $MV^{+\bullet}$ to Pt nanoparticle cocatalyst

To study the electron transfer from $MV^{+\bullet}$ to the Pt NP cocatalyst, experiments were performed in a 1 cm FUV cuvette with a stir bar and sealed with a rubber septum. Each sample contained $MV^{+\bullet}$ in the desired pH MES/HEPES/TAPS buffer. 50 µL of PVA-capped Pt NPs were injected after a baseline reading of $MV^{+\bullet}$ signal at 604 nm was obtained. While stirring, the decay of the absorption signal at 604 nm was monitored using kinetics mode on an Agilent Cary 60 UV-visible spectrophotometer and fit to an exponential decay function. This experiment was carried out at all four pH values (3, 6, 7, and 8), however, to make the $MV^{+\bullet}$ starting solution, different reducing agents were necessary. For pH 6, 7, and 8, dithionite was used as the reducing agent to reduce MV^{2+} to $MV^{+\bullet}$. However, dithionite's low solubility at pH 3 rendered it unable to reduce MV^{2+} at pH 3, instead, $NaBH_4$ was employed as the reducing agent at pH 3.

3.2.9 Pt nanoparticle cocatalyst H_2 production

H_2 production catalyzed by the Pt NPs was monitored directly from the samples used to study electron transfer from $MV^{+\bullet}$ to Pt NPs by measuring the H_2 produced after the latter experiment was complete. During the study of the electron transfer from $MV^{+\bullet}$ to the Pt NPs, once the Pt NPs were injected and the signal at 604 nm had decayed, the amount of H_2 in the headspace of the cuvette was measured using a gas chromatograph with thermal conductivity detector (GC-TCD). 200 µL of the sample vial's headspace was removed using a gas-tight glass syringe and injected into the GC-TCD. QYs of H_2 production were calculated as a quantitative measure of the Pt NP H_2 production efficiency.

3.2.10 Hole scavenging

It was necessary to study the hole scavenging step in multiple ways. Firstly, a wide variety of hole scavengers were tested for H_2 production performance in order to select the most efficient hole scavenger for the system (Figure 3.3). These H_2 production experiments were carried out in standard opening 2 mL crimp-top vials (Fisher Scientific) with a stir bar and 7.1 mm ID rubber septa (Cole-Parmer). Each sample contained 1 mg of $(Ga_{1-x}Zn_x)(N_{1-x}O_x)$ powder, 73.3 µM Pt NPs, 5 mM MV^{2+}, excess of the hole scavenger (>100 mM), in pH 3 MES/HEPES/TAPS buffer with a total sample volume of 300 µL. The exact concentration of hole scavenger in each sample varied based on the solubility limit of each hole scavenger in water. In each case, several concentrations near and at the solubility limit were tested. Once DTE was chosen as the preferred hole scavenger, the experiment studying reduction of MV^{2+} by $(Ga_{1-x}Zn_x)(N_{1-x}O_x)$, with the 2 mm cuvette with the Kontes valve top, was performed with and without DTE (200 mM) in the sample, as described above, and the MV^{2+} reduction rates were compared.

3.3 Results and Discussion

3.3.1 Pt Nanoparticle Characterization

Pt NPs were chosen as a cocatalyst for this H_2 production system because Pt is a well-known H_2 production catalyst.[5, 48-49] The Pt NPs used as solution phase cocatalysts in this study are 3.5 ± 0.6 nm in diameter. Figure 3.1 shows the UV-visible absorption spectrum and a TEM image for the Pt NPs.

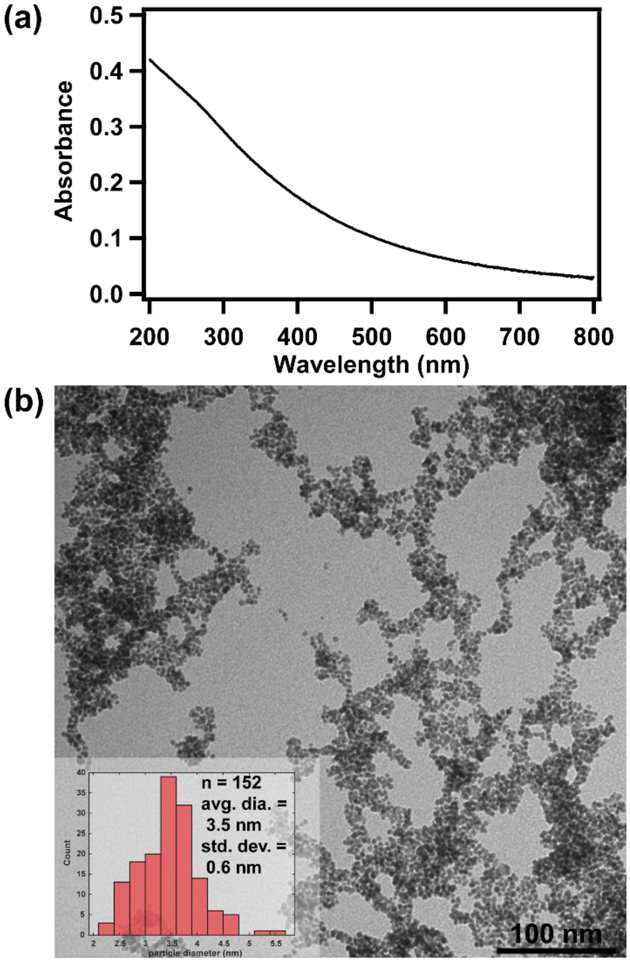

Figure 3.1: (a) UV-visible absorbance spectrum, (b) TEM image of Pt NP cocatalyst with diameters of 3.5 ± 0.6 nm, n=152.

The sample in Figure 3.1(a) has a [Pt] of ~0.14 mM, which is about double the [Pt] in a typical reaction solution. At 447 nm, the wavelength at which the reaction solutions are illuminated, the absorbance of the Pt NPs in a reaction solution is about half of what is seen in Figure 3.1(a), about 0.06. This absorbance is suitably low and therefore any absorbance screening of the $(Ga_{1-x}Zn_x)(N_{1-x}O_x)$ NCs by the Pt NPs should be negligible.

3.3.2 $(Ga_{1-x}Zn_x)(N_{1-x}O_x)$ Characterization

Prior work from the Domen group and others found that low x-values of $(Ga_{1-x}Zn_x)(N_{1-x}O_x)$ are more efficient light absorbers for photochemical systems; therefore, we use a low x-value to attempt to maximize the system's efficiency.[7-9, 13-14, 17-18, 35, 40, 50-52] The sample used in this study is $(Ga_{1-x}Zn_x)(N_{1-x}O_x)$ NCs with x=0.17 and ~5 nm in diameter. Figure 3.2 shows the XRD pattern, high-resolution TEM image, and Kubelka-Munk plot for the sample being studied. The Kubelka-Munk plot is generated by taking diffuse reflectance data to obtain a reflectance spectrum which is converted using the Kubelka-Munk equation $(F(R_\infty)=(1-R_\infty)^2/2R_\infty$, where $R_\infty=R_{sample}/R_{reference})$ into the equivalent of an absorbance spectrum. ICP-MS was performed to determine the x-value, or Zn content, of the sample, which is x=0.17. The Kubelka-Munk plot shows that the $(Ga_{1-x}Zn_{x-})(N_{1-x}O_x)$ NCs absorb visible and UV light. The high-resolution TEM image shows that particles are approximately 5 nm in diameter and single-crystalline.

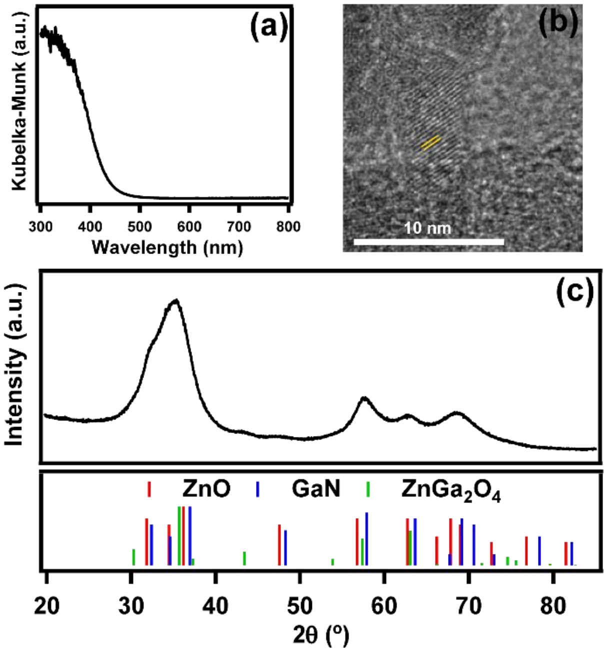

Figure 3.2: (a) Kubelka-Munk plot, (b) high-resolution TEM image, and (c) powder XRD pattern of (Ga$_{1-x}$Zn$_x$)(N$_{1-x}$O$_x$) NCs.

The XRD pattern shows broad peaks that match the reference patterns of GaN and ZnO wurtzite particles as well as some of the precursor $ZnGa_2O_4$ spinel particles. While some of the wurtzite and spinel reference lines overlap, there are a few distinct features that suggest the particles have a wurtzite crystal structure, for example: the shoulder around 32°, which is most likely part of the wurtzite triplet that also includes the peaks around 34° and 36°, all of which have been broadened into one large peak. Also of note are the features around 47° and 68°, which are distinct to the wurtzite references. Because the high-resolution TEM indicates that the particles are single crystalline, most of the peak broadening in the XRD pattern is attributed to the small particle size.[37-38, 46]

3.3.3 H_2 Production

The H_2 production system studied in this paper uses (Ga$_{1-x}$Zn$_x$)(N$_{1-x}$O$_x$) NCs as the light absorber, MV^{2+} as the electron relay, Pt NPs as the H_2 production cocatalyst, and DTE as the hole scavenger. Although $(Ga_{1-x}Zn_x)(N_{1-x}O_x)$ is known to be a strong light absorber, having a large molar absorptivity (ε),[39] in this H_2 production system it has a poor external quantum yield (EQY) of H_2 production. Possible explanations for this poor performance include the excited carriers being trapped in defects and vacancies before being transferred, unfavorable band potential alignments for driving electron transfer, or inefficient charge transfer from $(Ga_{1-x}Zn_x)(N_{1-x}O_x)$ to the catalyst. To investigate this, we developed the system in Scheme 3.1 to separate the charge transfer and catalysis steps in order to determine how each contributes to the overall H_2 production efficiency. The design of this system allows each major step or pathway involved in the H_2 production cycle, from charge transfer to catalysis, to be studied independently, allowing us to investigate how much and in what ways each step contributes to the overall chemistry of the system.

Scheme 3.1: Four-step photochemical H_2 production system.

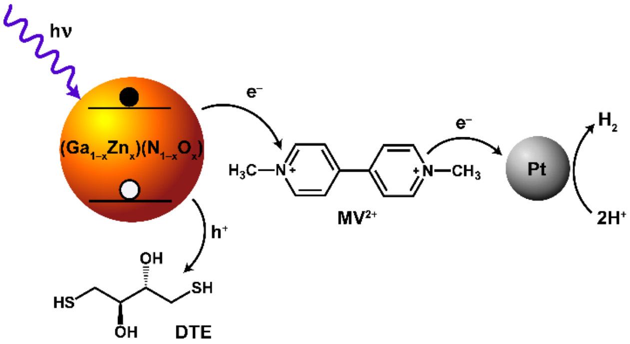

The overall system utilizes $(Ga_{1-x}Zn_x)(N_{1-x}O_x)$ NCs (x=0.17, 5 nm diameter) as the light absorber. MV^{2+} was chosen as the electron mediator because it is a well-known electron acceptor and has previously been used to efficiently shuttle electrons from light absorbers to cocatalysts through solution.[53-60] Preliminary tests were positive and confirmed that electrons could be transferred from the $(Ga_{1-x}Zn_x)(N_{1-x}O_x)$ NCs to the MV^{2+} molecules (the solution turned blue under illumination). Another important role that needed to be filled was that of the hole scavenger. Screening tests were done (Figure 3.3) to find the optimal hole scavenger for the system and DTE was chosen as the hole scavenger for the overall system. Lastly, since most of the steps in the system are pH dependent, a buffer cocktail with a wide pH range was required. In order to achieve a large pH buffering range and maintain continuity between samples, a buffer cocktail containing MES, HEPES, and TAPS was created. MES, HEPES, and TAPS are all sulfonic acid buffers and combining them allowed for maximum buffering capacities at pH 3, 6, 7, and 8 which provided a large pH range for studying the overall system.

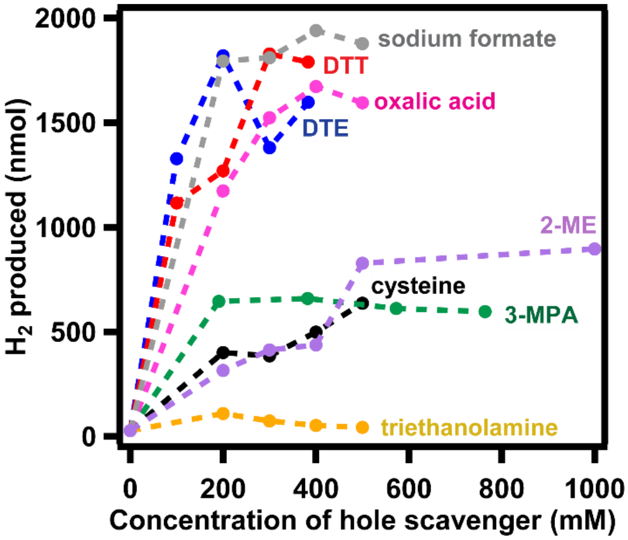

Figure 3.3: Amount of H_2 produced vs. concentration of hole scavenger for 8 different hole scavengers. Sample conditions: 2 mL vial with stir bar, 7.1 mm ID rubber septa, 1 mg of $(Ga_{1-x}Zn_x)(N_{1-x}O_x)$ powder, 73.3 µM Pt NPs, 5 mM MV^{2+}, excess of hole scavenger (>100 mM), in pH 3 MES/HEPES/TAPS buffer, total sample volume of 300 µL.

The hole scavengers tested in Figure 3.3 were ruled out for several reasons. Firstly, because some of them showed poor H_2 production performance (triethanolamine) or mediocre H_2 production performance (3-MPA, cysteine, 2-ME). Secondly, some were ruled out because they produce H_2 in a side reaction (sodium formate) and were therefore unreliable for the experiment.

Lastly, some were ruled out due to solubility issues (oxalate and oxalic acid). In the end, DTE and DTT, which are epimers of each other, were left as the possible candidate. On the average, both DTE and DTT performed similarly as hole scavengers so the choice came to convenience and availability in the lab, and therefore DTE was chosen as the hole scavenger for the system.

When the overall system is illuminated with a 447 nm diode laser at ~142 mW, it produces H_2. As shown in Figure 3.4, the H_2 production is pH dependent, with the largest amount of H_2 produced at pH 3; however, even that maximum amount of H_2 produced by the system is very small compared to other H_2 production systems utilizing $(Ga_{1-x}Zn_x)(N_{1-x}O_x)$. There have been QYs reported for other $(Ga_{1-x}Zn_x)(N_{1-x}O_x)$ H_2 production systems as high as 17.3%[40] for hollow sphere x=0.18 $(Ga_{1-x}Zn_x)(N_{1-x}O_x)$ particles decorated with Rh_2O_3-Cr_2O_3 as a cocatalyst and 5.9%[14] for x=0.18 $(Ga_{1-x}Zn_x)(N_{1-x}O_x)$ particles with $Rh_{2-y}Cr_yO_3$ as a cocatalyst. In contrast, the approximate EQY of H_2 production for this system at pH 3 is 0.084% ± 0.005%, two to three orders of magnitude smaller than other reported values for $(Ga_{1-x}Zn_x)(N_{1-x}O_x)$. The EQY for this experiment is calculated by the following equation: $EQY = 2\left(\frac{mol\ H_2}{mol\ incident\ photons}\right) \times 100\%$, which gives a lower limit for the EQY because the sample is a powder slurry and not optically clear, causing some of the photons to be lost due to scattering off of the powder particles. We aim to understand the contributions of the material properties and the catalysis to the low EQY of H_2 production observed.

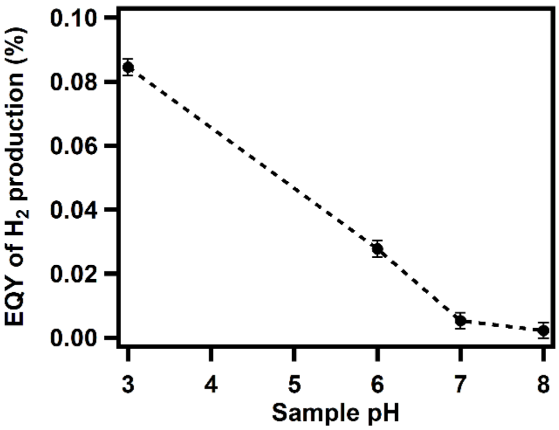

Figure 3.4: pH dependence of overall H_2 production system. Sample contained 1 mg of $(Ga_{1-x}Zn_x)(N_{1-x}O_x)$ powder, 5 mM MV^{2+}, 66 µM Pt NPs, 0.2 M DTE, in either pH 3, 6, 7, or 8 100 mM MES/HEPES/TAPS buffer.

3.3.4 Light absorption by $(Ga_{1-x}Zn_x)(N_{1-x}O_x)$ and electron transfer to MV^{2+} with and without DTE:

In order to investigate how each step in the H_2 production system performed when isolated from the other steps, electron transfer from photoexcited $(Ga_{1-x}Zn_x)(N_{1-x}O_x)$ to MV^{2+} was studied with and without DTE. A UV-vis kinetics experiment examining the reduction of MV^{2+} by $(Ga_{1-x}Zn_x)(N_{1-x}O_x)$ with and without DTE is shown in Figure 3.5 (a-e). As the sample is illuminated, UV-vis spectra are taken to investigate the $MV^{+\bullet}$ feature at 604 nm that grows in over time (Figure 3.5(a)). MV^{2+} is colorless, while $MV^{+\bullet}$ is blue/purple and absorbs strongly at 604 nm, which is what makes monitoring its formation through UV-vis measurements possible. As the $(Ga_{1-x}Zn_x)(N_{1-x}O_x)$ particles absorb the 447 nm laser light, excited electrons are transferred from the $(Ga_{1-x}Zn_x)(N_{1-x}O_x)$ particles to the MV^{2+} molecules, reducing them to $MV^{+\bullet}$. Photoexcited holes are scavenged from the $(Ga_{1-x}Zn_x)(N_{1-x}O_x)$ particles by a sacrificial hole scavenger, DTE. This experiment was performed with samples of pH of 3, 6, 7, and 8 with DTE (Figure 3.5(b-e), blue traces) and without DTE (Figure 3.5(b-e), black traces). Once the UV-vis data was analyzed and the $[MV^{+\bullet}]$ was calculated using Beer's Law (ε_{604} = 13,600 $M^{-1}cm^{-1}$),[47] the plots in Figure 3.5(b-

e) were generated. Figure 3.5(b-e) show the entirety of each data set being fit to an exponential rise; however, the initial rate of MV^{2+} reduction was calculated by fitting only the early time points and an EQY of MV^{2+} reduction was calculated by taking the initial rate of MV^{2+} reduction in moles $MV^{+\bullet}$/s divided by moles of incident photons/s and multiplying by 100%. The initial rates and EQY of MV^{2+} reduction are shown in Figure 3.5(f), which compares the initial rate and EQY of MV^{2+} reduction with and without DTE for the four different pH samples.

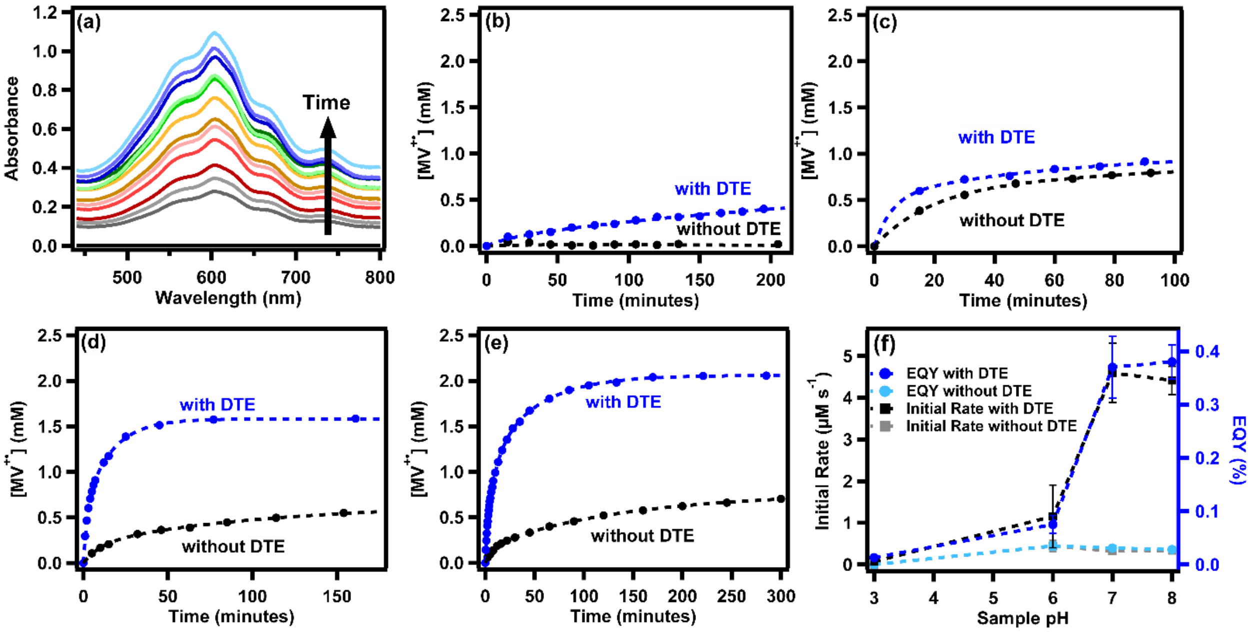

Figure 3.5: (a) UV-vis spectra taken over time (arrow indicates increasing illumination time) of the pH 3 sample. (b-e) Traces illustrating the production of $MV^{+\bullet}$ over time with (blue) and without (black) DTE at pH 3 (b), 6 (c), 7 (d), and 8 (e). (f) Plot of initial rate of $MV^{+\bullet}$ production and EQY at pH 3, 6, 7, and 8 with and without DTE.

The initial rates and the magnitude of final [$MV^{+\bullet}$] from the exponential growth curves in Figure 3.5(b-e) also indicate that the reduction of MV^{2+} to $MV^{+\bullet}$ by $(Ga_{1-x}Zn_x)(N_{1-x}O_x)$ particles gets faster and more extensive as the pH increases. The reduction of MV^{2+} is the slowest at pH 3, with the smallest magnitude of final [$MV^{+\bullet}$], and the fastest at pH 8, with the largest magnitude of final [$MV^{+\bullet}$]. The EQYs of MV^{2+} reduction given in Figure 3.5(f) show that the EQY of MV^{2+}

reduction is the smallest for pH 3 and largest for pH 8. The changing values of EQYs of MV^{2+} reduction, initial rates, and final [$MV^{+\bullet}$] support the idea that the $(Ga_{1-x}Zn_x)(N_{1-x}O_x)$ conduction band (CB) is shifting with pH while the redox potential of the $MV^{2+}/MV^{+\bullet}$ stays constant. Shifting of the $(Ga_{1-x}Zn_x)(N_{1-x}O_x)$ CB would change the driving force for the electron transfer from $(Ga_{1-x}Zn_x)(N_{1-x}O_x)$ to MV^{2+}. The CB and valence band (VB) of metal oxide particles are known to shift with pH due to a change in surface charge and proton intercalation.[61-64]

Knowing that the EQY of MV^{2+} reduction is very low for all of the samples (about 0.013% at pH 3) supports the hypothesis that the $(Ga_{1-x}Zn_x)(N_{1-x}O_x)$ CB could be positioned poorly for electron transfer in reference to the $MV^{2+}/MV^{+\bullet}$ redox potential. Our group has done photoelectrochemical studies to determine the flat band potential via open circuit potential and photocurrent onset measurements. The CB energy determined from the open circuit potential experiments is –0.15 V vs. NHE and the CB energy determined from the photocurrent onset measurements is –0.39 V vs. NHE for x=0.23. Other CB values from the literature include –0.78 V vs. NHE (x=0.42, bulk particles) from photocurrent onset data from Hashiguchi et al.,[65] –0.97 eV vs. NHE (x=0.31, CVD nanowires) and –1.01 eV vs. NHE (x=0.09, CVD nanowires) from subtracting the VB value determined by valence-band X-ray photoelectron spectroscopy from the bandgap value from Ren et al.,[66] and about –0.7 V vs. NHE (x=0.18, hollow spheres) from UV photoelectron spectroscopy data from Li et al.[40] The difference in reported CB values from the literature and those determined by our group can be due to various things including the synthesis method, x-value, and the data collection method, none of which are the same. Both of our experiments suggest that the $(Ga_{1-x}Zn_x)(N_{1-x}O_x)$ CB in our material is more positive than the $MV^{2+}/MV^{+\bullet}$ redox potential. If that is the case, it is possible that electrons would need to build up in the CB to overcome the small barrier to the $MV^{2+}/MV^{+\bullet}$ redox potential and there would be little driving force for electron transfer before enough electrons accumulate. This could cause the efficiency of MV^{2+} reduction by $(Ga_{1-x}Zn_x)(N_{1-x}O_x)$ to be poor, which could significantly limit the overall H_2 production efficiency.

Another factor that contributes to the efficiency of MV^{2+} reduction is the hole scavenging via sacrificial hole scavenger DTE. Figure 3.5 shows a trend in the effectiveness of DTE as a hole scavenger. Looking at the black traces in Figure 3.5(c-e), it’s clear that each one saturates at a similar maximum $[MV^{+\bullet}]$. This confirms the necessity of using a hole scavenger like DTE, because without DTE, the hole scavenging is limiting the MV^{2+} reduction. Comparing the blue traces in Figure 3.5(b-e) to the black traces, there is a dramatic increase in MV^{2+} reduction due to the addition of DTE. There is also a pH dependent increase in the maximum $[MV^{+\bullet}]$ saturation point with DTE. As the pH increases, the reduction of MV^{2+} to $MV^{+\bullet}$ saturates at a larger $[MV^{+\bullet}]$ indicating that DTE could be scavenging holes more efficiently at higher pH. This is not unexpected since DTE has two thiol groups responsible for the hole scavenging and as the pH increases closer to the pK_a of the thiol groups (about pH 9 and 10), the proton on the thiols is more likely to be unbound, improving the hole scavenging ability of DTE.

Hole scavenging would be particularly important in the instance that it is necessary to build up electrons in the $(Ga_{1-x}Zn_x)(N_{1-x}O_x)$ CB, because the hole scavenging would need to be fast and efficient in order to achieve a build-up of electrons in the CB. Plots (c)-(e) in Figure 3.5 all show a faster initial rate of MV^{2+} reduction when DTE is present (blue) as opposed to when DTE is not present (black), with the pH 3 sample (Figure 3.5(b)) unable to reduce a measurable amount of MV^{2+} without DTE. The higher initial rates of MV^{2+} reduction indicate that DTE does participate in the reaction. Due to energy level alignment, we propose that DTE is scavenging holes from the $(Ga_{1-x}Zn_x)(N_{1-x}O_x)$ NCs, which are reducing the MV^{2+}. The slower initial MV^{2+} reduction rate in the sample without DTE suggests that a hole scavenger is necessary to reduce the build-up of holes in the $(Ga_{1-x}Zn_x)(N_{1-x}O_x)$ VB in order for the NCs to continue to be excited. Alternatively, the slower initial rate without DTE might indicate that electrons must build up in the CB in order to overcome the possible barrier to the $MV^{2+}/MV^{+\bullet}$ redox potential. By using enough DTE so that the hole scavenger is in excess, the limiting effects of hole scavenging can be minimized. However, without comparing this rate to the rates of the other steps in the system, it is unclear if slow MV^{2+} reduction is the only source of low EQY of H_2 production in this system.

3.3.5 Electron transfer from $MV^{+\bullet}$ to Pt and subsequent H_2 production:

Electron transfer from $MV^{+\bullet}$ to the Pt cocatalyst is a key step in H_2 production, as the H^+ reduction reaction occurs at the Pt cocatalyst (Figure 3.6(a)). The efficiency of electron transfer from $MV^{+\bullet}$ to Pt was studied by chemically reducing MV^{2+}, injecting Pt NPs, and measuring the decay of the $MV^{+\bullet}$ feature at 604 nm using steady-state UV-vis kinetics. Figure 3.6(b) shows the $[MV^{+\bullet}]$ decaying over time for three different samples. The samples are at pH 6, 7, and 8. Sodium dithionite was used to reduce MV^{2+} to $MV^{+\bullet}$ for all samples except pH 3, as dithionite is unable to reduce MV^{2+} at this pH. The experiment started with the sample cuvette in the UV-vis spectrophotometer, which was in kinetics mode. The sample was being stirred and baseline absorbance signal at 604 nm was gathered for about 3 minutes. Each sample was injected with 50 μL of Pt NPs (20 μM) after baseline signal was gathered. Once the Pt NPs were injected, the absorbance signal at 604 nm decayed and Beer's Law was implemented to calculate $[MV^{+\bullet}]$. The initial decay rate was fastest for the sample at pH 6, slowest for the sample at pH 8, and the pH 7 sample fell in between. The values for the rate constants also follow this trend.

Directly following the electron transfer from $MV^{+\bullet}$ to the Pt NP, Pt catalyzes H^+ reduction to H_2. The data in Figure 3.6(d) was gathered directly after the $MV^{+\bullet}$ to Pt electron transfer experiments were completed. After Pt NP injection and decay of the signal at 604 nm, aliquots of the headspace of the samples examined in Figure 3.6(b) and their controls were injected into a GC-TCD to measure the amount of H_2 produced. Total moles of $MV^{+\bullet}$ consumed, calculated by taking the starting moles of $MV^{+\bullet}$ - ending moles of $MV^{+\bullet}$, was used as the number of moles of available electrons for the calculation: $QY = \left(2\left(\frac{mol\ H_2\ produced}{mol\ available\ electrons}\right)\right) \times 100\%$. The results of the QY calculation are shown in Figure 3.6(d). The control samples with dithionite and buffer produced no H_2.

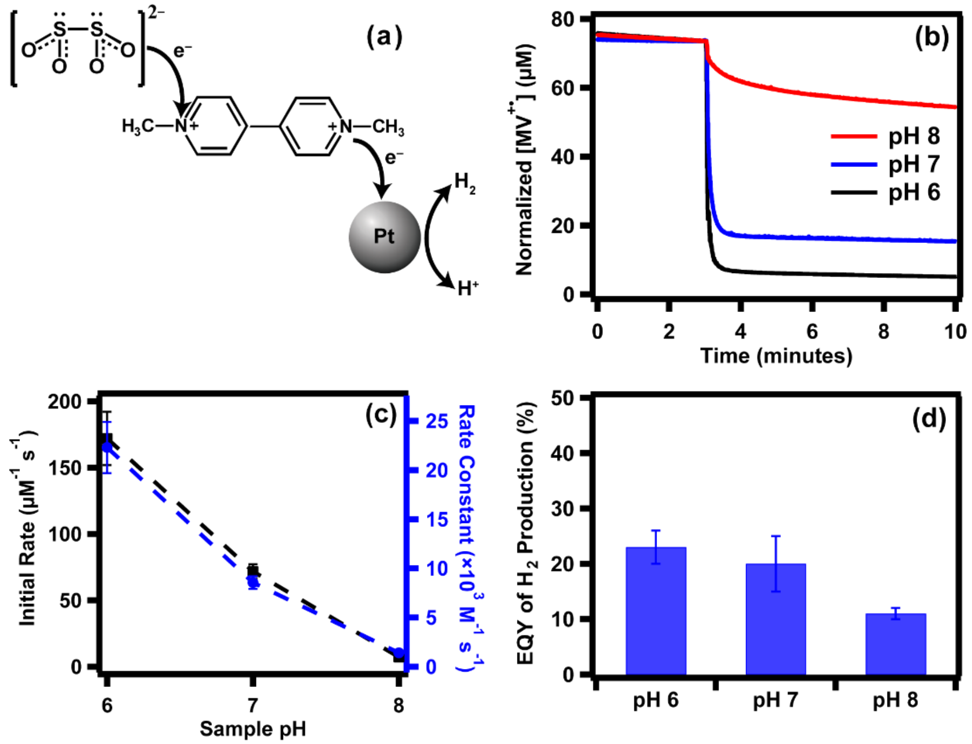

Figure 3.6: (a) Scheme showing electron transfer from dithionite to MV^{2+} to Pt, which generates H_2. (b) Decay of $[MV^{+\bullet}]$ over time at pH 6, 7, and 8 after injection of Pt NPs. Data has been normalized and adjusted so traces start at same time point. (c) Initial rate of $MV^{+\bullet}$ decay in M/s on the left axis (black) and rate constant of $MV^{+\bullet}$ decay on the right axis (blue). (d) Plot of QY of H_2 production for Pt NPs at pH 6, 7, and 8.

As the pH increases, the initial rate of electron transfer from $MV^{+\bullet}$ to the Pt NPs is slower and the total amount of $MV^{+\bullet}$ that decays decreases. The trend of QY data in Figure 3.6(d) follows the trend of overall amount of oxidized $MV^{+\bullet}$ shown in Figure 3.6(b) and the trends of initial rates of electron transfer and rate constants seen in Figure 3.6(c). As the pH increases, the rate of electron transfer, as well as the QY of H_2 production, decreases. Miller et al. has also seen this same trend of the rate of H_2 production decreasing with increasing pH in a similar system with MV and Pt but using a different light absorber and hole scavenger.[67]

One possible explanation for the decrease in the rate of electron transfer and the QY of H_2 production with increasing pH is that the driving force for electron transfer between $MV^{+\bullet}$ and Pt NPs may be decreasing with increasing pH. While the $MV^{2+}/MV^{+\bullet}$ redox potential remains constant with pH, the Pt NP Fermi level can shift with pH, decreasing the driving force for electron transfer. In the Perspective by Scanlon et al., the behavior of the Fermi level in metallic NPs in solution is thoroughly explained.[68] They explain that the Fermi level of metallic NPs will equilibrate to the potential of the most prominent redox couple in solution. In this case that means the Fermi level of the Pt NPs will equilibrate with the potential of the $MV^{2+}/MV^{+\bullet}$ redox couple (-0.45 V vs. NHE). Next, Scanlon et al. explains that as negative charges build up on the metallic NP surface, the Fermi level shifts to more negative potentials and as positive charges build up on the metallic NP surface, the Fermi level shifts to more positive potentials. In this system, if the Fermi level of the Pt NPs equilibrates with the $MV^{2+}/MV^{+\bullet}$ redox couple, then as the pH increases, more OH^{-} ions will adsorb to the Pt NP surface, causing the Fermi level to shift to more negative potentials and reducing the driving force for electron transfer from the $MV^{+\bullet}$ radical to the Pt NP. This would also account for the decrease in overall oxidized $MV^{+\bullet}$, as a smaller difference between the Pt NP Fermi level and the $MV^{2+}/MV^{+\bullet}$ redox potential could cause fewer electrons to be transferred from $MV^{+\bullet}$ to Pt. Conversely, as the pH decreases, H^{+} ions will adsorb to the Pt NP surface and cause a positive charge to build up, which would shift the Fermi level to more positive potentials (further away from the $MV^{2+}/MV^{+\bullet}$ redox couple), increasing the driving force for electron transfer from $MV^{+\bullet}$ radical to Pt NPs. Since the reduction potential for H^+ reduction to H_2 also decreases with increasing pH, this could contribute to the decrease in catalytic efficiency. As the $[H^+]$ is two orders of magnitude higher at pH 6 than at pH 8, the QY of H_2 production should also be higher at the more acidic pH. We observe the highest QY of H_2 production (23%) at pH 6, which fits with our observation of most efficient electron transfer at pH 6. Although background H_2 production by the chemical reducing agent makes the data collected at pH 3 unsuitable for quantitative analysis, it does show the same trend in QY of H_2 production as the dithionite data, suggesting that pH 3 would follow the same trend and have the highest QY of H_2 production. However, compared to other cocatalysts, a QY of 23% is somewhat low, which could contribute to lower efficiencies in this and other systems as noted by Zhu and coworkers,[57] indicating that QYs higher than 23% may be possible with more efficient cocatalysts. However, this change in efficiency due to pH is not as strong as the trend in efficiency with pH that is seen in the experiments studying electron transfer from $(Ga_{1-x}Zn_x)(N_{1-x}O_x)$ to MV^{2+}, so overall, the QY of 23% for the Pt NPs is much more efficient than the 0.013% EQY of MV^{2+} reduction.

Overall, the reduction of MV^{2+} by $(Ga_{1-x}Zn_x)(N_{1-x}O_x)$ NCs is very inefficient and slow (~0.013% at pH 3), the electron transfer from $MV^{+\bullet}$ to the Pt cocatalyst is fast (rate constant of $2.2\times10^4\ M^{-1}s^{-1}$ at pH 6), the QY of H_2 generation from the Pt cocatalyst is 23% at pH 6, and the hole scavenging by DTE is as optimized as possible. All of these individual efficiencies will contribute to the overall H_2 production efficiency of the complete system. While each individual efficiency is important, it appears that the very low efficiency of MV^{2+} reduction by $(Ga_{1-x}Zn_x)(N_{1-x}O_x)$ NCs affects the overall system efficiency the most. The <100% QY of H_2 generation for the Pt cocatalyst and the hole scavenging by DTE can also incrementally lower the overall system efficiency, while it seems like the electron transfer from $MV^{+\bullet}$ to Pt should affect the overall system efficiency the least at low pH values. However, as the pH increases, the rate and magnitude of electron transfer from $MV^{+\bullet}$ to Pt will start to limit the overall system efficiency more, as exemplified by the pH 8 data, which shows a very small magnitude of overall $MV^{+\bullet}$ oxidation, meaning a small magnitude of electron transfer to Pt.

Comparing the rate of $MV^{+\bullet}$ generation and consumption at pH 6 vs. pH 8, there is a distinct difference. At pH 6, the rate of $MV^{+\bullet}$ consumption is two orders of magnitude faster than the rate of $MV^{+\bullet}$ generation. At pH 8, the rate of $MV^{+\bullet}$ consumption and generation are the same order of magnitude. This means that at pH 6 (or pH 3 if we extrapolate the data), $MV^{+\bullet}$ is being consumed much faster than it is being generated and at pH 8 $MV^{+\bullet}$ is being consumed almost as fast as it is being generated. Therefore, at lower pH, the overall efficiency is clearly limited by $MV^{+\bullet}$ generation, while at higher pH the electron transfer from $MV^{+\bullet}$ to Pt is likely limiting the overall efficiency just as much as MV^{+} generation. Additionally, the catalytic efficiency of Pt for H^{+} reduction also decreases as pH increases, meaning Pt is also a less effective H_2 production catalyst at pH 8, on top of the electron transfer from $MV^{+\bullet}$ to Pt being slower. In summary, at lower pH, $MV^{+\bullet}$ generation is the overwhelming cause of overall H_2 production inefficiency, while at higher pH, $MV^{+\bullet}$ generation and consumption rates are the same order of magnitude while the catalytic efficiency of Pt for H^{+} reduction is 10% lower than at more acidic pH, causing all three factors to be limiting the overall H_2 production efficiency, not just one factor like at lower pH.

Since the initial rate and EQY of MV^{2+} reduction are low at pH 3, it is possible that the $(Ga_{1-x}Zn_x)(N_{1-x}O_x)$ CB is very close to or more positive than the redox potential of $MV^{2+}/MV^{+\bullet}$ and therefore may require some sort of initial build-up of electrons in the CB before the electrons can transfer to the MV^{2+} molecule. Requiring a build-up of electrons before MV^{2+} reduction can occur would help explain the low values of EQY of MV^{2+} reduction that are seen. This hypothesis is supported by our group's photocurrent onset measurements that estimate the CB energy at –0.39 V vs. NHE and open circuit potential measurements that estimate a CB energy of –0.15 V vs. NHE for x=0.23. Our CB estimate values are less negative than other CB estimates in the literature. Hashiguchi et al.[65] estimate the CB of x=0.42 bulk particles as –0.78 V vs. NHE from photocurrent onset data. Ren et al.[66] estimate the CB of x=0.31 CVD nanowires as –0.97 eV vs. NHE and –1.01 eV vs. NHE for x=0.09 CVD nanowires by subtracting the VB value determined by valence-band X-ray photoelectron spectroscopy from the bandgap value. Lastly, Li et al.[40] estimate the CB of x=0.18 hollow spheres as –0.7 V vs. NHE from UV photoelectron spectroscopy data. The difference between our group's CB estimates and the other estimates reported in the literature could be due to a variety of things including the synthesis method, x-value, and data collection method, all of which are different. As the pH increases, the initial rate and EQY of MV^{2+} reduction also increase, indicating that the CB of the $(Ga_{1-x}Zn_x)(N_{1-x}O_x)$ could be moving to more negative potentials, possibly more negative than the $MV^{2+}/MV^{+\bullet}$ redox potential, increasing the driving force of electron transfer from $(Ga_{1-x}Zn_x)(N_{1-x}O_x)$ to MV^{2+}.

While electron transfer from $MV^{+\bullet}$ to Pt seems favorable at low pH values, the turnover and QY of H_2 generation of the Pt itself is still <100% efficient. This <100% efficient performance has been seen by others and it has been suggested the H_2 production systems can be improved by using a better cocatalyst than Pt.[57] In this particular system, while the Pt performance may contribute to lowering the overall efficiency, the main source of overall inefficiency still comes from the slow MV^{2+} reduction. Additionally, hole scavenging is a potential source of inefficiency, which we optimized by testing many types and concentrations of hole scavengers (Figure 3.3), however we acknowledge that the hole scavenging step could still be contributing to the overall inefficiency.

The EQY of H_2 production for this system at pH 3 is 0.084% ± 0.005%, which is two to three orders of magnitude smaller than other reported values in the literature for $(Ga_{1-x}Zn_x)(N_{1-x}O_x)$ H_2 production. Other QYs reported in the literature for $(Ga_{1-x}Zn_x)(N_{1-x}O_x)$ H_2 production systems include performances as high as 17.3%[40] for hollow sphere x=0.18 $(Ga_{1-x}Zn_x)(N_{1-x}O_x)$ particles modified with Rh_2O_3-Cr_2O_3 as a cocatalyst and 5.9%[14] for x=0.18 $(Ga_{1-x}Zn_x)(N_{1-x}O_x)$ particles with $Rh_{2-y}Cr_yO_3$ as a cocatalyst. Both of these systems have cocatalysts directly deposited on the $(Ga_{1-x}Zn_x)(N_{1-x}O_x)$ surface, which eliminates the electron transfer step from $(Ga_{1-x}Zn_x)(N_{1-x}O_x)$ to a redox mediator. This lack of an extra electron transfer step could be one key reason why these other $(Ga_{1-x}Zn_x)(N_{1-x}O_x)$ H_2 production systems have significantly higher performance compared to our system.

3.4 Conclusions

After studying the four-part H_2 production system containing $(Ga_{1-x}Zn_x)(N_{1-x}O_x)$ NCs as the light absorber, Pt NPs as the cocatalyst, DTE as the hole scavenger, and MV^{2+} as the redox mediator, we have found that it produces H_2 with a maximum EQY of 0.084% at pH 3. The most limiting step in the system is the electron transfer from the $(Ga_{1-x}Zn_x)(N_{1-x}O_x)$ NC to the MV^{2+} molecule. Hole scavenging by DTE is also an important factor in H_2 production efficiency; however, it is assumed that using an excess of DTE minimizes the limitations of hole scavenging. Electron transfer from the redox mediator, $MV^{+\bullet}$, to the Pt NP cocatalyst is one of the fastest steps in the system and does not appear to limit the system's efficiency at lower pH values. Lastly, the production of H_2 by the Pt NPs had QYs around 23%, which is much larger than the EQYs of

MV^{2+} reduction by $(Ga_{1-x}Zn_x)(N_{1-x}O_x)$ but is still relatively low overall. Therefore, the Pt NP performance is probably not limiting the system the most, with the QY being four orders of magnitude larger than EQY of MV^{2+} reduction by $(Ga_{1-x}Zn_x)(N_{1-x}O_x)$, but it does mean that Pt NPs may not be the most efficient cocatalyst to use in this type of system. While further optimization of the cocatalyst for this system may be possible, the low EQY of MV^{2+} reduction by $(Ga_{1-x}Zn_{x-})(N_{1-x}O_x)$ suggests that it is electron transfer from the light absorber that is limiting the overall system efficiency. We conclude that the CB potential of the $(Ga_{1-x}Zn_x)(N_{1-x}O_x)$ NC is too positive to provide a strong driving force for electron transfer to MV^{2+}. With a different redox mediator, much higher QYs for H_2 production with this system could be possible.

3.5 References

(1) Lewis, N. S.; Nocera, D. G., Powering the planet: Chemical challenges in solar energy utilization. *Proceedings of the National Academy of Sciences of the United States of America* **2006**, *103*, 15729-15735.

(2) Whittingham, M. S., Lithium Batteries and Cathode Materials. *Chemical Reviews* **2004**, *104*, 4271-4302.

(3) Kudo, A.; Miseki, Y., Heterogeneous Photocatalyst Materials for Water Splitting. *Chemical Society Reviews* **2009**, *38*, 253-278.

(4) Nozik, A. J.; Beard, M. C.; Luther, J. M.; Law, M.; Ellingson, R. J.; Johnson, J. C., Semiconductor Quantum Dots and Quantum Dot Arrays and Applications of Multiple Exciton Generation to Third-Generation Photovoltaic Solar Cells. *Chemical Reviews* **2010**, *110*, 6873-6890.

(5) Walter, M. G.; Warren, E. L.; McKone, J. R.; Boettcher, S. W.; Mi, Q. X.; Santori, E. A.; Lewis, N. S., Solar Water Splitting Cells. *Chemical Reviews* **2010**, *110*, 6446-6473.

(6) Regulacio, M. D.; Han, M.-Y., Multinary I-III-VI_2 and I_2-II-IV-VI_4 Semiconductor Nanostructures for Photocatalytic Applications. *Accounts of Chemical Research* **2016**, *49*, 511-519.

(7) Maeda, K.; Takata, T.; Hara, M.; Saito, N.; Inoue, Y.; Kobayashi, H.; Domen, K., GaN:ZnO Solid Solution as a Photocatalyst for Visible-Light-Driven Overall Water Splitting. *Journal of the American Chemical Society* **2005**, *127*, 8286-8287.

(8) Maeda, K.; Teramura, K.; Takata, T.; Hara, M.; Saito, N.; Toda, K.; Inoue, Y.; Kobayashi, H.; Domen, K., Overall Water Splitting on $(Ga_{1-x}Zn_x)(N_{1-x}O_x)$ Solid Solution Photocatalyst: Relationship between Physical Properties and Photocatalytic Activity. *Journal of Physical Chemistry B* **2005**, *109*, 20504-20510.

(9) Maeda, K.; Teramura, K.; Lu, D.; Takata, T.; Saito, N.; Inoue, Y.; Domen, K., Characterization of Rh−Cr Mixed-Oxide Nanoparticles Dispersed on $(Ga_{1-x}Zn_x)(N_{1-x}O_x)$ as a Cocatalyst for Visible-Light-Driven Overall Water Splitting. *Journal of Physical Chemistry B* **2006**, *110*, 13753-13758.

(10) Maeda, K.; Teramura, K.; Lu, D. L.; Takata, T.; Saito, N.; Inoue, Y.; Domen, K., Photocatalyst releasing hydrogen from water - Enhancing catalytic performance holds promise for hydrogen production by water splitting in sunlight. *Nature* **2006**, *440*, 295-295.

(11) Maeda, K.; Teramura, K.; Masuda, H.; Takata, T.; Saito, N.; Inoue, Y.; Domen, K., Efficient Overall Water Splitting under Visible-Light Irradiation on $(Ga_{1-x}Zn_x)(N_{1-x}O_x)$ Dispersed with Rh−Cr Mixed-Oxide Nanoparticles: Effect of Reaction Conditions on Photocatalytic Activity. *Journal of Physical Chemistry B* **2006**, *110*, 13107-13112.

(12) Maeda, K.; Domen, K., New Non-Oxide Photocatalysts Designed for Overall Water Splitting under Visible Light. *Journal of Physical Chemistry C* **2007**, *111*, 7851-7861.

(13) Maeda, K.; Hashiguchi, H.; Masuda, H.; Abe, R.; Domen, K., Photocatalytic Activity of $(Ga_{1-x}Zn_x)(N_{1-x}O_x)$ for Visible-Light-Driven H_2 and O_2 Evolution in the Presence of Sacrificial Reagents. *Journal of Physical Chemistry C* **2008**, *112*, 3447-3452.

(14) Maeda, K.; Teramura, K.; Domen, K., Effect of Post-Calcination on Photocatalytic Activity of $(Ga_{1-x}Zn_x)(N_{1-x}O_x)$ Solid Solution for Overall Water Splitting under Visible Light. *Journal of Catalysis* **2008**, *254*, 198-204.

(15) Hisatomi, T.; Maeda, K.; Lu, D.; Domen, K., The Effects of Starting Materials in the Synthesis of $(Ga_{1-x}Zn_x)(N_{1-x}O_x)$ Solid Solution on Its Photocatalytic Activity for Overall Water Splitting under Visible Light. *ChemSusChem* **2009**, *2*, 336-343.

(16) Hisatomi, T.; Maeda, K.; Takanabe, K.; Kubota, J.; Domen, K., Aspects of the Water Splitting Mechanism on $(Ga_{1-x}Zn_x)(N_{1-x}O_x)$ Photocatalyst Modified with $Rh_{2-y}Cr_yO_3$ Cocatalyst. *The Journal of Physical Chemistry C* **2009**, *113*, 21458-21466.

(17) Maeda, K.; Domen, K., Solid Solution of GaN and ZnO as a Stable Photocatalyst for Overall Water Splitting under Visible Light. *Chemistry of Materials* **2010**, *22*, 612-623.

(18) Ohno, T.; Bai, L.; Hisatomi, T.; Maeda, K.; Domen, K., Photocatalytic Water Splitting Using Modified GaN:ZnO Solid Solution under Visible Light: Long-Time Operation and Regeneration of Activity. *Journal of the American Chemical Society* **2012**, *134*, 8254-8259.

(19) Hirai, T.; Maeda, K.; Yoshida, M.; Kubota, J.; Ikeda, S.; Matsumura, M.; Domen, K., Origin of Visible Light Absorption in GaN-Rich $(Ga_{1-x}Zn_x)(N_{1-x}O_x)$ Photocatalysts. *Journal of Physical Chemistry C* **2007**, *111*, 18853-18855.

(20) Huda, M. N.; Yan, Y. F.; Wei, S. H.; Al-Jassim, M. M., Electronic structure of ZnO:GaN compounds: Asymmetric bandgap engineering. *Physical Review B* **2008**, *78*, 195204.

(21) Jensen, L. L.; Muckerman, J. T.; Newton, M. D., First-Principles Studies of the Structural and Electronic Properties of the $(Ga_{1-x}Zn_x)(N_{1-x}O_x)$ Solid Solution Photocatalyst. *Journal of Physical Chemistry C* **2008**, *112*, 3439-3446.

(22) Wei, W.; Dai, Y.; Yang, K. S.; Guo, M.; Huang, B. B., Origin of the visible light absorption of GaN-Rich $Ga_{1-x}Zn_xN_{1-x}O_x$ (x=0.125) solid solution. *Journal of Physical Chemistry C* **2008**, *112*, 15915-15919.

(23) Chen, H.; Wang, L.; Bai, J.; Hanson, J. C.; Warren, J. B.; Muckerman, J. T.; Fujita, E.; Rodriguez, J. A., *In Situ* XRD Studies of ZnO/GaN Mixtures at High Pressure and High Temperature: Synthesis of Zn-Rich $(Ga_{1-x}Zn_x)(N_{1-x}O_x)$ Photocatalysts. *Journal of Physical Chemistry C* **2010**, *114*, 1809-1814.

(24) Di Valentin, C., Electronic Structure of $(Ga_{1-x}Zn_x)N_{1-x}O_x$ Photocatalyst for Water Splitting by Hybrid Hartree-Fock Density Functional Theory Methods. *Journal of Physical Chemistry C* **2010**, *114*, 7054-7062.

(25) Wang, S. Z.; Wang, L. W., Atomic and Electronic Structures of GaN/ZnO Alloys. *Physical Review Letters* **2010**, *104*, 065501.

(26) Yoshida, M.; Hirai, T.; Maeda, K.; Saito, N.; Kubota, J.; Kobayashi, H.; Inoue, Y.; Domen, K., Photoluminescence Spectroscopic and Computational Investigation of the Origin of the Visible Light Response of $(Ga_{1-x}Zn_x)(N_{1-x}O_x)$ Photocatalyst for Overall Water Splitting. *The Journal of Physical Chemistry C* **2010**, *114*, 15510-15515.

(27) Lee, Y.-C.; Lin, T.-Y.; Wu, C.-W.; Teng, H.; Hu, C.-C.; Hu, S.-Y.; Yang, M.-D., Visible luminescence properties of $(Ga_{1-x}Zn_x)(N_{1-x}O_x)$ solid solution (x = 0.22). *Journal of Applied Physics* **2011**, *109*, 073506.

(28) Li, L.; Muckerman, J. T.; Hybertsen, M. S.; Allen, P. B., Phase Diagram, Structure, and Electronic Properties of $(Ga_{1-x}Zn_x)(N_{1-x}O_x)$ Solid Solutions from DFT-Based Simulations. *Physical Review B* **2011**, *83*, 134202.

(29) Yu, H.-G., An optimal density functional theory method for GaN and ZnO. *Chemical Physics Letters* **2011**, *512*, 231-236.

(30) Dou, M.; Persson, C., Band gap reduction and dielectric function of $Ga_{1-x}Zn_xN_{1-x}O_x$ and $In_{1-x}Zn_xN_{1-x}O_x$ alloys. *physica status solidi (a)* **2012**, *209*, 75-78.

(31) McDermott, E. J.; Kurmaev, E. Z.; Boyko, T. D.; Finkelstein, L. D.; Green, R. J.; Maeda, K.; Domen, K.; Moewes, A., Structural and Band Gap Investigation of GaN:ZnO Heterojunction

Solid Solution Photocatalyst Probed by Soft X-ray Spectroscopy. *Journal of Physical Chemistry C* **2012**, *116*, 7694-7700.

(32) Shockley, W.; Queisser, H. J., Detailed Balance Limit of Efficiency of p-n Junction Solar Cells. *Journal of Applied Physics* **1961**, *32*, 510-519.

(33) Han, W.-Q.; Liu, Z.; Yu, H.-G., Synthesis and Optical Properties of GaN/ZnO Solid Solution Nanocrystals. *Applied Physics Letters* **2010**, *96*, 183112.

(34) Wang, J.; Huang, B.; Wang, Z.; Wang, P.; Cheng, H.; Zheng, Z.; Qin, X.; Zhang, X.; Dai, Y.; Whangbo, M.-H., Facile Synthesis of Zn-rich $(GaN)_{1-x}(ZnO)_x$ Solid Solutions Using Layered Double Hydroxides as Precursors. *Journal of Materials Chemistry* **2011**, *21*, 4562-4567.

(35) Hahn, C.; Fardy, M. A.; Nguyen, C.; Natera-Comte, M.; Andrews, S. C.; Yang, P. D., Synthesis and Photocatalytic Properties of Single Crystalline $(Ga_{1-x}Zn_x)(N_{1-x}O_x)$ Nanotubes. *Israel Journal of Chemistry* **2012**, *52*, 1111-1117.

(36) Adeli, B.; Taghipour, F., A Review of Synthesis Techniques for Gallium-Zinc Oxynitride Solar-Activated Photocatalyst for Water Splitting. *ECS J. Solid State Sci. Technol.* **2013**, *2*, Q118-Q126.

(37) Lee, K.; Tienes, B. M.; Wilker, M. B.; Schnitzenbaumer, K. J.; Dukovic, G., $(Ga_{1-x}Zn_x)(N_{1-x}O_x)$ Nanocrystals: Visible Absorbers with Tunable Composition and Absorption Spectra. *Nano Letters* **2012**, *12*, 3268-3272.

(38) Tongying, P.; Lu, Y.-G.; Hall, L. M. G.; Lee, K.; Sulima, M.; Ciston, J.; Dukovic, G., Control of Elemental Distribution in the Nanoscale Solid-State Reaction That Produces $(Ga_{1-x}Zn_x)(N_{1-x}O_x)$ Nanocrystals. *ACS Nano* **2017**, *11*, 8401-8412.

(39) Chuang, C.-H.; Lu, Y.-G.; Lee, K.; Ciston, J.; Dukovic, G., Strong Visible Absorption and Broad Time Scale Excited-State Relaxation in $(Ga_{1-x}Zn_x)(N_{1-x}O_x)$ Nanocrystals. *Journal of the American Chemical Society* **2015**, *137*, 6452-6455.

(40) Li, Y.; Zhu, L.; Yang, Y.; Song, H.; Lou, Z.; Guo, Y.; Ye, Z., A Full Compositional Range for a $(Ga_{1-x}Zn_x)(N_{1-x}O_x)$ Nanostructure: High Efficiency for Overall Water Splitting and Optical Properties. *Small* **2015**, *11*, 871-876.

(41) Zhou, Y.; Chen, G.; Yu, Y.; Zhao, L.; Yu, Q.; He, Q., Effects of La-doping on charge separation behavior of ZnO:GaN for its enhanced photocatalytic performance. *Catalysis Science & Technology* **2016**, *6*, 1033-1041.

(42) Godin, R.; Hisatomi, T.; Domen, K.; Durrant, J. R., Understanding the visible-light photocatalytic activity of GaN:ZnO solid solution: the role of $Rh_{2-y}Cr_yO_3$ cocatalyst and charge carrier lifetimes over tens of seconds. *Chemical Science* **2018**, *9*, 7546-7555.

(43) Li, Z.; Zhang, F.; Han, J.; Zhu, J.; Li, M.; Zhang, B.; Fan, W.; Lu, J.; Li, C., Using Pd as a Cocatalyst on GaN–ZnO Solid Solution for Visible-Light-Driven Overall Water Splitting. *Catalysis Letters* **2018**, *148*, 933-939.

(44) Wang, Z.; Li, C.; Domen, K., Recent developments in heterogeneous photocatalysts for solar-driven overall water splitting. *Chemical Society Reviews* **2019**.

(45) Wu, G.-W.; He, S.-B.; Peng, H.-P.; Deng, H.-H.; Liu, A.-L.; Lin, X.-H.; Xia, X.-H.; Chen, W., Citrate-Capped Platinum Nanoparticle as a Smart Probe for Ultrasensitive Mercury Sensing. *Analytical Chemistry* **2014**, *86*, 10955-10960.

(46) Lee, K.; Lu, Y.-G.; Chuang, C.-H.; Ciston, J.; Dukovic, G., Synthesis and Characterization of $(Ga_{1-x}Zn_x)(N_{1-x}O_x)$ Nanocrystals with a Wide Range of Compositions. *Journal of Materials Chemistry A* **2016**, *4*, 2927-2935.

(47) Mayhew, S. G.; Abels, R.; Platenkamp, R., The production of dithionite and SO_2^- by chemical reaction of (bi)sulphite with methyl viologen semiquinone. *Biochemical and Biophysical Research Communications* **1977**, *77*, 1397-1403.

(48) Aharon-Shalom, E.; Heller, A., Efficient p - InP (Rh - H alloy) and p - InP (Re - H alloy) Hydrogen Evolving Photocathodes. *Journal of The Electrochemical Society* **1982**, *129*, 2865-2866.

(49) Conway, B. E.; Tilak, B. V., Interfacial processes involving electrocatalytic evolution and oxidation of H_2, and the role of chemisorbed H. *Electrochimica Acta* **2002**, *47*, 3571-3594.

(50) Maeda, K.; Teramura, K.; Saito, N.; Inoue, Y.; Domen, K., Improvement of Photocatalytic Activity of $(Ga_{1-x}Zn_x)(N_{1-x}O_x)$ Solid Solution for Overall Water Splitting by Co-loading Cr and Another Transition Metal. *Journal of Catalysis* **2006**, *243*, 303-308.

(51) Sun, X.; Maeda, K.; Le Faucheur, M.; Teramura, K.; Domen, K., Preparation of $(Ga_{1-x}Zn_x)(N_{1-x}O_x)$ Solid-Solution from $ZnGa_2O_4$ and ZnO as a Photo-Catalyst for Overall Water Splitting under Visible Light. *Appl Catal a-Gen* **2007**, *327*, 114-121.

(52) Yoshida, M.; Maeda, K.; Lu, D.; Kubota, J.; Domen, K., Lanthanoid Oxide Layers on Rhodium-Loaded $(Ga_{1-x}Zn_x)(N_{1-x}O_x)$ Photocatalyst as a Modifier for Overall Water Splitting under Visible-Light Irradiation. *Journal of Physical Chemistry C* **2013**, *117*, 14000-14006.

(53) Van Dijk, C.; Veeger, C., The Effects of pH and Redox Potential on the Hydrogen Production Activity of the Hydrogenase from Megasphaera elsdenii. *European Journal of Biochemistry* **1981**, *114*, 209-219.

(54) Li, Q.; Guo, B.; Yu, J.; Ran, J.; Zhang, B.; Yan, H.; Gong, J. R., Highly Efficient Visible-Light-Driven Photocatalytic Hydrogen Production of CdS-Cluster-Decorated Graphene Nanosheets. *Journal of the American Chemical Society* **2011**, *133*, 10878-10884.

(55) Zhang, J.; Yu, J.; Zhang, Y.; Li, Q.; Gong, J. R., Visible Light Photocatalytic H_2-Production Activity of CuS/ZnS Porous Nanosheets Based on Photoinduced Interfacial Charge Transfer. *Nano Letters* **2011**, *11*, 4774-4779.

(56) Zhang, J.; Yu, J.; Jaroniec, M.; Gong, J. R., Noble Metal-Free Reduced Graphene Oxide-$Zn_xCd_{1-x}S$ Nanocomposite with Enhanced Solar Photocatalytic H_2-Production Performance. *Nano Letters* **2012**, *12*, 4584-4589.

(57) Zhu, H.; Song, N.; Lv, H.; Hill, C. L.; Lian, T., Near Unity Quantum Yield of Light-Driven Redox Mediator Reduction and Efficient H_2 Generation Using Colloidal Nanorod Heterostructures. *Journal of the American Chemical Society* **2012**, *134*, 11701-11708.

(58) Li, Q.; Meng, H.; Zhou, P.; Zheng, Y.; Wang, J.; Yu, J.; Gong, J., $Zn_{1-x}Cd_xS$ Solid Solutions with Controlled Bandgap and Enhanced Visible-Light Photocatalytic H_2-Production Activity. *ACS Catalysis* **2013**, *3*, 882-889.

(59) Chica, B.; Wu, C.-H.; Liu, Y.; Adams, M. W. W.; Lian, T.; Dyer, R. B., Balancing electron transfer rate and driving force for efficient photocatalytic hydrogen production in CdSe/CdS nanorod–[NiFe] hydrogenase assemblies. *Energy & Environmental Science* **2017**, *10*, 2245-2255.

(60) Zhao, F.; Li, Q.; Han, K.; Lian, T., Mechanism of Efficient Viologen Radical Generation by Ultrafast Electron Transfer from CdS Quantum Dots. *The Journal of Physical Chemistry C* **2018**, *122*, 17136-17142.

(61) Lemon, B. I.; Liu, F.; Hupp, J. T., Electrochemical, spectral, and quartz crystal microgravimetric assessment of conduction band edge energies for nanocrystalline zirconium dioxide/solution interfaces. *Coordination Chemistry Reviews* **2004**, *248*, 1225-1230.

(62) Yan, S. G.; Lyon, L. A.; Lemon, B. I.; Preiskorn, J. S.; Hupp, J. T., Energy Conversion Chemistry: Mechanisms of Charge Transfer at Metal-Oxide Semiconductor/Solution Interfaces. *Journal of Chemical Education* **1997**, *74*, 657.

(63) Lyon, L. A.; Hupp, J. T., Energetics of the Nanocrystalline Titanium Dioxide/Aqueous Solution Interface: Approximate Conduction Band Edge Variations between H0 = −10 and H- = +26. *The Journal of Physical Chemistry B* **1999**, *103*, 4623-4628.

(64) She, C.; Anderson, N. A.; Guo, J.; Liu, F.; Goh, W.-H.; Chen, D.-T.; Mohler, D. L.; Tian, Z.-Q.; Hupp, J. T.; Lian, T., pH-Dependent Electron Transfer from Re-bipyridyl Complexes to Metal Oxide Nanocrystalline Thin Films. *The Journal of Physical Chemistry B* **2005**, *109*, 19345-19355.

(65) Hashiguchi, H.; Maeda, K.; Abe, R.; Ishikawa, A.; Kubota, J.; Domen, K., Photoresponse of GaN:ZnO Electrode on FTO under Visible Light Irradiation. *Bulletin of the Chemical Society of Japan* **2009**, *82*, 401-407.

(66) Ren, B.; Zhang, X.; Zhao, M.; Wang, X.; Ye, J.; Wang, D., Significant enhancement in photocatalytic activity of $(GaN)_{1-x}(ZnO)_x$ nanowires via solubility and crystal facet tailoring. *AIP Advances* **2018**, *8*, 015206.

(67) Miller, D. S.; Bard, A. J.; McLendon, G.; Ferguson, J., Catalytic water reduction at colloidal metal "microelectrodes". 2. Theory and experiment. *Journal of the American Chemical Society* **1981**, *103*, 5336-5341.

(68) Scanlon, M. D.; Peljo, P.; Méndez, M. A.; Smirnov, E.; Girault, H. H., Charging and discharging at the nanoscale: Fermi level equilibration of metallic nanoparticles. *Chemical Science* **2015**, *6*, 2705-2720.

Chapter 4: Comparison of Electronic Structure in Heterogeneous and Homogeneous $(Ga_{1-x}Zn_x)(N_{1-x}O_x)$ Nanocrystals

4.1 Introduction

$(Ga_{1-x}Zn_x)(N_{1-x}O_x)$ is a solid solution of GaN and ZnO with a compositionally-tunable visible bandgap, making it an intriguing candidate for artificial photosynthesis applications.[1-10] The visible light absorption in $(Ga_{1-x}Zn_x)(N_{1-x}O_x)$ has been proposed to originate from the orbital repulsion caused by having Ga, N, Zn, and O in the same crystal lattice, specifically from the Zn 3d and N 2p repulsion.[11-16] It is proposed that the orbital repulsion causes the valence band to shift to higher energies, which narrows the bandgap and puts it into the visible region. The conduction band is thought to be made up of only GaN or ZnO orbitals but not both.[17-18] Learning more about the electronic band structure of $(Ga_{1-x}Zn_x)(N_{1-x}O_x)$ is important for understanding how it behaves as a light absorber for photocatalysis.

$(Ga_{1-x}Zn_x)(N_{1-x}O_x)$ was originally synthesized as a bulk material,[19] but since then researchers have found a variety of ways to synthesize $(Ga_{1-x}Zn_x)(N_{1-x}O_x)$ on the nanoscale.[11-12, 15, 20-25] Working with nanoscale $(Ga_{1-x}Zn_x)(N_{1-x}O_x)$ is advantageous due to the higher surface to volume ratio found with nanoscale particles, which can increase catalytic activity. As published previously by our group,[26] our nanoscale synthesis method results in $(Ga_{1-x}Zn_x)(N_{1-x}O_x)$ particles with a heterogeneous elemental distribution when performed at 650 °C and a homogeneous distribution when done at 800 °C. Having a heterogeneous sample could cause spatial variations in the bandgap or potentially lead to catalytic issues, such as grain boundaries. Presently, most studies of the optical properties of this material are accomplished using UV-visible diffuse reflectance spectroscopy on $(Ga_{1-x}Zn_x)(N_{1-x}O_x)$ powders and tend to show a broad band of absorbance that spans the UV and goes into the visible region.[14-15, 24, 27-29] It is possible that the absorbance is broad due to a distribution of bandgaps or because of the heterogeneity of the particles; however, the diffuse reflectance measurements can only provide ensemble data. Spatially resolved measurements of individual particles are needed to understand the mechanisms of broadening and effects of compositional inhomogeneity on light absorption.

In order to study $(Ga_{1-x}Zn_x)(N_{1-x}O_x)$ on a single particle level, electron energy loss spectroscopy (EELS) was employed to investigate the electronic band structure. We find a consistent EELS spectrum throughout a particle implying that the electronic band structure is uniform; this is true whether the particle is homogeneous or heterogeneous. Additionally, the EELS spectrum for the heterogeneous $(Ga_{1-x}Zn_x)(N_{1-x}O_x)$ particles shows two distinct transitions in the UV and visible, while homogeneous $(Ga_{1-x}Zn_x)(N_{1-x}O_x)$ particles only show one transition. These findings suggest that inhomogeneity in $(Ga_{1-x}Zn_x)(N_{1-x}O_x)$ particles leads to two band-like transitions within the semiconductor, but these transitions do not show spatial localization to particular parts of the particle. This also suggests that despite the inhomogeneous nature of the synthesis, the particles have a relatively uniform electronic band structure. This increased understanding of compositional effects will enhance future ability to utilize $(Ga_{1-x}Zn_x)(N_{1-x}O_x)$ in light absorbing applications.

4.2 Materials and Methods

4.2.1 Chemicals

Benzyl ether (98%), hexane (99%), toluene (99.5%), zinc acetylacetonate hydrate ($Zn(acac)_2$, zinc chloride ($ZnCl_2$, ≥98%), gallium acetylacetonate ($Ga(acac)_3$, 99.99%), 3-

mercaptopropionic acid (3-MPA, ≥99.0%), 1,2-hexadecanediol (90%), oleic acid (≥99.0%), oleylamine (70%), and tetramethylammonium hydroxide pentahydrate (≥97%), 99.995%) were purchased from Sigma-Aldrich. Methanol (99.9%), 2-propanol (99.9%), and sodium hydroxide (NaOH pellets, 99.3%) were purchased from Fisher. 1,2-ethanediol (99.8%) was purchased from Macron Fine Chemicals. Ethanol (95%) was purchased from Decon Labs. Ammonia (99.99%) was purchased from Airgas. All chemicals were purchased commercially and used without further purification.

4.2.2 ZnO Nanocrystal Synthesis

10 nm ZnO NCs were synthesized as detailed in Chapter 2.

4.2.3 $ZnGa_2O_4$ Nanocrystal Synthesis

$ZnGa_2O_4$ NCs were synthesized as detailed in Chapter 2.

4.2.4 $(Ga_{1-x}Zn_x)(N_{1-x}O_x)$ Nanocrystal Synthesis

$(Ga_{1-x}Zn_x)(N_{1-x}O_x)$ NCs were synthesized as detailed in Chapter 2.

4.2.5 Diffuse Reflectance Spectroscopy and Kubelka-Munk Plots

Diffuse reflectance measurements were done on an Agilent Cary 60 UV-Vis spectrophotometer with the Agilent Cary 60 Remote Diffuse Reflectance Accessory (DRA). A Spectralon puck was used as the reference and the diffuse reflectance spectra were converted to Kubelka-Munk plots using the Kubelka-Munk equation: $F(R_\infty)=(1-R_\infty)^2/2R_\infty$, where $R_\infty=R_{sample}/R_{reference}$.

4.2.6 Energy-Dispersive X-ray Spectroscopy Analysis

The scanning transmission electron microscopy-energy dispersive X-ray spectroscopy (STEM-EDS) data was collected using an FEI Titan microscope operated at 80 kV and an FEI

Talos F200X microscope operated at 200 kV. Both microscopes were equipped with Super-X EDS systems with four silicon drift detectors (SDDs). The analysis of the STEM-EDS data was done on Bruker Esprit software as described previously.[26]

4.2.7 Electron Energy Loss Spectroscopy Analysis

EELS data was collected on an aberration-corrected FEI TEAM 0.5 Titan microscope operated at 80 kV and on an FEI Titan Themis STEM equipped with a monochromator and a Gatan Quantum ERS electron spectrometer operated at 80 kV with energy dispersion per channel of 0.01 eV and a pixel dwell time of 0.002 s. TEM samples were prepared either by picking up dry powder onto a holey carbon film supported by a 300-mesh copper TEM grid or by dropping solutions on a ultrathin carbon film TEM grid.

The EELS data was analyzed using a software package called Hyperspy. A general procedure for processing an EELS spectrum in Hyperspy starts with aligning the zero-loss peak for all of the pixels in the spectrum image followed by fitting the zero-loss peak tail to a power law near the energy transition of interest and subtracting the fitted zero-loss peak from the spectrum. Next, an optional spike removal tool is run to remove any spikes in the data. Lastly, non-negative matrix factorization (NMF) is used to denoise the data. After the data was processed in Hyperspy it was imported into MATLAB for further analysis including bandgap fitting and generation of bandgap maps.

4.3 Results and Discussion

The synthesis procedure employed here results in a $(Ga_{1-x}Zn_x)(N_{1-x}O_x)$ nanoscale product with different elemental distributions depending on the synthesis temperature. When performed at

650 °C, the synthesis results in heterogeneous "core/shell-like" particles seen on the left in Figure 4.1. When performed at 800 °C, the result is homogeneous particles seen on the right in Figure 4.1. We hypothesized that this is due to the topotactic nucleation mechanism of synthesis, the amount of thermal energy for diffusion available at 650 °C versus 800 °C,[30-32] and an increase in Zn vacancies and NH_3 decomposition at higher temperatures.[32-33] With enough vacancies, NH_3 decomposition, and thermal energy for diffusion at 800 °C, the Ga and N ions are able to diffuse fully through the particles, while at 650 °C there is potentially not enough vacancies, or NH_3 decomposition, or thermal energy for full diffusion, so the Ga and N remain near the edges of the particle.

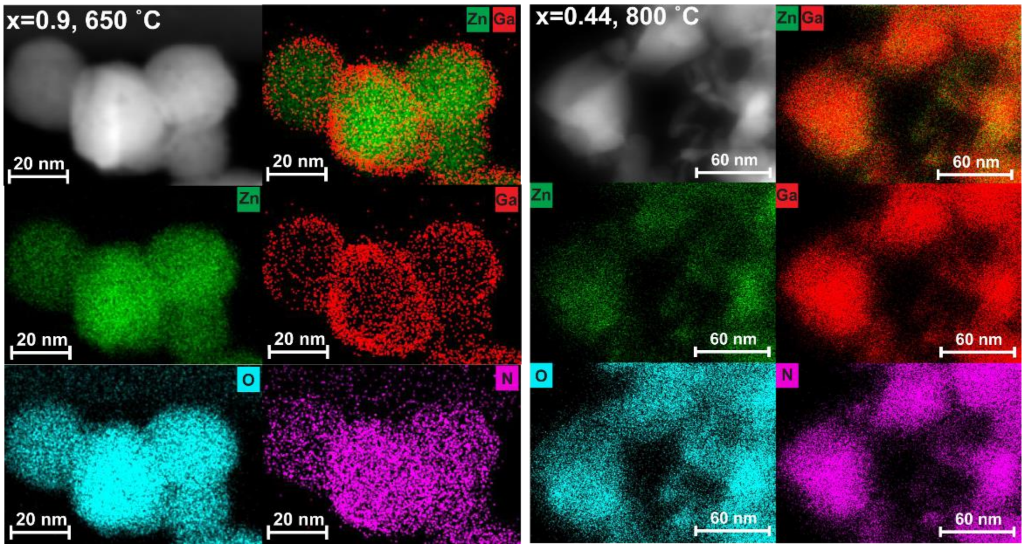

Figure 4.1: HAADF-STEM image and EDS maps of an x=0.9 $(Ga_{1-x}Zn_x)(N_{1-x}O_x)$ sample synthesized at 650 °C (left) and an x=0.44 $(Ga_{1-x}Zn_x)(N_{1-x}O_x)$ sample synthesized at 800 °C (right). The EDS maps show individual elements Zn, O, Ga, and N, along with a map of Zn/Ga overlaid.

Studies of the $(Ga_{1-x}Zn_x)(N_{1-x}O_x)$ material have been mostly limited to ensemble measurements and the bulk material.[3, 19, 34-41] As the research in the area has progressed, there have been more nanoscale $(Ga_{1-x}Zn_x)(N_{1-x}O_x)$ materials created and studied.[11-12, 15, 20-25] In terms of characterization, most data have been for ensemble measurements like UV-vis, diffuse reflectance, XRD, etc.[3, 19, 34-41] A few exceptions are some EDS studies of bulk and nanoscale $(Ga_{1-x}Zn_x)(N_{1-x}O_x)$.[13, 16, 24, 26, 39, 42-44] A specific example of an ensemble measurement is the diffuse reflectance measurement that most researchers do for $(Ga_{1-x}Zn_x)(N_{1-x}O_x)$.[14-15, 24, 27-29] Since the product is usually a powder, diffuse reflectance is the technique of choice rather than UV-vis spectroscopy, which requires a dissolved solution. Figure 4.2 shows Kubelka-Munk plots of the two $(Ga_{1-x}Zn_x)(N_{1-x}O_x)$ samples discussed in this study, whose EDS maps are shown in Figure 4.1.

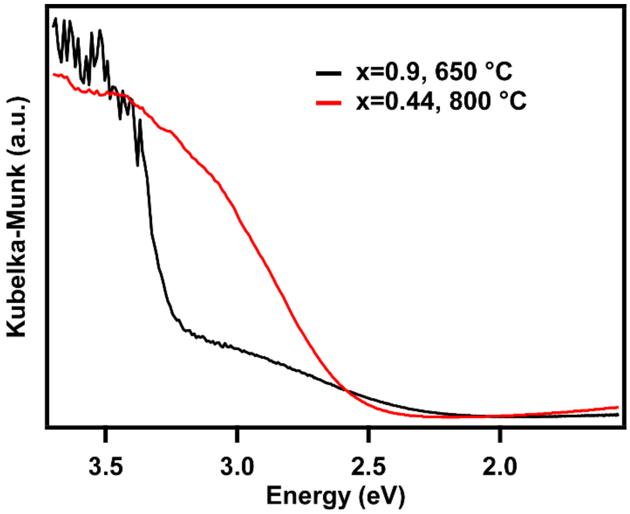

Figure 4.2: Kubelka-Munk plots of the x=0.9, 650 °C sample (black) and the x=0.44, 800 °C sample (red).

The Kubelka-Munk plot of the x=0.9, 650 °C sample has two different optical transitions, one in the UV and one in the visible region, while the plot of the x=0.44, 800 °C sample has only one transition. This is interesting information considering that we know from our EDS studies (Figure 4.1) that the elemental distributions of the two samples are also different, the 650 °C sample having a heterogeneous "core/shell-like" distribution and the 800 °C having a homogeneous elemental distribution. The two features in the Kubelka-Munk plot for the 650 °C sample reflect the two regions of elemental distribution in the 650 °C particles. It is possible that this correlation is a feature of the fact that the Kubelka-Munk plot is an ensemble measurement and not a single particle measurement; however, without single particle data it is difficult to know. This lack of single particle and spatially resolved characterization of $(Ga_{1-x}Zn_x)(N_{1-x}O_x)$ is one of the main factors motivating our investigation. By analyzing our $(Ga_{1-x}Zn_x)(N_{1-x}O_x)$ samples with EELS we can get single particle information and see how that information compares to the bulk ensemble measurements like Kubelka-Munk plots.

EELS is a powerful technique to study single particles as evidenced by many nanoscale studies reported in the current EELS literature.[45-52] EELS involves an electron beam being transmitted through a sample where the electrons from the beam interact with the electrons in the atoms of the sample via inelastic scattering, causing excitations within the particle and a loss of energy from the electron beam which is then detected and plotted as a spectrum of energy loss. One of the frequently studied features in a low-loss EELS spectrum is the bandgap energy transition, which is usually found at energy losses <10 eV.[48] Some of the bandgap measurement studies in the current EELS literature are of CdSe quantum dots (QDs),[51] PbS QDs,[46] solar cell materials like CIGS[53] and others.[45, 52, 54-57] EELS is used to gather many other sets of data besides bandgap measurements including vibrational mode measurements,[50, 58] plasmon energy measurements,[47-49] and various core-loss measurements which give elemental composition information.[47, 52, 56, 59]

A key feature that enables investigation of a wider range of energy losses through EELS is an electron beam monochromator.[47-48, 50] In an electron microscope, a monochromator is either made up of a magnetic prism or a Wien filter which spatially disperse the electrons in the beam by energies, selects a narrow range of energies using a monochromating slit and then recompresses the selected electrons back into a beam. Monochromators are especially important for low-loss EELS, like bandgap measurements, because low-loss signals are close to the zero loss peak (ZLP) and the monochromator not only reduces the (full width at half max) FWHM of the ZLP but it also helps minimize the length of the ZLP tail, both of which help resolve low-loss signals.[48] Monochromators help to improve EELS energy resolution because the energy resolution is limited, in part, by the dispersion width of electron energies coming out of the gun, which is commonly characterized as the FWHM of the ZLP peak.[48] Components that impact the spatial resolution of EELS measurements include broadening due to elastic scattering that increases with sample thickness, the inherent delocalization of the inelastic scattering which comes from the limited angular range of inelastic scattering, and radiation damage to the sample from the electron beam.[47]

One advantage of EELS is that it can give single particle information with nanometer spatial resolution by coupling it to a STEM, which allows the collection of data with high spatial resolution because the STEM raster-scans the electron beam across the sample. This results in an EELS spectrum being collected at each position of the electron probe beam.[47] This can facilitate spatial investigation of single nanoparticles with heterogeneous compositions and can inform how the change in composition will change the electronic structure of the nanoparticle. This is one of the main reasons we are using EELS to investigate our material, so that we can study the electronic band structure of individual particles.

4.3.1 Electronic Structure of Pure ZnO Nanoparticles

In order to understand the electronic structure of $(Ga_{1-x}Zn_x)(N_{1-x}O_x)$ nanocrystals we start by studying the electronic structure of pure ZnO nanoparticles (d = ~10 nm), one of the precursors for the $(Ga_{1-x}Zn_x)(N_{1-x}O_x)$ synthesis. ZnO is an important precursor in the $(Ga_{1-x}Zn_x)(N_{1-x}O_x)$ synthesis because it serves as the template for the Ga and N ions to diffuse into.[26] Additionally, for the samples synthesized at 650 °C, there tend to be regions of mostly ZnO, usually in the center of the particles. Hence, understanding what the ZnO EELS spectrum looks like can help us better understand the EELS spectrum of $(Ga_{1-x}Zn_x)(N_{1-x}O_x)$, especially for the heterogeneous $(Ga_{1-x}Zn_x)(N_{1-x}O_x)$ nanocrystals.

The EELS spectrum in Figure 4.3(b) is point data taken on a ZnO nanoparticle, shown in Figure 4.3(a), which shows a single sharp, linear energy transition between 3.0-3.5 eV, which is the ZnO bandgap transition. The ZnO energy transition was linearly fit between ~3.1-3.6 eV and where the linear fit intersects the baseline (~2.2-3.0 eV) is the value of the bandgap for the sample. In this case the bandgap is 3.14 eV, which is a good approximation to the bulk bandgap of ZnO.[60-64]

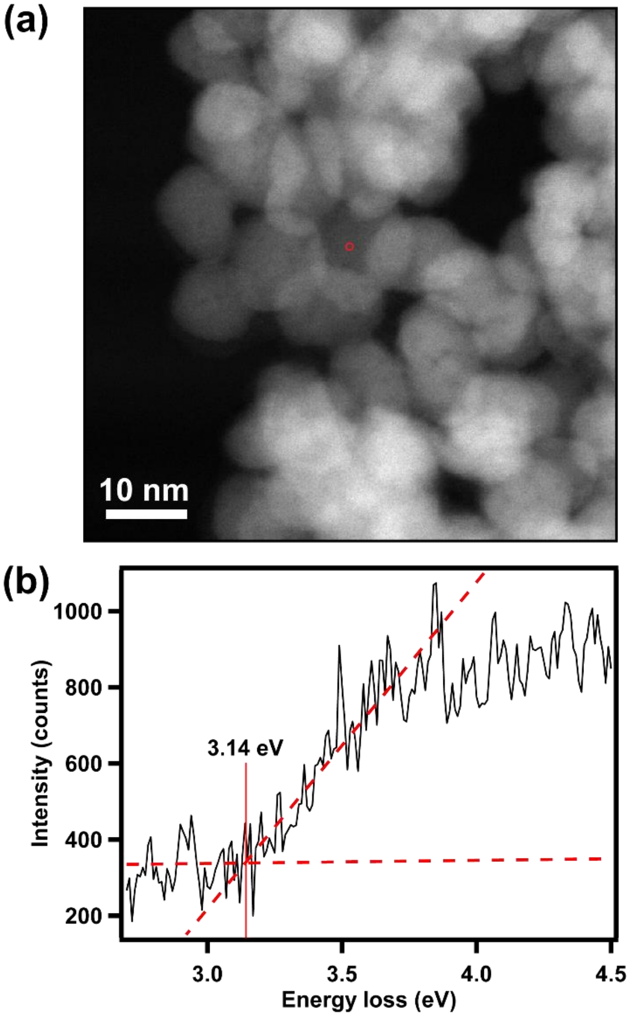

Figure 4.3: (a) EELS spectrum image with a red circle indicating where the point data was taken. (b) EELS spectrum of a pure ZnO nanoparticle. The intersection of the linear fit with the baseline gives a bandgap value of 3.14 eV.

The spectrum shown in Figure 4.3(b) shows only one energy transition (one linear rise in the spectrum), just like there is only one compositional region, since the particles are pure ZnO and not a combination like $(Ga_{1-x}Zn_x)(N_{1-x}O_x)$. Having understood this type of homogeneous particle, we now move on to discuss the homogeneous $(Ga_{1-x}Zn_x)(N_{1-x}O_x)$ system.

4.3.2 Electronic Structure in Homogeneous $(Ga_{1-x}Zn_x)(N_{1-x}O_x)$ Nanocrystals

We begin by analyzing the homogeneous $(Ga_{1-x}Zn_x)(N_{1-x}O_x)$ particles synthesized at 800 °C. The EDS elemental map in Figure 4.4(b) shows a homogeneous distribution of Ga and Zn throughout the $(Ga_{1-x}Zn_x)(N_{1-x}O_x)$ particle, which is characteristic to $(Ga_{1-x}Zn_x)(N_{1-x}O_x)$ samples synthesized at 800 °C. In order to obtain absorbance-proportional data, diffuse reflectance spectra were collected and converted using the Kubelka-Munk equation. Figure 4.4(c) compares the Kubelka-Munk spectrum (black trace) to EELS spectra (red series) gathered at various locations in a particle, which are denoted by the red boxes in Figure 4.4(d). Qualitatively, the Kubelka-Munk and EELS spectra have similar shapes, indicating that the electronic band structure in one single particle is similar to the optical response seen from the overall bulk ensemble sample. This correlation between the optical spectrum and the EELS spectrum has also been seen in other EELS studies.[50, 65] The five EELS spectra taken from different locations in the particle qualitatively do not change shape, indicating that the electronic band structure stays relatively constant throughout a homogeneous particle. However, the spectra do shift in energy and intensity giving us an energy transition spread of about +/- 0.2 eV, which could be due to a variety of causes like Cherenkov radiation,[50, 54-55] multiple scattering events,[46] ZLP subtraction,[59, 65] fitting range of the bandgap,[47-48] sample thickness increasing or decreasing which would cause an increase of decrease in broadening, respectively,[46] and changes in composition, lattice strain, and orbital repulsion.[1-4] Despite the energy and intensity shifting, particles with homogeneous elemental distributions also have homogeneous electronic band structures, as evidenced by the spectra only having one energy transition, similar to how the pure ZnO spectrum only has one energy transition. This correlates the single homogeneous compositional region with the single electronic transition as we have now seen in both the pure ZnO and the homogeneous $(Ga_{1-x}Zn_x)(N_{1-x}O_x)$ sample.

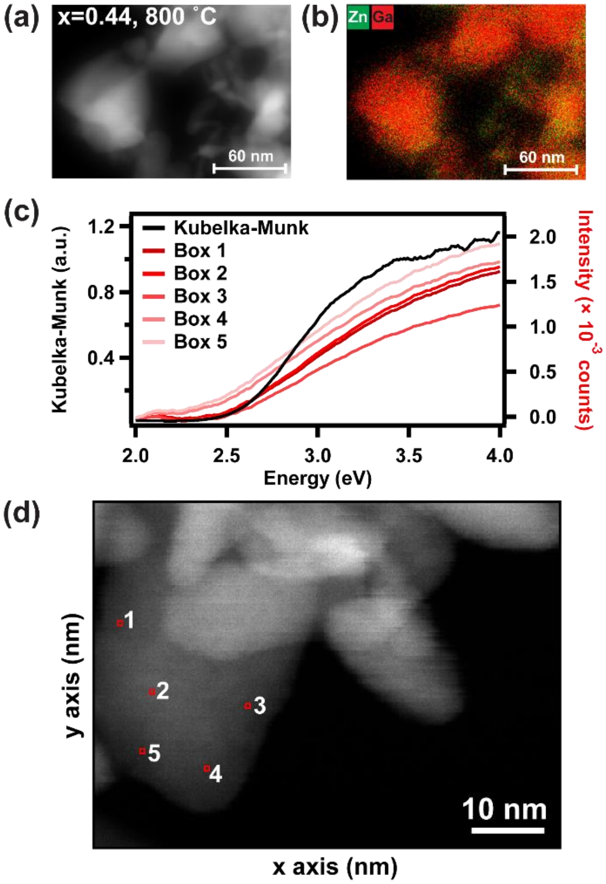

Figure 4.4: (a) HAADF image and (b) EDS elemental map of a $(Ga_{1-x}Zn_x)(N_{1-x}O_x)$ sample with x=0.44 synthesized at 800 °C. (c) Plot comparing the absorbance-proportional Kubelka-Munk spectrum with EELS spectra at different locations in a $(Ga_{1-x}Zn_x)(N_{1-x}O_x)$ particle. The EELS spectra are normalized to the zero-loss peak intensity. (d) HAADF image with numbered boxes indicating the places from which the spectra in (c) were taken.

To visualize variation in the bandgap throughout a single particle, we determine the bandgap value at each pixel through iterative linear fitting and transform these values into a bandgap colormap using MATLAB. The colormaps are images created by assigning a certain pixel a color depending on the value of the bandgap obtained at that pixel. Figure 4.5 shows high angle annular dark field (HAADF)-STEM images and bandgap colormaps for the x=0.44 $(Ga_{1-x}Zn_x)(N_{1-x}O_x)$ particles synthesized at 800 °C. The colormaps show that the bandgap energy has a range of ± 0.1-0.3 eV throughout a particle. The colormaps reflect the distribution in bandgap values seen due to the shift in energy in the EELS spectra in Figure 4.5(c). Particularly, in colormap 3b in Figure 4.5, a larger range of bandgap values is seen. Colormap 3b contains two particles, the one on the right looks to have about the same bandgap values throughout; however, the particle on the left has a region on the bottom tip that is 0.2-0.3 eV more than the top end of the same particle. This difference could be due to thickness variation, but this is not seen in the HAADF-STEM image in colormap 3a. This larger difference could be due to compositional changes within this specific particle, although, in general these particular samples are expected to be homogeneous compositionally. To make a firm conclusion about this particle, it is necessary to have both low-loss and core-loss EELS data, which would provide band gap data and elemental composition data at the same location. Without both core-loss and low-loss data, it is difficult to conclude why there is such a large band gap distribution in this particle.

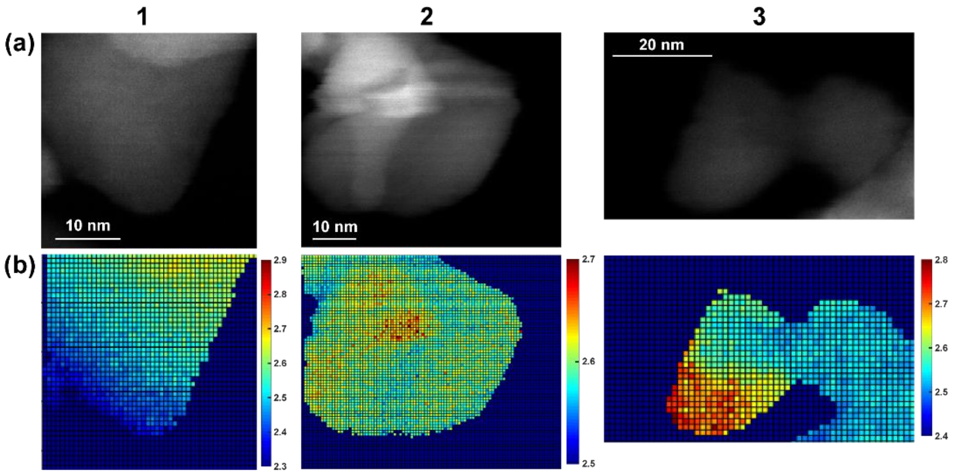

Figure 4.5: (a) Dark field images of three different x=0.44, 800 °C $(Ga_{1-x}Zn_x)(N_{1-x}O_x)$ particles. (b) Colormaps of the bandgap energy transition values. Column 1 contains the dark field image and colormaps for one particle, while columns 2 and 3 both contain the dark field images and colormaps for two other, different particles.

The bandgap colormaps show that two particles have a bandgap value range of about 0.1 eV and two other particles have a range of about 0.2-0.3 eV. Based on the FWHM of the zero-loss peak, the energy resolution of the EELS measurement is about 0.11 eV, which would translate into an uncertainty of about ± 0.11 eV, meaning some of the distribution we see is within the uncertainty range. Also, the EELS signal changes depending on where the signal is taken in or around the particle. The closer the data is to the center of the particle or the more the thickness increases, the more the EELS signal will broaden and the more multiple scattering events can occur.[46] Alternatively, the visible bandgap is hypothesized to come from the orbital repulsion and mixing that happens when GaN and ZnO are combined into one lattice.[1-4, 6-10, 66-67] It is possible that the mixing and repulsion could change throughout a crystal lattice and therefore the bandgap value could change slightly over a particle. However, overall, we see that the homogeneous $(Ga_{1-x}Zn_x)(N_{1-x}O_x)$ particles have a single electronic transition in the visible region and that the shape of that transition stays the same throughout an entire particle. Next, we can see how the homogeneous $(Ga_{1-x}Zn_x)(N_{1-x}O_x)$ particle's electronic structure compares to a heterogeneous $(Ga_{1-x}Zn_x)(N_{1-x}O_x)$ particle's electronic structure.

4.3.3 Electronic Structure in Heterogeneous $(Ga_{1-x}Zn_x)(N_{1-x}O_x)$ Nanocrystals

Next, we investigate how the electronic band structure changes when studying a heterogeneous "core/shell-like" $(Ga_{1-x}Zn_x)(N_{1-x}O_x)$ particle. When $(Ga_{1-x}Zn_x)(N_{1-x}O_x)$ particles are synthesized at 650 °C the resulting particles have a heterogeneous elemental distribution of Ga and Zn. The distribution of Ga and Zn is roughly "core/shell-like" but not exactly core-shell as many nanostructures are purposefully synthesized to be. The resulting heterogeneous $(Ga_{1-x}Zn_x)(N_{1-x}O_x)$ particles still show visible absorption like the homogeneous particles do, however at high x-values (high ZnO content) the optical absorbance spectra show a UV absorption component in addition to the visible absorption component as seen in the black trace in Figure 4.6. We will investigate the electronic band structure of a single $(Ga_{1-x}Zn_x)(N_{1-x}O_x)$ nanoparticle to see if we find the same UV and visible components as in the optical absorbance spectra and we will investigate how the electronic band structure changes throughout a heterogeneous particle.

Figure 4.6 shows the HAADF image, EDS elemental map, Kubelka-Munk spectrum, EELS spectrum, and EELS spectrum image for a $x=0.9$ $(Ga_{1-x}Zn_x)(N_{1-x}O_x)$ sample synthesized at 650 °C. The EDS elemental map shows a heterogeneous distribution of Ga and Zn, with Ga and N concentrated more towards the edges of the particle and Zn and O concentrated more in the center of the particle. The mechanism leading to heterogeneous or homogeneous elemental distribution is discussed in detail in our previous publication;[26] however, the essential reasoning is that at 650 °C there is not enough vacancies, NH_3 decomposition, or thermal energy for the Ga and N to diffuse fully through the entire particle, but at 800 °C there is enough for complete diffusion. Figure 4.6(c) compares the absorbance-proportional Kubelka-Munk spectrum to EELS spectra taken in various places in a particle, shown in Figure 4.6(d) with red boxes. As seen with the homogeneous particles above, here we also see that the Kubelka-Munk spectrum and the EELS spectra share a similar shape and that the shape is maintained throughout the particle, with some changes in intensity and shift in energy.

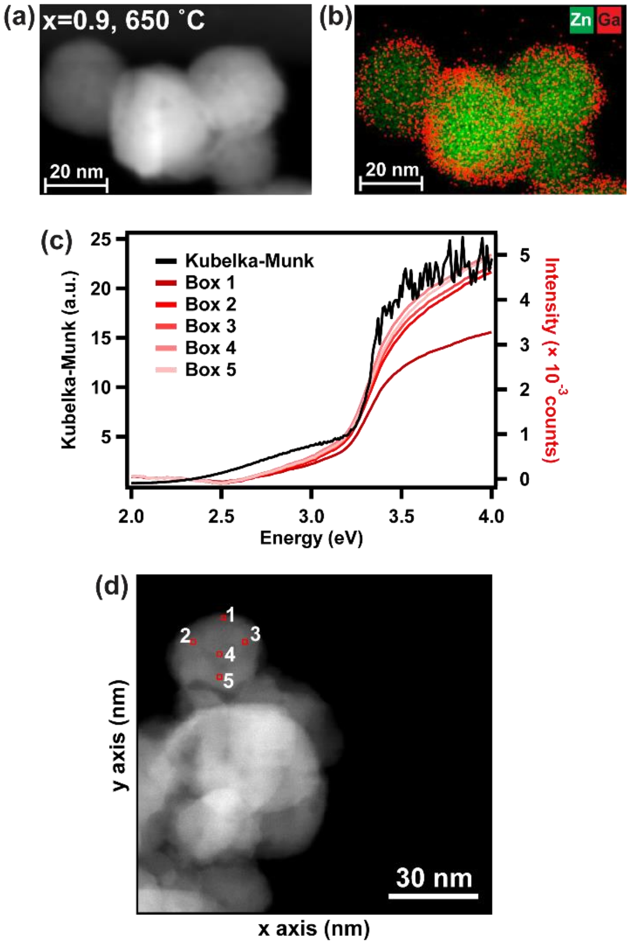

Figure 4.6: (a) HAADF image and (b) EDS elemental map of a $(Ga_{1-x}Zn_x)(N_{1-x}O_x)$ particle with x=0.9 synthesized at 650 °C, scale bar is 20 nm. (c) Plot comparing the absorbance-proportional Kubelka-Munk spectrum with EELS spectra at different locations in a $(Ga_{1-x}Zn_x)(N_{1-x}O_x)$ particle. The EELS spectra are normalized to the zero-loss peak intensity. (d) EELS spectrum image with numbered boxes indicating the pixels from which the spectra in (c) were taken.

The EDS map in Figure 4.6(b) shows that the $(Ga_{1-x}Zn_x)(N_{1-x}O_x)$ particle has two distinct compositional regions, a center that is mostly ZnO and the edges which are mostly $(Ga_{1-x}Zn_x)(N_{1-x}O_x)$. This is reflected in the EELS spectra in Figure 4.6(c) where we see two distinct energy transitions. The two different energy transitions could be directly correlated with the two different elemental distribution regions. A more intriguing finding is that the shape of the EELS spectrum doesn’t change when sampled in different parts of the particle, meaning that even if we are sampling in the ZnO center or the $(Ga_{1-x}Zn_x)(N_{1-x}O_x)$ edge, we still see the same shape of the EELS spectrum no matter what, indicating that the electronic band structure may be the same over the entire particle.

The spectral shapes are the same for absorbance and EELS spectra throughout the heterogeneous particle, just as we saw with the homogeneous particle. Having corresponding spectral features supports the idea that the ensemble optical properties correspond to the single particle electronic properties, as we hypothesized with the homogeneous particles. Also, the EELS spectrum does not change shape as spectra are taken from different spatial areas in a particle. There is some inherent signal delocalization and limits to the spatial resolution;[65] however, the particles are large enough that we would see some differences between the farthest points if there were any differences to detect. It also appears that the shape staying the same is a real phenomenon even accounting for delocalization and limits to the spatial resolution. Meaning that the electronic structure for a heterogeneous $(Ga_{1-x}Zn_x)(N_{1-x}O_x)$ particle appears to be similar throughout the particle and not different in the center vs the edge. However, as with the homogeneous $(Ga_{1-x}Zn_x)(N_{1-x}O_x)$ particles, there is a shift in energies and a change in the intensity of the EELS spectrum in different locations in a particle, which results in a distribution of bandgap values.

In order to visualize how much the bandgap is changing throughout a single particle, we can plot the bandgap value at each pixel and create a colormap as was done for the homogeneous particles. Figure 4.7 shows HAADF-STEM images and bandgap colormaps for the x=0.9 $(Ga_{1-x}Zn_x)(N_{1-x}O_x)$ particles synthesized at 650 °C. There are two colormaps for each HAADF-STEM image because the x=0.9, 650 °C sample has two different energy transitions in its EELS spectrum as shown in Figure 4.7(c) – therefore, there are colormaps for the lower energy transition (labeled visible) and for the higher energy transition (labeled UV). Both the visible and the UV colormaps show that the bandgap values have a range. The visible colormaps have a range of values of about 0.1-0.2 eV, while the UV colormaps have a range of about 0.5-0.1 eV.

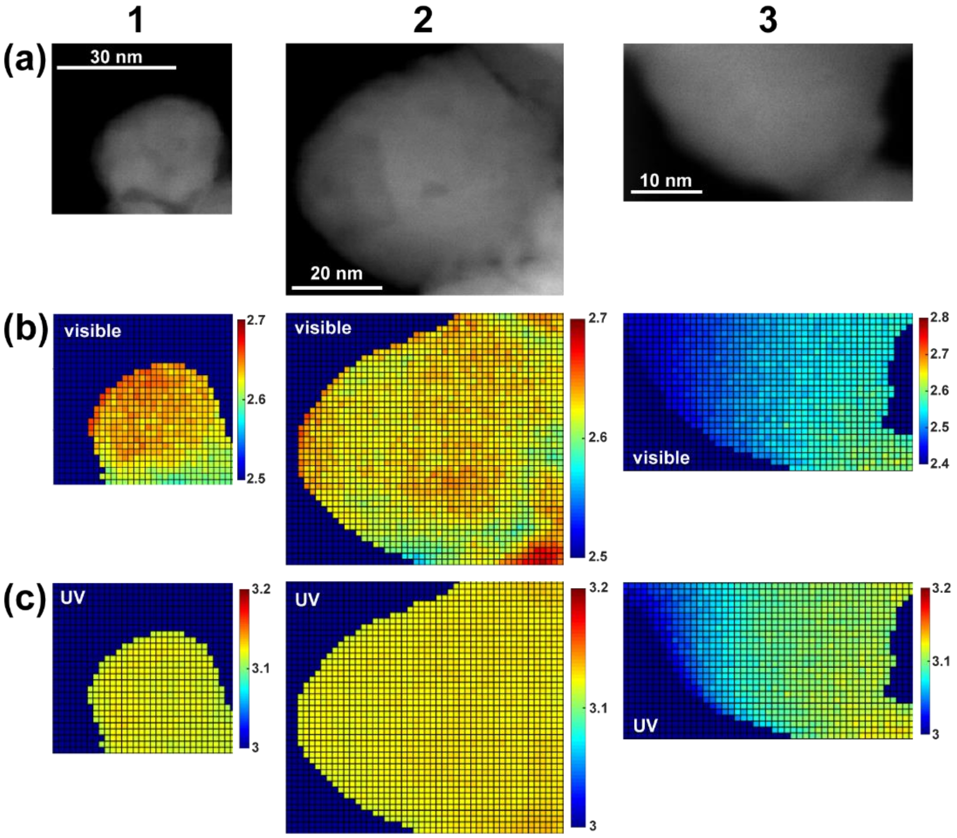

Figure 4.7: (a) HAADF-STEM images of three different x=0.9, 650 °C $(Ga_{1-x}Zn_x)(N_{1-x}O_x)$ particles. (b) Colormaps of the visible, lower energy transition bandgap values. (c) Colormaps of the UV, higher energy transition bandgap values. Column 1 contains the dark field image and colormaps for one particle, while columns 2 and 3 both contain the dark field images and colormaps for two other, different particles.

One notable thing is that the distribution in both the UV and visible bandgap values for the heterogeneous $(Ga_{1-x}Zn_x)(N_{1-x}O_x)$ particles is smaller than it was for the homogeneous particles.

This could perhaps be due to the particle only having $(Ga_{1-x}Zn_x)(N_{1-x}O_x)$ at the edges of the particle and not throughout the entire particle. Having a smaller $(Ga_{1-x}Zn_x)(N_{1-x}O_x)$ compositional region could lead to a smaller distribution of orbital repulsion and mixing differences, making it so that there is a narrower bandgap value distribution. As mentioned above for the homogeneous $(Ga_{1-x}Zn_x)(N_{1-x}O_x)$ particles, the distribution in bandgaps could be because of how the visible bandgap is formed. Since the visible absorption comes from the repulsion of all of the orbitals mixing, and mostly Zn and N repelling, the local environment in the particle would have a lot to do with the exact bandgap value. So, if in one area there is a lot more repulsion and lattice strain, the bandgap might be smaller because that could cause the valence band (VB) to shift higher in energy. In another spot there might be less repulsion and strain, causing the VB to shift lower in energy and then there would be a slightly larger visible bandgap. Thus, the reason that the visible bandgap values could have a distribution is because there's a lot of variance in lattice strain and orbital repulsion in the particle, meaning there's slightly different mixing of the atoms and orbitals, causing the bandgap to vary. The same doesn't appear to be true for the UV bandgap, which could be because the UV bandgap comes from the pure ZnO regions and does not depend on orbital repulsion and strain to create the bandgap. Additionally, the variance could come from experimental uncertainty like the ZLP subtraction method, the bandgap fitting range, any sample thickness variations, or multiple scattering events, which would be more common in the center of the particles.

To confirm that the electronic band structure is similar even in regions with different composition, core-loss and low-loss EELS data were gathered at two points in a x=0.89 $(Ga_{1-x}Zn_x)(N_{1-x}O_x)$ particle as shown in Figure 4.8. Figure 4.8(d) shows the HAADF-STEM image of the cluster of $(Ga_{1-x}Zn_x)(N_{1-x}O_x)$ particles and the two points where core-loss and low-loss data were collected. The data from the area denoted by the red circle is seen in Figure 4.8(a) and the red trace in Figure 4.8(c), which shows that there is nitrogen present at that location as evidenced by the small peak near 400 eV. The data from the area marked by the blue circle is shown in Figure 4.8(b) and the blue trace in Figure 4.8(c), which shows that there is no nitrogen present at the location, deduced by the lack of a peak near 400 eV. Knowing that the red data is from a spot containing nitrogen ($(Ga_{1-x}Zn_x)(N_{1-x}O_x)$) and the blue data is from a spot with no nitrogen (ZnO) allows us to compare the low-loss spectra Figure 4.8 (a) and (b) to see that even in locations with different composition, the shape of the EELS spectrum is still similar. This supports the hypothesis that the electronic band structure is similar throughout the particle regardless of elemental makeup.

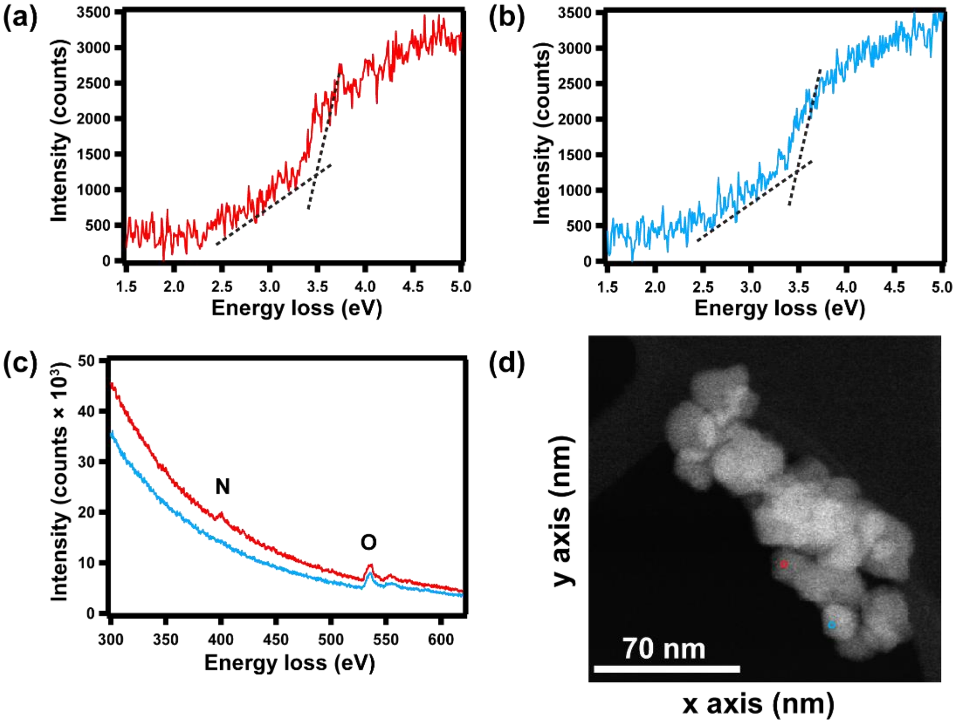

Figure 4.8: (a) and (b) show EELS spectra for two different spots denoted in (d). (c) is a plot of two core-loss spectra for the same two spots denoted in (d) indicating the presence (red) or absence (blue) of nitrogen. (d) shows a HAADF-STEM image of the cluster of $(Ga_{1-x}Zn_x)(N_{1-x}O_x)$ particles where the data in (a)-(c) were taken; the red circle shows the location where the spectrum in (a) and the red trace in (c) were taken, while the blue circle shows the location where the spectrum in (b) and the blue trace in (c) were taken.

From our EELS studies we found that the number of regions of different elemental distribution in the particles tends to correlate with the number of energy transitions in the EELS spectrum. The heterogeneous particles had two major regions of different elemental composition and had two different energy transitions in their EELS spectrum, whereas the homogeneous particles with only one compositional region only had one energy transition in their EELS spectrum. We also found that the EELS spectrum shape tends to be similar to the shape of the Kubelka-Munk plot, meaning that the single particle measurement qualitatively matches the bulk ensemble measurement. We confirmed that, regardless of the composition at the spot that the EELS spectrum was taken (with or without N), the EELS spectrum still had a similar shape and additionally, we confirmed that the EELS spectrum has a similar shape over the entire particle. Lastly, we found that there is a distribution in the bandgap values determined from fitting the EELS spectra. The visible bandgap values had a larger distribution (0.1-0.3 eV) than the UV bandgap values (0.05-0.1 eV). Factors contributing to the distributions include inherent uncertainty in the EELS measurement, thickness variations, fitting range of the bandgap, ZLP subtraction, Cherenkov radiation, multiple scattering events and changes in composition, lattice strain, and orbital repulsion. Possible explanations for the distribution in bandgap values besides uncertainty (FWHM of the ZLP) and thickness variations could be that the visible bandgap comes from orbital repulsion and mixing in the valence band, which causes the valence band to increase in energy, decreasing the bandgap and pushing it into the visible region. It is possible that since there can be local disorder in the crystal lattice that the orbitals would mix and repel each other slightly differently throughout the particle which could cause a distribution in bandgap values since the valence band could be shifting slightly, even though the electronic band structure is thought to be similar over the entire particle.

4.4 Conclusions

Throughout this investigation of $(Ga_{1-x}Zn_x)(N_{1-x}O_x)$ nanocrystals using EELS, we have learned that the number of energy transitions in the EELS spectrum appears to correlate with the number of compositional regions in the particle and that the qualitative shape of the EELS spectrum is the same throughout the particle. This could have broader implications for the nature of excitation pathways in heterostructure nanomaterials and could confirm some hypotheses that their band structures are delocalized over the entire particle. Additionally, the single particle measurements qualitatively agree with the bulk ensemble measurement, which supports the idea that the phenomena that are seen in bulk ensemble measurements are meaningful on a single particle level. We did see energy shifting and that the intensity of the EELS spectrum changes for both homogeneous and heterogeneous $(Ga_{1-x}Zn_x)(N_{1-x}O_x)$ particles, which leads to a distribution in bandgap energy values. This could mean that, while the overall signal is delocalized, local signals could mix with neighboring signals to produce the overall distribution that we see in a particle. This is similar to having multiple scattering events occur inside a particle, which will alter the detected signal. The changing intensities could also be related to the hypothesis that the visible bandgap is formed due to orbital repulsion and mixing, causing the valence band to increase in energy and therefore decreasing the bandgap. It appears that the visible bandgap energy values have a slightly larger range than the UV bandgap values, which makes sense since the UV bandgap does not depend on orbital repulsion and mixing for its formation.

4.5 References

(1) Yu, H.-G., An optimal density functional theory method for GaN and ZnO. *Chemical Physics Letters* **2011**, *512*, 231-236.

(2) Di Valentin, C., Electronic Structure of $(Ga_{1-x}Zn_x)N_{1-x}O_x$ Photocatalyst for Water Splitting by Hybrid Hartree-Fock Density Functional Theory Methods. *Journal of Physical Chemistry C* **2010**, *114*, 7054-7062.

(3) Hirai, T.; Maeda, K.; Yoshida, M.; Kubota, J.; Ikeda, S.; Matsumura, M.; Domen, K., Origin of Visible Light Absorption in GaN-Rich $(Ga_{1-x}Zn_x)(N_{1-x}O_x)$ Photocatalysts. *Journal of Physical Chemistry C* **2007**, *111*, 18853-18855.

(4) Jensen, L. L.; Muckerman, J. T.; Newton, M. D., First-Principles Studies of the Structural and Electronic Properties of the $(Ga_{1-x}Zn_x)(N_{1-x}O_x)$ Solid Solution Photocatalyst. *Journal of Physical Chemistry C* **2008**, *112*, 3439-3446.

(5) McDermott, E. J.; Kurmaev, E. Z.; Boyko, T. D.; Finkelstein, L. D.; Green, R. J.; Maeda, K.; Domen, K.; Moewes, A., Structural and Band Gap Investigation of GaN:ZnO Heterojunction Solid Solution Photocatalyst Probed by Soft X-ray Spectroscopy. *Journal of Physical Chemistry C* **2012**, *116*, 7694-7700.

(6) Wei, W.; Dai, Y.; Yang, K. S.; Guo, M.; Huang, B. B., Origin of the visible light absorption of GaN-Rich $Ga_{1-x}Zn_xN_{1-x}O_x$ (x=0.125) solid solution. *Journal of Physical Chemistry C* **2008**, *112*, 15915-15919.

(7) Dou, M.; Persson, C., Band gap reduction and dielectric function of $Ga_{1-x}Zn_xN_{1-x}O_x$ and $In_{1-x}Zn_xN_{1-x}O_x$ alloys. *physica status solidi (a)* **2012**, *209*, 75-78.

(8) Huda, M. N.; Yan, Y. F.; Wei, S. H.; Al-Jassim, M. M., Electronic structure of ZnO:GaN compounds: Asymmetric bandgap engineering. *Physical Review B* **2008**, *78*, 195204.

(9) Li, L.; Muckerman, J. T.; Hybertsen, M. S.; Allen, P. B., Phase Diagram, Structure, and Electronic Properties of $(Ga_{1-x}Zn_x)(N_{1-x}O_x)$ Solid Solutions from DFT-Based Simulations. *Physical Review B* **2011**, *83*, 134202.

(10) Wang, S. Z.; Wang, L. W., Atomic and Electronic Structures of GaN/ZnO Alloys. *Physical Review Letters* **2010**, *104*, 065501.

(11) Zhang, Y.; Wu, Z.-F.; Gao, P.-F.; Fang, D.-Q.; Zhang, S.-L., Enhanced visible light absorption in ZnO/GaN heterostructured nanofilms. *Journal of Alloys and Compounds* **2017**, *704*, 478-483.

(12) Zhang, Y.; Fang, D.-Q.; Zhang, S.-L.; Huang, R.; Wen, Y.-H., Structural and electronic properties of ZnO/GaN heterostructured nanowires from first-principles study. *Physical Chemistry Chemical Physics* **2016**, *18*, 3097-3102.

(13) Yoshida, M.; Hirai, T.; Maeda, K.; Saito, N.; Kubota, J.; Kobayashi, H.; Inoue, Y.; Domen, K., Photoluminescence Spectroscopic and Computational Investigation of the Origin of the Visible Light Response of $(Ga_{1-x}Zn_x)(N_{1-x}O_x)$ Photocatalyst for Overall Water Splitting. *The Journal of Physical Chemistry C* **2010**, *114*, 15510-15515.

(14) RajaAmbal, S.; Yadav, A. K.; Jha, S. N.; Bhattacharyya, D.; Gopinath, C. S., Electronic structure-sunlight driven water splitting activity correlation of $(Zn_{1-y}Ga_y)(O_{1-z}N_z)$. *Physical Chemistry Chemical Physics* **2014**, *16*, 23654-23662.

(15) Menon, S. S.; Kuppulingam, B.; Baskar, K.; Sairam, T. N.; Ravindran, T. R.; Gupta, B.; Singh, S., Realization of high photocatalytic hydrogen generation activity by nanostructured $Ga_{1-x}Zn_xO_{1-z}N_z$ solid-solution without co-catalyst. *International Journal of Hydrogen Energy* **2015**, *40*, 13901-13908.

(16) Maeda, K.; Teramura, K.; Takata, T.; Hara, M.; Saito, N.; Toda, K.; Inoue, Y.; Kobayashi, H.; Domen, K., Overall Water Splitting on $(Ga_{1-x}Zn_x)(N_{1-x}O_x)$ Solid Solution Photocatalyst: Relationship between Physical Properties and Photocatalytic Activity. *Journal of Physical Chemistry B* **2005**, *109*, 20504-20510.

(17) Hashiguchi, H.; Maeda, K.; Abe, R.; Ishikawa, A.; Kubota, J.; Domen, K., Photoresponse of GaN:ZnO Electrode on FTO under Visible Light Irradiation. *Bulletin of the Chemical Society of Japan* **2009**, *82*, 401-407.

(18) Chuang, C.-H.; Lu, Y.-G.; Lee, K.; Ciston, J.; Dukovic, G., Strong Visible Absorption and Broad Time Scale Excited-State Relaxation in $(Ga_{1-x}Zn_x)(N_{1-x}O_x)$ Nanocrystals. *Journal of the American Chemical Society* **2015**, *137*, 6452-6455.

(19) Maeda, K.; Takata, T.; Hara, M.; Saito, N.; Inoue, Y.; Kobayashi, H.; Domen, K., GaN:ZnO Solid Solution as a Photocatalyst for Visible-Light-Driven Overall Water Splitting. *Journal of the American Chemical Society* **2005**, *127*, 8286-8287.

(20) Ren, B.; Zhang, X.; Zhao, M.; Wang, X.; Ye, J.; Wang, D., Significant enhancement in photocatalytic activity of $(GaN)_{1-x}(ZnO)_x$ nanowires via solubility and crystal facet tailoring. *AIP Advances* **2018**, *8*, 015206.

(21) Li, Y.; Zhu, L.; Yang, Y.; Song, H.; Lou, Z.; Guo, Y.; Ye, Z., A Full Compositional Range for a $(Ga_{1-x}Zn_x)(N_{1-x}O_x)$ Nanostructure: High Efficiency for Overall Water Splitting and Optical Properties. *Small* **2015**, *11*, 871-876.

(22) Han, W.-Q.; Liu, Z.; Yu, H.-G., Synthesis and Optical Properties of GaN/ZnO Solid Solution Nanocrystals. *Applied Physics Letters* **2010**, *96*, 183112.

(23) Hahn, C.; Fardy, M. A.; Nguyen, C.; Natera-Comte, M.; Andrews, S. C.; Yang, P. D., Synthesis and Photocatalytic Properties of Single Crystalline $(Ga_{1-x}Zn_x)(N_{1-x}O_x)$ Nanotubes. *Israel Journal of Chemistry* **2012**, *52*, 1111-1117.

(24) Adeli, B.; Taghipour, F., Facile synthesis of highly efficient nano-structured gallium zinc oxynitride solid solution photocatalyst for visible-light overall water splitting. *Applied Catalysis A: General* **2016**, *521*, 250-258.

(25) Adeli, B.; Taghipour, F., A Review of Synthesis Techniques for Gallium-Zinc Oxynitride Solar-Activated Photocatalyst for Water Splitting. *ECS J. Solid State Sci. Technol.* **2013**, *2*, Q118-Q126.

(26) Tongying, P.; Lu, Y.-G.; Hall, L. M. G.; Lee, K.; Sulima, M.; Ciston, J.; Dukovic, G., Control of Elemental Distribution in the Nanoscale Solid-State Reaction That Produces $(Ga_{1-x}Zn_x)(N_{1-x}O_x)$ Nanocrystals. *ACS Nano* **2017**, *11*, 8401-8412.

(27) Ram Boppana, V. B.; Doren, D. J.; Lobo, R. F., Analysis of Ga Coordination Environment in Novel Spinel Zinc Gallium Oxy-nitride Photocatalysts. *Journal of Materials Chemistry* **2010**, *20*, 9787-9797.

(28) Martha, S.; Reddy, K. H.; Parida, K. M.; Satapathy, P. K., Enhanced photocatalytic activity over N-doped GaZn mixed oxide under visible light irradiation. *International Journal of Hydrogen Energy* **2012**, *37*, 115-124.

(29) Furube, A.; Maeda, K.; Domen, K., Transient absorption study on photogenerated carrier dynamics in visible light responsive photocatalysts GaN:ZnO. *Solar Hydrogen and Nanotechnology Vi* **2011**, *8109*.

(30) Nakagawa, T.; Sakaguchi, I.; Uematsu, M.; Sato, Y.; Ohashi, N.; Haneda, H.; Ikuhara, Y., Diffusion Model of Gallium in Single-Crystal ZnO Proposed from Analysis of Concentration-Dependent Profiles Based on the Fermi-Level Effect. *Jpn J Appl Phys 1* **2007**, *46*, 4099-4101.

(31) Moore, W. J.; Williams, E. L., Diffusion of Zinc and Oxygen in Zinc Oxide. *Discuss Faraday Soc* **1959**, *28*, 86-93.

(32) Erhart, P.; Albe, K., Diffusion of Zinc Vacancies and Interstitials in Zinc Oxide. *Applied Physics Letters* **2006**, *88*, 201918.

(33) White, A. H.; Melville, W., The Decomposition of Ammonia at High Temperatures. *Journal of the American Chemical Society* **1905**, *27*, 373-386.

(34) Hisatomi, T.; Maeda, K.; Lu, D.; Domen, K., The Effects of Starting Materials in the Synthesis of $(Ga_{1-x}Zn_x)(N_{1-x}O_x)$ Solid Solution on Its Photocatalytic Activity for Overall Water Splitting under Visible Light. *ChemSusChem* **2009**, *2*, 336-343.

(35) Maeda, K.; Teramura, K.; Saito, N.; Inoue, Y.; Domen, K., Improvement of Photocatalytic Activity of $(Ga_{1-x}Zn_x)(N_{1-x}O_x)$ Solid Solution for Overall Water Splitting by Co-loading Cr and Another Transition Metal. *Journal of Catalysis* **2006**, *243*, 303-308.

(36) Maeda, K.; Teramura, K.; Masuda, H.; Takata, T.; Saito, N.; Inoue, Y.; Domen, K., Efficient Overall Water Splitting under Visible-Light Irradiation on $(Ga_{1-x}Zn_x)(N_{1-x}O_x)$ Dispersed with Rh−Cr Mixed-Oxide Nanoparticles: Effect of Reaction Conditions on Photocatalytic Activity. *Journal of Physical Chemistry B* **2006**, *110*, 13107-13112.

(37) Chen, H.; Wen, W.; Wang, Q.; Hanson, J. C.; Muckerman, J. T.; Fujita, E.; Frenkel, A. I.; Rodriguez, J. A., Preparation of $(Ga_{1-x}Zn_x)(N_{1-x}O_x)$ Photocatalysts from the Reaction of NH_3 with Ga_2O_3/ZnO and $ZnGa_2O_4$: *In Situ* Time-Resolved XRD and XAFS Studies. *Journal of Physical Chemistry C* **2009**, *113*, 3650-3659.

(38) Hisatomi, T.; Maeda, K.; Takanabe, K.; Kubota, J.; Domen, K., Aspects of the Water Splitting Mechanism on $(Ga_{1-x}Zn_x)(N_{1-x}O_x)$ Photocatalyst Modified with $Rh_{2-y}Cr_yO_3$ Cocatalyst. *The Journal of Physical Chemistry C* **2009**, *113*, 21458-21466.

(39) Maeda, K.; Hashiguchi, H.; Masuda, H.; Abe, R.; Domen, K., Photocatalytic Activity of $(Ga_{1-x}Zn_x)(N_{1-x}O_x)$ for Visible-Light-Driven H_2 and O_2 Evolution in the Presence of Sacrificial Reagents. *Journal of Physical Chemistry C* **2008**, *112*, 3447-3452.

(40) McDermott, E. J.; Kurmaev, E. Z.; Boyko, T. D.; Finkelstein, L. D.; Green, R. J.; Maeda, K.; Domen, K.; Moewes, A., Structural and Band Gap Investigation of GaN:ZnO Heterojunction Solid Solution Photocatalyst Probed by Soft X-ray Spectroscopy. *The Journal of Physical Chemistry C* **2012**, *116*, 7694-7700.

(41) Dharmagunawardhane, H. A. N.; James, A.; Wu, Q.; Woerner, W. R.; Palomino, R. M.; Sinclair, A.; Orlov, A.; Parise, J. B., Unexpected visible light driven photocatalytic activity without cocatalysts and sacrificial reagents from a $(GaN)_{1-x}(ZnO)_x$ solid solution synthesized at high pressure over the entire composition range. *RSC Advances* **2018**, *8*, 8976-8982.

(42) Maeda, K.; Domen, K., Solid Solution of GaN and ZnO as a Stable Photocatalyst for Overall Water Splitting under Visible Light. *Chemistry of Materials* **2010**, *22*, 612-623.

(43) Liu, B.; Bando, Y.; Liu, L.; Zhao, J.; Masanori, M.; Jiang, X.; Golberg, D., Solid–Solution Semiconductor Nanowires in Pseudobinary Systems. *Nano Letters* **2013**, *13*, 85-90.

(44) Yang, M.; Huang, Q.; Jin, X., Microwave synthesis of porous ZnGaNO solid solution for improved visible light photocatalytic performance. *Solid State Sciences* **2012**, *14*, 465-470.

(45) Dileep, K.; Loukya, B.; Pachauri, N.; Gupta, A.; Datta, R., Probing optical band gaps at the nanoscale in $NiFe_2O_4$ and $CoFe_2O_4$ epitaxial films by high resolution electron energy loss spectroscopy. *Journal of Applied Physics* **2014**, *116*, 103505.

(46) Jung, H. J.; Dasgupta, N. P.; Van Stockum, P. B.; Koh, A. L.; Sinclair, R.; Prinz, F. B., Spatial Variation of Available Electronic Excitations within Individual Quantum Dots. *Nano Letters* **2013**, *13*, 716-721.

(47) Egerton, R. F., Electron energy-loss spectroscopy in the TEM. *Reports on Progress in Physics* **2009**, *72*, 016502.

(48) Hachtel, J. A.; Lupini, A. R.; Idrobo, J. C., Exploring the capabilities of monochromated electron energy loss spectroscopy in the infrared regime. *Scientific Reports* **2018**, *8*, 5637.

(49) Zhan, W.; Venkatachalapathy, V.; Aarholt, T.; Kuznetsov, A. Y.; Prytz, Ø., Band gap maps beyond the delocalization limit: correlation between optical band gaps and plasmon energies at the nanoscale. *Scientific Reports* **2018**, *8*, 848.

(50) Crozier, P. A., Vibrational and valence aloof beam EELS: A potential tool for nondestructive characterization of nanoparticle surfaces. *Ultramicroscopy* **2017**, *180*, 104-114.

(51) Erni, R.; Browning, N. D., Quantification of the size-dependent energy gap of individual CdSe quantum dots by valence electron energy-loss spectroscopy. *Ultramicroscopy* **2007**, *107*, 267-273.

(52) Park, J.; Heo, S.; Chung, J.-G.; Kim, H.; Lee, H.; Kim, K.; Park, G.-S., Bandgap measurement of thin dielectric films using monochromated STEM-EELS. *Ultramicroscopy* **2009**, *109*, 1183-1188.

(53) Deitz, J. I.; Karki, S.; Marsillac, S. X.; Grassman, T. J.; McComb, D. W., Bandgap profiling in CIGS solar cells via valence electron energy-loss spectroscopy. *Journal of Applied Physics* **2018**, *123*, 115703.

(54) Gu, L.; Srot, V.; Sigle, W.; Koch, C.; van Aken, P.; Scholz, F.; Thapa, S. B.; Kirchner, C.; Jetter, M.; Rühle, M., Band-gap measurements of direct and indirect semiconductors using monochromated electrons. *Physical Review B* **2007**, *75*, 195214.

(55) Erni, R., On the validity of the Čerenkov limit as a criterion for precise band gap measurements by VEELS. *Ultramicroscopy* **2016**, *160*, 80-83.

(56) Lazar, S.; Botton, G. A.; Wu, M. Y.; Tichelaar, F. D.; Zandbergen, H. W., Materials science applications of HREELS in near edge structure analysis and low-energy loss spectroscopy. *Ultramicroscopy* **2003**, *96*, 535-546.

(57) Schamm, S.; Zanchi, G., Study of the dielectric properties near the band gap by VEELS: gap measurement in bulk materials. *Ultramicroscopy* **2003**, *96*, 559-564.

(58) Rez, P.; Aoki, T.; March, K.; Gur, D.; Krivanek, O. L.; Dellby, N.; Lovejoy, T. C.; Wolf, S. G.; Cohen, H., Damage-free vibrational spectroscopy of biological materials in the electron microscope. *Nature Communications* **2016**, *7*, 10945.

(59) Lazar, S.; Botton, G. A.; Zandbergen, H. W., Enhancement of resolution in core-loss and low-loss spectroscopy in a monochromated microscope. *Ultramicroscopy* **2006**, *106*, 1091-1103.

(60) Zhang, X.; Qin, J.; Xue, Y.; Yu, P.; Zhang, B.; Wang, L.; Liu, R., Effect of aspect ratio and surface defects on the photocatalytic activity of ZnO nanorods. *Scientific Reports* **2014**, *4*, 4596.

(61) Reynolds, D. C.; Look, D. C.; Jogai, B.; Hoelscher, J. E.; Sherriff, R. E.; Harris, M. T.; Callahan, M. J., Time-resolved photoluminescence lifetime measurements of the Γ5 and Γ6 free excitons in ZnO. *Journal of Applied Physics* **2000**, *88*, 2152-2153.

(62) Kamarulzaman, N.; Kasim, M. F.; Rusdi, R., Band Gap Narrowing and Widening of ZnO Nanostructures and Doped Materials. *Nanoscale Research Letters* **2015**, *10*, 346.

(63) Debanath, M. K.; Karmakar, S., Study of blueshift of optical band gap in zinc oxide (ZnO) nanoparticles prepared by low-temperature wet chemical method. *Materials Letters* **2013**, *111*, 116-119.

(64) Arakha, M.; Roy, J.; Nayak, P. S.; Mallick, B.; Jha, S., Zinc oxide nanoparticle energy band gap reduction triggers the oxidative stress resulting into autophagy-mediated apoptotic cell death. *Free Radical Biology and Medicine* **2017**, *110*, 42-53.

(65) Zhan, W.; Granerød, C. S.; Venkatachalapathy, V.; Johansen, K. M. H.; Jensen, I. J. T.; Kuznetsov, A. Y.; Ø, P., Nanoscale mapping of optical band gaps using monochromated electron energy loss spectroscopy. *Nanotechnology* **2017**, *28*, 105703.

(66) Lee, Y.-C.; Lin, T.-Y.; Wu, C.-W.; Teng, H.; Hu, C.-C.; Hu, S.-Y.; Yang, M.-D., Visible luminescence properties of $(Ga_{1-x}Zn_x)(N_{1-x}O_x)$ solid solution ($x = 0.22$). *Journal of Applied Physics* **2011**, *109*, 073506.

(67) Chen, H.; Wang, L.; Bai, J.; Hanson, J. C.; Warren, J. B.; Muckerman, J. T.; Fujita, E.; Rodriguez, J. A., *In Situ* XRD Studies of ZnO/GaN Mixtures at High Pressure and High Temperature: Synthesis of Zn-Rich $(Ga_{1-x}Zn_x)(N_{1-x}O_x)$ Photocatalysts. *Journal of Physical Chemistry C* **2010**, *114*, 1809-1814.

Chapter 5: Conclusions and Outlook

Chapter 2 discussed the synthesis and surface functionalization of $(Ga_{1-x}Zn_x)(N_{1-x}O_x)$ nanocrystals, emphasizing the solid-state synthesis mechanism involving topotactic nucleation and the lack of surface OH groups leading to mostly unsuccessful surface functionalization attempts. It was found that the size and shape of the final $(Ga_{1-x}Zn_x)(N_{1-x}O_x)$ nanocrystal product is independent of the ZnO precursor size and shape, but that the synthesis temperature will change the elemental distribution in the final product. When the synthesis is performed at 650 °C, a heterogeneous "core/shell" like distribution results, with the $(Ga_{1-x}Zn_x)(N_{1-x}O_x)$ mostly towards the edges of the particle and ZnO in the center of the particle. Conversely, when the synthesis is done at 800 °C, a homogeneous product is produced with all four elements evenly distributed throughout the particle. It was hypothesized that the surface of $(Ga_{1-x}Zn_x)(N_{1-x}O_x)$ nanocrystals may have both OH and NH groups, leading to only semi-successful silanizations and other unsuccessful functionalizations. This hypothesis came from the lack of success with attaching ligands that were supposed to react with or attach to OH sites on the surface.

Chapter 3 introduced a new H_2 production system using $(Ga_{1-x}Zn_x)(N_{1-x}O_x)$ nanocrystals as a light absorber, methyl viologen as a redox mediator, Pt nanoparticles as a cocatalyst, and dithioerythritol as a hole scavenger. This system successfully produced H_2 when irradiated with a 447 nm diode laser. However, the efficiency of the system was very low, at least two orders of magnitude lower than other $(Ga_{1-x}Zn_x)(N_{1-x}O_x)$ H_2 production systems and other redox mediator H_2 production systems. The low efficiency was proposed to be due to poorly aligned band potentials between the conduction band of the $(Ga_{1-x}Zn_x)(N_{1-x}O_x)$ and the redox potential of the methyl viologen. It is possible that the conduction band of the $(Ga_{1-x}Zn_x)(N_{1-x}O_x)$ could be more positive than the redox potential of methyl viologen, necessitating a buildup of electrons in the $(Ga_{1-x}Zn_x)(N_{1-x}O_x)$ conduction band to overcome the barrier of electron transfer to methyl viologen. On the contrary, it was found that electron transfer from methyl viologen to the Pt nanoparticles was fast and efficient, leading to the conclusion that it was not limiting the efficiency of the overall system.

Chapter 4 discusses results from using electron energy loss spectroscopy to study the spatially-resolved electronic band structure of $(Ga_{1-x}Zn_x)(N_{1-x}O_x)$ nanocrystals. One major conclusion from the study was that the electronic spectrum qualitatively matches the optical absorbance spectrum, indicating that an ensemble measurement is reflecting the same qualities as a single particle measurement. This is especially significant for the samples synthesized at 650 °C because they are a mixture of nitrided zinc gallate particles that did not topotactically nucleate with ZnO and regular $(Ga_{1-x}Zn_x)(N_{1-x}O_x)$ nanocrystals. Therefore, it was always a question whether or not the ensemble optical measurements were a result of the two types of particles mixing together. The electron energy loss spectroscopy measurements show that the single particle electronic band structure and the ensemble optical measurement match, indicating that the ensemble optical measurement accurately reflects the single particle electronic band structure. Another conclusion from the study was that the energy loss spectrum, and therefore the electronic band structure, of the $(Ga_{1-x}Zn_x)(N_{1-x}O_x)$ nanocrystals was qualitatively the same shape no matter where in the particle the spectrum was taken. This means that whether or not the particles have a homogeneous or heterogeneous elemental distribution, the electronic band structure will be the same throughout the particle. Therefore, in the heterogeneous “core/shell” like particles, this means that the electronic band structure is not different in the center of the particle versus the edge.

In order to study $(Ga_{1-x}Zn_x)(N_{1-x}O_x)$ nanocrystals further, alternative synthesis techniques should be employed so that the size and shape of the $(Ga_{1-x}Zn_x)(N_{1-x}O_x)$ product can be controlled. Solution-phase synthesis would be particularly useful because not only would it potentially allow for more control over the product size and shape, but the product could be synthesized with native ligands, negating the need to figure out how to functionalize the surface of $(Ga_{1-x}Zn_x)(N_{1-x}O_x)$ nanocrystals. If a synthesis technique with native ligands is not found, further surface functionalization efforts should be made, particularly to hydroxylate the surface of the $(Ga_{1-x}Zn_{x-})(N_{1-x}O_x)$ nanocrystals so that ligands can more successfully be attached. Alternatively, one could find ligands that would react with both OH and NH groups. Functionalizing the surface of $(Ga_{1-x}Zn_x)(N_{1-x}O_x)$ would allow for solution-phase measurements to be made and for less interference in H_2 production measurements, which are currently done as a powder slurry.

The next step for H_2 production studies would be to test H_2 production using $(Ga_{1-x}Zn_x)(N_{1-x}O_x)$ nanocrystals with Pt directly photodeposited on the surface. The procedure for Pt photodeposition is described in Chapter 2. This would remove the electron transfer step from $(Ga_{1-x}Zn_x)(N_{1-x}O_x)$ to methyl viologen, thus eliminating the rate limiting step in the redox mediator system discussed in Chapter 3. If H_2 production with the photodeposited Pt is successful, other cocatalysts could be investigated, particularly ones that contain an extra shell material that suppresses the backreaction of H_2 to H_2O.

Lastly, further electron energy loss spectroscopy studies can be done on the entire range of x-values of $(Ga_{1-x}Zn_x)(N_{1-x}O_x)$ nanocrystals with core-loss and low-loss data being collected at the same point for each sample. This would allow an elemental map to be generated to show the elemental composition at the exact spot where the bandgap measurements were also taken. With this, the changes in elemental composition to be more strongly linked to changes in the energy loss spectrum to shed light on the intricacies of the $(Ga_{1-x}Zn_x)(N_{1-x}O_x)$ band structure. Learning more about the band structure of $(Ga_{1-x}Zn_x)(N_{1-x}O_x)$ will inform further investigations into solid state synthesis of multinary materials, with the hopes of creating an ideal material for solar fuel generation.

Bibliography

Lewis, N. S.; Nocera, D. G., Powering the planet: Chemical challenges in solar energy utilization. *Proceedings of the National Academy of Sciences of the United States of America* **2006,** *103* (43), 15729-15735.

Walter, M. G.; Warren, E. L.; McKone, J. R.; Boettcher, S. W.; Mi, Q. X.; Santori, E. A.; Lewis, N. S., Solar Water Splitting Cells. *Chemical Reviews* **2010,** *110* (11), 6446-6473.

Kudo, A.; Miseki, Y., Heterogeneous Photocatalyst Materials for Water Splitting. *Chemical Society Reviews* **2009,** *38* (1), 253-278.

Maeda, K.; Domen, K., Photocatalytic Water Splitting: Recent Progress and Future Challenges. *Journal of Physical Chemistry Letters* **2010,** *1* (18), 2655-2661.

Zhou, M.; Bao, J.; Xu, Y.; Zhang, J.; Xie, J.; Guan, M.; Wang, C.; Wen, L.; Lei, Y.; Xie, Y., Photoelectrodes Based upon Mo:BiVO4 Inverse Opals for Photoelectrochemical Water Splitting. *ACS Nano* **2014,** *8* (7), 7088-7098.

Zhang, G.; Zhang, W.; Minakata, D.; Chen, Y.; C. Crittenden, J.; Wang, P., The pH effects on H2 evolution kinetics for visible light water splitting over the Ru/(CuAg)0.15In0.3Zn1.4S2 photocatalyst. *International Journal of Hydrogen Energy* **2013,** *38*, 11727-11736.

Sivula, K.; Zboril, R.; Le Formal, F.; Robert, R.; Weidenkaff, A.; Tucek, J.; Frydrych, J.; Grätzel, M., Photoelectrochemical Water Splitting with Mesoporous Hematite Prepared by a Solution-Based Colloidal Approach. *Journal of the American Chemical Society* **2010,** *132* (21), 7436-7444.

Sabio, E. M.; Chamousis, R. L.; Browning, N. D.; Osterloh, F. E., Photocatalytic Water Splitting with Suspended Calcium Niobium Oxides: Why Nanoscale is Better than Bulk – A Kinetic Analysis. *Journal of Physical Chemistry C* **2012,** *116* (4), 3161-3170.

Maeda, K.; Teramura, K.; Takata, T.; Hara, M.; Saito, N.; Toda, K.; Inoue, Y.; Kobayashi, H.; Domen, K., Overall Water Splitting on $(\mathrm{Ga}_{1-x}\mathrm{Zn}_{x})(\mathrm{N}_{1-x}\mathrm{O}_{x})$ Solid Solution Photocatalyst: Relationship between Physical Properties and Photocatalytic Activity. *Journal of Physical Chemistry B* **2005,** *109* (43), 20504-20510.

Maeda, K.; Ohno, T.; Domen, K., A copper and chromium based nanoparticulate oxide as a noble-metal-free cocatalyst for photocatalytic water splitting. *Chemical Science* **2011,** *2* (7), 1362-1368.

Li, Y.; Takata, T.; Cha, D.; Takanabe, K.; Minegishi, T.; Kubota, J.; Domen, K., Vertically Aligned Ta3N5 Nanorod Arrays for Solar-Driven Photoelectrochemical Water Splitting. *Advanced Materials* **2013,** *25* (1), 125-131.

Kumagai, N.; Ni, L.; Irie, H., A visible-light-sensitive water splitting photocatalyst composed of Rh3+ in a 4d6 electronic configuration, Rh3+-doped ZnGa2O4. *Chemical Communications* **2011,** *47* (6), 1884-1886.

Ikeda, T.; Xiong, A.; Yoshinaga, T.; Maeda, K.; Domen, K.; Teranishi, T., Polyol Synthesis of Size-Controlled Rh Nanoparticles and Their Application to Photocatalytic Overall Water Splitting under Visible Light. *Journal of Physical Chemistry C* **2013,** *117* (6), 2467-2473.

Berto, T. F.; Sanwald, K. E.; Byers, J. P.; Browning, N. D.; Gutiérrez, O. Y.; Lercher, J. A., Enabling Overall Water Splitting on Photocatalysts by CO-Covered Noble Metal Co-catalysts. *The Journal of Physical Chemistry Letters* **2016,** *7* (21), 4358-4362.

Adeli, B.; Taghipour, F., Reduced Graphene Oxide Composite of Gallium Zinc Oxynitride Photocatalyst with Improved Activity for Overall Water Splitting. *Chemical Engineering & Technology* **2016,** *39* (1), 142-148.

Maeda, K.; Takata, T.; Hara, M.; Saito, N.; Inoue, Y.; Kobayashi, H.; Domen, K., GaN:ZnO Solid Solution as a Photocatalyst for Visible-Light-Driven Overall Water Splitting. *Journal of the American Chemical Society* **2005,** *127* (23), 8286-8287.

Xie, R.-J.; Hintzen, H. T., Optical Properties of (Oxy)Nitride Materials: A Review. *Journal of the American Ceramic Society* **2013,** *96* (3), 665-687.

Li, X.; Zhang, Q.; Wang, H.; Li, Y., Synthesis of Mesoporous (Ga1−xZnx)(N1−xOx) Using Layered Double Hydroxides as Precursors for Enhanced Visible-Light Driven H2 Production. *Chinese Journal of Chemistry* **2017,** *35* (2), 196-202.

Lee, K.; Tienes, B. M.; Wilker, M. B.; Schnitzenbaumer, K. J.; Dukovic, G., $(Ga_{1-x}Zn_x)(N_{1-x}O_x)$ Nanocrystals: Visible Absorbers with Tunable Composition and Absorption Spectra. *Nano Letters* **2012,** *12* (6), 3268-3272.

Wang, J.; Huang, B.; Wang, Z.; Wang, P.; Cheng, H.; Zheng, Z.; Qin, X.; Zhang, X.; Dai, Y.; Whangbo, M.-H., Facile Synthesis of Zn-rich $(GaN)_{1-x}(ZnO)_x$ Solid Solutions Using Layered Double Hydroxides as Precursors. *Journal of Materials Chemistry* **2011,** *21* (12), 4562-4567.

Ren, B.; Zhang, X.; Zhao, M.; Wang, X.; Ye, J.; Wang, D., Significant enhancement in photocatalytic activity of (GaN)1−x(ZnO)x nanowires via solubility and crystal facet tailoring. *AIP Advances* **2018,** *8* (1), 015206.

RajaAmbal, S.; Yadav, A. K.; Jha, S. N.; Bhattacharyya, D.; Gopinath, C. S., Electronic structure-sunlight driven water splitting activity correlation of (Zn1-yGay)(O1-zNz). *Physical Chemistry Chemical Physics* **2014,** *16* (43), 23654-23662.

Martha, S.; Reddy, K. H.; Parida, K. M.; Satapathy, P. K., Enhanced photocatalytic activity over N-doped GaZn mixed oxide under visible light irradiation. *International Journal of Hydrogen Energy* **2012,** *37* (1), 115-124.

Hisatomi, T.; Maeda, K.; Lu, D.; Domen, K., The Effects of Starting Materials in the Synthesis of $(Ga_{1-x}Zn_x)(N_{1-x}O_x)$ Solid Solution on Its Photocatalytic Activity for Overall Water Splitting under Visible Light. *ChemSusChem* **2009,** *2* (4), 336-343.

Han, W.-Q.; Liu, Z.; Yu, H.-G., Synthesis and Optical Properties of GaN/ZnO Solid Solution Nanocrystals. *Applied Physics Letters* **2010,** *96* (18), 183112.

Hahn, C.; Fardy, M. A.; Nguyen, C.; Natera-Comte, M.; Andrews, S. C.; Yang, P. D., Synthesis and Photocatalytic Properties of Single Crystalline (Ga1-xZnx)(N1-xOx) Nanotubes. *Israel Journal of Chemistry* **2012,** *52* (11-12), 1111-1117.

Dharmagunawardhane, H. A. N.; James, A.; Wu, Q.; Woerner, W. R.; Palomino, R. M.; Sinclair, A.; Orlov, A.; Parise, J. B., Unexpected visible light driven photocatalytic activity without cocatalysts and sacrificial reagents from a (GaN)1–x(ZnO)x solid solution synthesized at high pressure over the entire composition range. *RSC Advances* **2018,** *8* (16), 8976-8982.

Chen, H.; Wen, W.; Wang, Q.; Hanson, J. C.; Muckerman, J. T.; Fujita, E.; Frenkel, A. I.; Rodriguez, J. A., Preparation of $(Ga_{1-x}Zn_x)(N_{1-x}O_x)$ Photocatalysts from the Reaction of NH_3 with Ga_2O_3/ZnO and $ZnGa_2O_4$: *In Situ* Time-Resolved XRD and XAFS Studies. *Journal of Physical Chemistry C* **2009,** *113* (9), 3650-3659.

Adeli, B.; Taghipour, F., A Review of Synthesis Techniques for Gallium-Zinc Oxynitride Solar-Activated Photocatalyst for Water Splitting. *ECS J. Solid State Sci. Technol.* **2013,** *2* (7), Q118-Q126.

Maeda, K.; Teramura, K.; Masuda, H.; Takata, T.; Saito, N.; Inoue, Y.; Domen, K., Efficient Overall Water Splitting under Visible-Light Irradiation on $(Ga_{1-x}Zn_x)(N_{1-x}O_x)$ Dispersed with Rh−Cr Mixed-Oxide Nanoparticles: Effect of Reaction Conditions on Photocatalytic Activity. *Journal of Physical Chemistry B* **2006,** *110* (26), 13107-13112.

Maeda, K.; Teramura, K.; Domen, K., Development of Cocatalysts for Photocatalytic Overall Water Splitting on (Ga1−xZnx)(N1−xOx) Solid Solution. *Catalysis Surveys from Asia* **2007,** *11* (4), 145-157.

Maeda, K.; Hashiguchi, H.; Masuda, H.; Abe, R.; Domen, K., Photocatalytic Activity of $(Ga_{1-x}Zn_x)(N_{1-x}O_x)$ for Visible-Light-Driven H_2 and O_2 Evolution in the Presence of Sacrificial Reagents. *Journal of Physical Chemistry C* **2008,** *112* (9), 3447-3452.

Maeda, K.; Teramura, K.; Domen, K., Effect of Post-Calcination on Photocatalytic Activity of $(Ga_{1-x}Zn_x)(N_{1-x}O_x)$ Solid Solution for Overall Water Splitting under Visible Light. *Journal of Catalysis* **2008,** *254* (2), 198-204.

Hisatomi, T.; Maeda, K.; Takanabe, K.; Kubota, J.; Domen, K., Aspects of the Water Splitting Mechanism on $(Ga_{1-x}Zn_x)(N_{1-x}O_x)$ Photocatalyst Modified with $Rh_{2-y}Cr_yO_3$ Cocatalyst. *The Journal of Physical Chemistry C* **2009,** *113* (51), 21458-21466.

Maeda, K.; Domen, K., Solid Solution of GaN and ZnO as a Stable Photocatalyst for Overall Water Splitting under Visible Light. *Chemistry of Materials* **2010,** *22* (3), 612-623.

Xiong, A.; Yoshinaga, T.; Ikeda, T.; Takashima, M.; Hisatomi, T.; Maeda, K.; Setoyama, T.; Teranishi, T.; Domen, K., Effect of Hydrogen and Oxygen Evolution Cocatalysts on Photocatalytic Activity of GaN:ZnO. *European Journal of Inorganic Chemistry* **2014,** *2014* (4), 767-772.

Menon, S. S.; Kuppulingam, B.; Baskar, K.; Sairam, T. N.; Ravindran, T. R.; Gupta, B.; Singh, S., Realization of high photocatalytic hydrogen generation activity by nanostructured Ga1−xZnxO1−zNz solid-solution without co-catalyst. *International Journal of Hydrogen Energy* **2015,** *40* (40), 13901-13908.

Zhou, Y.; Chen, G.; Yu, Y.; Zhao, L.; Yu, Q.; He, Q., Effects of La-doping on charge separation behavior of ZnO:GaN for its enhanced photocatalytic performance. *Catalysis Science & Technology* **2016,** *6* (4), 1033-1041.

Maeda, K.; Teramura, K.; Saito, N.; Inoue, Y.; Domen, K., Improvement of Photocatalytic Activity of $(Ga_{1-x}Zn_x)(N_{1-x}O_x)$ Solid Solution for Overall Water Splitting by Co-loading Cr and Another Transition Metal. *Journal of Catalysis* **2006,** *243* (2), 303-308.

Hirai, T.; Maeda, K.; Yoshida, M.; Kubota, J.; Ikeda, S.; Matsumura, M.; Domen, K., Origin of Visible Light Absorption in GaN-Rich (Ga1-xZnx)(N1-xOx) Photocatalysts. *Journal of Physical Chemistry C* **2007,** *111* (51), 18853-18855.

Maeda, K.; Domen, K., New Non-Oxide Photocatalysts Designed for Overall Water Splitting under Visible Light. *Journal of Physical Chemistry C* **2007,** *111* (22), 7851-7861.

Li, Y.; Zhu, L.; Yang, Y.; Song, H.; Lou, Z.; Guo, Y.; Ye, Z., A Full Compositional Range for a $(Ga_{1-x}Zn_x)(N_{1-x}O_x)$ Nanostructure: High Efficiency for Overall Water Splitting and Optical Properties. *Small* **2015,** *11* (7), 871-876.

Tongying, P.; Lu, Y.-G.; Hall, L. M. G.; Lee, K.; Sulima, M.; Ciston, J.; Dukovic, G., Control of Elemental Distribution in the Nanoscale Solid-State Reaction That Produces (Ga1–xZnx)(N1–xOx) Nanocrystals. *ACS Nano* **2017,** *11* (8), 8401-8412.

Zhu, H.; Song, N.; Lv, H.; Hill, C. L.; Lian, T., Near Unity Quantum Yield of Light-Driven Redox Mediator Reduction and Efficient H_2 Generation Using Colloidal Nanorod Heterostructures. *Journal of the American Chemical Society* **2012,** *134* (28), 11701-11708.

Miller, D. S.; Bard, A. J.; McLendon, G.; Ferguson, J., Catalytic water reduction at colloidal metal "microelectrodes". 2. Theory and experiment. *Journal of the American Chemical Society* **1981,** *103* (18), 5336-5341.

Pellegrino, F.; Sordello, F.; Minella, M.; Minero, C.; Maurino, V., The Role of Surface Texture on the Photocatalytic H2 Production on TiO2. *Catalysts* **2019,** *9* (1).

Yan, S. G.; Lyon, L. A.; Lemon, B. I.; Preiskorn, J. S.; Hupp, J. T., Energy Conversion Chemistry: Mechanisms of Charge Transfer at Metal-Oxide Semiconductor/Solution Interfaces. *Journal of Chemical Education* **1997,** *74* (6), 657.

She, C.; Anderson, N. A.; Guo, J.; Liu, F.; Goh, W.-H.; Chen, D.-T.; Mohler, D. L.; Tian, Z.-Q.; Hupp, J. T.; Lian, T., pH-Dependent Electron Transfer from Re-bipyridyl Complexes to Metal Oxide Nanocrystalline Thin Films. *The Journal of Physical Chemistry B* **2005,** *109* (41), 19345-19355.

Lyon, L. A.; Hupp, J. T., Energetics of the Nanocrystalline Titanium Dioxide/Aqueous Solution Interface: Approximate Conduction Band Edge Variations between H0 = −10 and H- = +26. *The Journal of Physical Chemistry B* **1999,** *103* (22), 4623-4628.

Lemon, B. I.; Liu, F.; Hupp, J. T., Electrochemical, spectral, and quartz crystal microgravimetric assessment of conduction band edge energies for nanocrystalline zirconium dioxide/solution interfaces. *Coordination Chemistry Reviews* **2004,** *248* (13), 1225-1230.

Zhang, J.; Yu, J.; Jaroniec, M.; Gong, J. R., Noble Metal-Free Reduced Graphene Oxide-ZnxCd1–xS Nanocomposite with Enhanced Solar Photocatalytic H2-Production Performance. *Nano Letters* **2012,** *12* (9), 4584-4589.

Van Dijk, C.; Veeger, C., The Effects of pH and Redox Potential on the Hydrogen Production Activity of the Hydrogenase from Megasphaera elsdenii. *European Journal of Biochemistry* **1981,** *114* (2), 209-219.

Li, Q.; Meng, H.; Zhou, P.; Zheng, Y.; Wang, J.; Yu, J.; Gong, J., Zn1–xCdxS Solid Solutions with Controlled Bandgap and Enhanced Visible-Light Photocatalytic H2-Production Activity. *ACS Catalysis* **2013,** *3* (5), 882-889.

Li, Q.; Guo, B.; Yu, J.; Ran, J.; Zhang, B.; Yan, H.; Gong, J. R., Highly Efficient Visible-Light-Driven Photocatalytic Hydrogen Production of CdS-Cluster-Decorated Graphene Nanosheets. *Journal of the American Chemical Society* **2011,** *133* (28), 10878-10884.

Cleland, W. W., Dithiothreitol, a New Protective Reagent for SH Groups*. *Biochemistry* **1964,** *3* (4), 480-482.

Yoshida, M.; Yamakata, A.; Takanabe, K.; Kubota, J.; Osawa, M.; Domen, K., ATR-SEIRAS Investigation of the Fermi Level of Pt Cocatalyst on a GaN Photocatalyst for Hydrogen Evolution under Irradiation. *Journal of the American Chemical Society* **2009,** *131* (37), 13218-13219.

Scanlon, M. D.; Peljo, P.; Méndez, M. A.; Smirnov, E.; Girault, H. H., Charging and discharging at the nanoscale: Fermi level equilibration of metallic nanoparticles. *Chemical Science* **2015,** *6* (5), 2705-2720.

Hachtel, J. A.; Lupini, A. R.; Idrobo, J. C., Exploring the capabilities of monochromated electron energy loss spectroscopy in the infrared regime. *Scientific Reports* **2018,** *8* (1), 5637.

Egerton, R. F., Electron energy-loss spectroscopy in the TEM. *Reports on Progress in Physics* **2009,** *72* (1), 016502.

Crozier, P. A., Vibrational and valence aloof beam EELS: A potential tool for nondestructive characterization of nanoparticle surfaces. *Ultramicroscopy* **2017,** *180*, 104-114.

Williams, D. B.; Carter, C. B., *Transmission Electron Microscopy*. Springer: New York, 1996.

Yoshida, M.; Hirai, T.; Maeda, K.; Saito, N.; Kubota, J.; Kobayashi, H.; Inoue, Y.; Domen, K., Photoluminescence Spectroscopic and Computational Investigation of the Origin of the Visible Light Response of (Ga1−xZnx)(N1−xOx) Photocatalyst for Overall Water Splitting. *The Journal of Physical Chemistry C* **2010,** *114* (36), 15510-15515.

Yang, M.; Huang, Q.; Jin, X., Microwave synthesis of porous ZnGaNO solid solution for improved visible light photocatalytic performance. *Solid State Sciences* **2012,** *14* (4), 465-470.

Liu, B.; Bando, Y.; Liu, L.; Zhao, J.; Masanori, M.; Jiang, X.; Golberg, D., Solid–Solution Semiconductor Nanowires in Pseudobinary Systems. *Nano Letters* **2013,** *13* (1), 85-90.

Kociak, M.; Zagonel, L. F., Cathodoluminescence in the scanning transmission electron microscope. *Ultramicroscopy* **2017,** *176*, 112-131.

Keast, V. J.; Bosman, M., New developments in electron energy loss spectroscopy. *Microscopy Research and Technique* **2007,** *70* (3), 211-219.

Maeda, K.; Teramura, K.; Lu, D.; Takata, T.; Saito, N.; Inoue, Y.; Domen, K., Characterization of Rh−Cr Mixed-Oxide Nanoparticles Dispersed on (Ga1-xZnx)(N1-xOx) as a Cocatalyst for Visible-Light-Driven Overall Water Splitting. *Journal of Physical Chemistry B* **2006,** *110* (28), 13753-13758.

Maeda, K.; Teramura, K.; Lu, D. L.; Takata, T.; Saito, N.; Inoue, Y.; Domen, K., Photocatalyst releasing hydrogen from water - Enhancing catalytic performance holds promise for hydrogen production by water splitting in sunlight. *Nature* **2006,** *440* (7082), 295-295.

Ford, G. M.; Guo, Q.; Agrawal, R.; Hillhouse, H. W., Earth Abundant Element Cu2Zn(Sn1−xGex)S4 Nanocrystals for Tunable Band Gap Solar Cells: 6.8% Efficient Device Fabrication. *Chemistry of Materials* **2011,** *23* (10), 2626-2629.

Fan, F.-J.; Wu, L.; Yu, S.-H., Energetic I–III–VI2 and I2–II–IV–VI4 nanocrystals: synthesis, photovoltaic and thermoelectric applications. *Energy & Environmental Science* **2014,** *7* (1), 190-208.

Wei, S.-Y.; Liao, Y.-C.; Hsu, C.-H.; Cai, C.-H.; Huang, W.-C.; Huang, M.-C.; Lai, C.-H., Achieving high efficiency Cu2ZnSn(S,Se)4 solar cells by non-toxic aqueous ink: Defect analysis and electrical modeling. *Nano Energy* **2016,** *26*, 74-82.

Chuang, C.-H.; Lu, Y.-G.; Lee, K.; Ciston, J.; Dukovic, G., Strong Visible Absorption and Broad Time Scale Excited-State Relaxation in (Ga1–xZnx)(N1–xOx) Nanocrystals. *Journal of the American Chemical Society* **2015,** *137* (20), 6452-6455.

Schwartz, D. A.; Norberg, N. S.; Nguyen, Q. P.; Parker, J. M.; Gamelin, D. R., Magnetic Quantum Dots: Synthesis, Spectroscopy, and Magnetism of Co2+- and Ni2+-Doped ZnO Nanocrystals. *Journal of the American Chemical Society* **2003,** *125* (43), 13205-13218.

Tienes, B. M.; Perkins, R. J.; Shoemaker, R. K.; Dukovic, G., Layered Phosphonates in Colloidal Synthesis of Anisotropic ZnO Nanocrystals. *Chemistry of Materials* **2013,** *25* (21), 4321-4329.

Saengdee, P.; Chaisriratanakul, W.; Bunjongpru, W.; Sripumkhai, W.; Srisuwan, A.; Jeamsaksiri, W.; Hruanun, C.; Poyai, A.; Promptmas, C., Surface modification of silicon dioxide, silicon nitride and titanium oxynitride for lactate dehydrogenase immobilization. *Biosensors and Bioelectronics* **2015,** *67*, 134-138.

Rabin Nurun, N.; Morshed, J.; Akhter, H.; Islam Md, S.; Hossain Md, A.; Elias, M.; Alam Md, M.; Karim, M. R.; Hasnat, M. A.; uddin Md, N.; Siddiquey Iqbal, A., Surface Modification of the ZnO Nanoparticles with γ-Aminopropyltriethoxysilane and Study of Their Photocatalytic Activity, Optical Properties and Antibacterial Activities. In *International Journal of Chemical Reactor Engineering*, 2016; Vol. 14, p 785.

Liu, Y.; Li, Y.; Li, X.-M.; He, T., Kinetics of (3-Aminopropyl)triethoxylsilane (APTES) Silanization of Superparamagnetic Iron Oxide Nanoparticles. *Langmuir* **2013,** *29* (49), 15275-15282.

Grasset, F.; Saito, N.; Li, D.; Park, D.; Sakaguchi, I.; Ohashi, N.; Haneda, H.; Roisnel, T.; Mornet, S.; Duguet, E., Surface modification of zinc oxide nanoparticles by aminopropyltriethoxysilane. *Journal of Alloys and Compounds* **2003,** *360* (1), 298-311.

Dong, A.; Ye, X.; Chen, J.; Kang, Y.; Gordon, T.; Kikkawa, J. M.; Murray, C. B., A Generalized Ligand-Exchange Strategy Enabling Sequential Surface Functionalization of Colloidal Nanocrystals. *Journal of the American Chemical Society* **2011,** *133* (4), 998-1006.

Yee, C.; Kataby, G.; Ulman, A.; Prozorov, T.; White, H.; King, A.; Rafailovich, M.; Sokolov, J.; Gedanken, A., Self-Assembled Monolayers of Alkanesulfonic and -phosphonic Acids on Amorphous Iron Oxide Nanoparticles. *Langmuir* **1999,** *15* (21), 7111-7115.

Carabineiro, S. A. C.; Machado, B. F.; Dražić, G.; Bacsa, R. R.; Serp, P.; Figueiredo, J. L.; Faria, J. L., Photodeposition of Au and Pt on ZnO and TiO2. In *Studies in Surface Science and Catalysis*, Gaigneaux, E. M.; Devillers, M.; Hermans, S.; Jacobs, P. A.; Martens, J. A.; Ruiz, P., Eds. Elsevier: 2010; Vol. 175, pp 629-633.

Cavalca, F.; Laursen, A. B.; Kardynal, B. E.; Dunin-Borkowski, R. E.; Dahl, S.; Wagner, J. B.; Hansen, T. W., In situtransmission electron microscopy of light-induced photocatalytic reactions. *Nanotechnology* **2012,** *23* (7), 075705.

Whittingham, M. S., Lithium Batteries and Cathode Materials. *Chemical Reviews* **2004,** *104* (10), 4271-4302.

Nozik, A. J.; Beard, M. C.; Luther, J. M.; Law, M.; Ellingson, R. J.; Johnson, J. C., Semiconductor Quantum Dots and Quantum Dot Arrays and Applications of Multiple Exciton Generation to Third-Generation Photovoltaic Solar Cells. *Chemical Reviews* **2010,** *110* (11), 6873-6890.

Regulacio, M. D.; Han, M.-Y., Multinary I-III-VI2 and I2-II-IV-VI4 Semiconductor Nanostructures for Photocatalytic Applications. *Accounts of Chemical Research* **2016,** *49* (3), 511-519.

Ohno, T.; Bai, L.; Hisatomi, T.; Maeda, K.; Domen, K., Photocatalytic Water Splitting Using Modified GaN:ZnO Solid Solution under Visible Light: Long-Time Operation and Regeneration of Activity. *Journal of the American Chemical Society* **2012,** *134* (19), 8254-8259.

Huda, M. N.; Yan, Y. F.; Wei, S. H.; Al-Jassim, M. M., Electronic structure of ZnO:GaN compounds: Asymmetric bandgap engineering. *Physical Review B* **2008,** *78* (19), 195204.

Jensen, L. L.; Muckerman, J. T.; Newton, M. D., First-Principles Studies of the Structural and Electronic Properties of the $(Ga_{1-x}Zn_x)(N_{1-x}O_x)$ Solid Solution Photocatalyst. *Journal of Physical Chemistry C* **2008,** *112* (9), 3439-3446.

Wei, W.; Dai, Y.; Yang, K. S.; Guo, M.; Huang, B. B., Origin of the visible light absorption of GaN-Rich $Ga_{1-x}Zn_xN_{1-x}O_x$ (x=0.125) solid solution. *Journal of Physical Chemistry C* **2008,** *112* (40), 15915-15919.

Chen, H.; Wang, L.; Bai, J.; Hanson, J. C.; Warren, J. B.; Muckerman, J. T.; Fujita, E.; Rodriguez, J. A., *In Situ* XRD Studies of ZnO/GaN Mixtures at High Pressure and High Temperature: Synthesis of Zn-Rich $(Ga_{1-x}Zn_x)(N_{1-x}O_x)$ Photocatalysts. *Journal of Physical Chemistry C* **2010,** *114* (4), 1809-1814.

Di Valentin, C., Electronic Structure of (Ga1−xZnx)N1−xOx Photocatalyst for Water Splitting by Hybrid Hartree-Fock Density Functional Theory Methods. *Journal of Physical Chemistry C* **2010,** *114* (15), 7054-7062.

Wang, S. Z.; Wang, L. W., Atomic and Electronic Structures of GaN/ZnO Alloys. *Physical Review Letters* **2010,** *104* (6), 065501.

Lee, Y.-C.; Lin, T.-Y.; Wu, C.-W.; Teng, H.; Hu, C.-C.; Hu, S.-Y.; Yang, M.-D., Visible luminescence properties of (Ga1−xZnx)(N1−xOx) solid solution (x = 0.22). *Journal of Applied Physics* **2011,** *109* (7), 073506.

Li, L.; Muckerman, J. T.; Hybertsen, M. S.; Allen, P. B., Phase Diagram, Structure, and Electronic Properties of $(\mathrm{Ga}_{1-x}\mathrm{Zn}_x)(\mathrm{N}_{1-x}\mathrm{O}_x)$ Solid Solutions from DFT-Based Simulations. *Physical Review B* **2011,** *83* (13), 134202.

Yu, H.-G., An optimal density functional theory method for GaN and ZnO. *Chemical Physics Letters* **2011,** *512* (4–6), 231-236.

Dou, M.; Persson, C., Band gap reduction and dielectric function of Ga1−xZnxN1−xOx and In1−xZnxN1−xOx alloys. *physica status solidi (a)* **2012,** *209* (1), 75-78.

McDermott, E. J.; Kurmaev, E. Z.; Boyko, T. D.; Finkelstein, L. D.; Green, R. J.; Maeda, K.; Domen, K.; Moewes, A., Structural and Band Gap Investigation of GaN:ZnO Heterojunction Solid Solution Photocatalyst Probed by Soft X-ray Spectroscopy. *Journal of Physical Chemistry C* **2012,** *116* (14), 7694-7700.

Shockley, W.; Queisser, H. J., Detailed Balance Limit of Efficiency of p-n Junction Solar Cells. *Journal of Applied Physics* **1961,** *32* (3), 510-519.

Godin, R.; Hisatomi, T.; Domen, K.; Durrant, J. R., Understanding the visible-light photocatalytic activity of GaN:ZnO solid solution: the role of Rh2−yCryO3 cocatalyst and charge carrier lifetimes over tens of seconds. *Chemical Science* **2018,** *9* (38), 7546-7555.

Li, Z.; Zhang, F.; Han, J.; Zhu, J.; Li, M.; Zhang, B.; Fan, W.; Lu, J.; Li, C., Using Pd as a Cocatalyst on GaN–ZnO Solid Solution for Visible-Light-Driven Overall Water Splitting. *Catalysis Letters* **2018,** *148* (3), 933-939.

Wang, Z.; Li, C.; Domen, K., Recent developments in heterogeneous photocatalysts for solar-driven overall water splitting. *Chemical Society Reviews* **2019**.

Wu, G.-W.; He, S.-B.; Peng, H.-P.; Deng, H.-H.; Liu, A.-L.; Lin, X.-H.; Xia, X.-H.; Chen, W., Citrate-Capped Platinum Nanoparticle as a Smart Probe for Ultrasensitive Mercury Sensing. *Analytical Chemistry* **2014,** *86* (21), 10955-10960.

Lee, K.; Lu, Y.-G.; Chuang, C.-H.; Ciston, J.; Dukovic, G., Synthesis and Characterization of $(\mathrm{Ga}_{1-x}\mathrm{Zn}_x)(\mathrm{N}_{1-x}\mathrm{O}_x)$ Nanocrystals with a Wide Range of Compositions. *Journal of Materials Chemistry A* **2016,** *4* (8), 2927-2935.

Mayhew, S. G.; Abels, R.; Platenkamp, R., The production of dithionite and SO2− by chemical reaction of (bi)sulphite with methyl viologen semiquinone. *Biochemical and Biophysical Research Communications* **1977,** *77* (4), 1397-1403.

Aharon-Shalom, E.; Heller, A., Efficient p - InP (Rh - H alloy) and p - InP (Re - H alloy) Hydrogen Evolving Photocathodes. *Journal of The Electrochemical Society* **1982,** *129* (12), 2865-2866.

Conway, B. E.; Tilak, B. V., Interfacial processes involving electrocatalytic evolution and oxidation of H2, and the role of chemisorbed H. *Electrochimica Acta* **2002,** *47* (22), 3571-3594.

Sun, X.; Maeda, K.; Le Faucheur, M.; Teramura, K.; Domen, K., Preparation of $(Ga_{1-x}Zn_x)(N_{1-x}O_x)$ Solid-Solution from $ZnGa_2O_4$ and ZnO as a Photo-Catalyst for Overall Water Splitting under Visible Light. *Appl Catal a-Gen* **2007,** *327* (1), 114-121.

Yoshida, M.; Maeda, K.; Lu, D.; Kubota, J.; Domen, K., Lanthanoid Oxide Layers on Rhodium-Loaded (Ga1–xZnx)(N1–xOx) Photocatalyst as a Modifier for Overall Water Splitting under Visible-Light Irradiation. *Journal of Physical Chemistry C* **2013,** *117* (27), 14000-14006.

Zhang, J.; Yu, J.; Zhang, Y.; Li, Q.; Gong, J. R., Visible Light Photocatalytic H2-Production Activity of CuS/ZnS Porous Nanosheets Based on Photoinduced Interfacial Charge Transfer. *Nano Letters* **2011,** *11* (11), 4774-4779.

Chica, B.; Wu, C.-H.; Liu, Y.; Adams, M. W. W.; Lian, T.; Dyer, R. B., Balancing electron transfer rate and driving force for efficient photocatalytic hydrogen production in CdSe/CdS nanorod–[NiFe] hydrogenase assemblies. *Energy & Environmental Science* **2017,** *10* (10), 2245-2255.

Zhao, F.; Li, Q.; Han, K.; Lian, T., Mechanism of Efficient Viologen Radical Generation by Ultrafast Electron Transfer from CdS Quantum Dots. *The Journal of Physical Chemistry C* **2018,** *122* (30), 17136-17142.

Hashiguchi, H.; Maeda, K.; Abe, R.; Ishikawa, A.; Kubota, J.; Domen, K., Photoresponse of GaN:ZnO Electrode on FTO under Visible Light Irradiation. *Bulletin of the Chemical Society of Japan* **2009,** *82* (3), 401-407.

Zhang, Y.; Wu, Z.-F.; Gao, P.-F.; Fang, D.-Q.; Zhang, S.-L., Enhanced visible light absorption in ZnO/GaN heterostructured nanofilms. *Journal of Alloys and Compounds* **2017,** *704*, 478-483.

Zhang, Y.; Fang, D.-Q.; Zhang, S.-L.; Huang, R.; Wen, Y.-H., Structural and electronic properties of ZnO/GaN heterostructured nanowires from first-principles study. *Physical Chemistry Chemical Physics* **2016,** *18* (4), 3097-3102.

Adeli, B.; Taghipour, F., Facile synthesis of highly efficient nano-structured gallium zinc oxynitride solid solution photocatalyst for visible-light overall water splitting. *Applied Catalysis A: General* **2016,** *521*, 250-258.

Ram Boppana, V. B.; Doren, D. J.; Lobo, R. F., Analysis of Ga Coordination Environment in Novel Spinel Zinc Gallium Oxy-nitride Photocatalysts. *Journal of Materials Chemistry* **2010,** *20* (43), 9787-9797.

Furube, A.; Maeda, K.; Domen, K., Transient absorption study on photogenerated carrier dynamics in visible light responsive photocatalysts GaN:ZnO. *Solar Hydrogen and Nanotechnology Vi* **2011,** *8109*.

Nakagawa, T.; Sakaguchi, I.; Uematsu, M.; Sato, Y.; Ohashi, N.; Haneda, H.; Ikuhara, Y., Diffusion Model of Gallium in Single-Crystal ZnO Proposed from Analysis of Concentration-Dependent Profiles Based on the Fermi-Level Effect. *Jpn J Appl Phys 1* **2007,** *46* (7A), 4099-4101.

Moore, W. J.; Williams, E. L., Diffusion of Zinc and Oxygen in Zinc Oxide. *Discuss Faraday Soc* **1959,** *28*, 86-93.

Erhart, P.; Albe, K., Diffusion of Zinc Vacancies and Interstitials in Zinc Oxide. *Applied Physics Letters* **2006,** *88* (20), 201918.

McDermott, E. J.; Kurmaev, E. Z.; Boyko, T. D.; Finkelstein, L. D.; Green, R. J.; Maeda, K.; Domen, K.; Moewes, A., Structural and Band Gap Investigation of GaN:ZnO Heterojunction Solid Solution Photocatalyst Probed by Soft X-ray Spectroscopy. *The Journal of Physical Chemistry C* **2012,** *116* (14), 7694-7700.

Dileep, K.; Loukya, B.; Pachauri, N.; Gupta, A.; Datta, R., Probing optical band gaps at the nanoscale in $NiFe_2O_4$ and $CoFe_2O_4$ epitaxial films by high resolution electron energy loss spectroscopy. *Journal of Applied Physics* **2014,** *116* (10), 103505.

Jung, H. J.; Dasgupta, N. P.; Van Stockum, P. B.; Koh, A. L.; Sinclair, R.; Prinz, F. B., Spatial Variation of Available Electronic Excitations within Individual Quantum Dots. *Nano Letters* **2013,** *13* (2), 716-721.

Zhan, W.; Venkatachalapathy, V.; Aarholt, T.; Kuznetsov, A. Y.; Prytz, Ø., Band gap maps beyond the delocalization limit: correlation between optical band gaps and plasmon energies at the nanoscale. *Scientific Reports* **2018,** *8* (1), 848.

Erni, R.; Browning, N. D., Quantification of the size-dependent energy gap of individual CdSe quantum dots by valence electron energy-loss spectroscopy. *Ultramicroscopy* **2007,** *107* (2), 267-273.

Park, J.; Heo, S.; Chung, J.-G.; Kim, H.; Lee, H.; Kim, K.; Park, G.-S., Bandgap measurement of thin dielectric films using monochromated STEM-EELS. *Ultramicroscopy* **2009,** *109* (9), 1183-1188.

Deitz, J. I.; Karki, S.; Marsillac, S. X.; Grassman, T. J.; McComb, D. W., Bandgap profiling in CIGS solar cells via valence electron energy-loss spectroscopy. *Journal of Applied Physics* **2018,** *123* (11), 115703.

Gu, L.; Srot, V.; Sigle, W.; Koch, C.; van Aken, P.; Scholz, F.; Thapa, S. B.; Kirchner, C.; Jetter, M.; Rühle, M., Band-gap measurements of direct and indirect semiconductors using monochromated electrons. *Physical Review B* **2007,** *75* (19), 195214.

Erni, R., On the validity of the Čerenkov limit as a criterion for precise band gap measurements by VEELS. *Ultramicroscopy* **2016,** *160*, 80-83.

Lazar, S.; Botton, G. A.; Wu, M. Y.; Tichelaar, F. D.; Zandbergen, H. W., Materials science applications of HREELS in near edge structure analysis and low-energy loss spectroscopy. *Ultramicroscopy* **2003,** *96* (3), 535-546.

Schamm, S.; Zanchi, G., Study of the dielectric properties near the band gap by VEELS: gap measurement in bulk materials. *Ultramicroscopy* **2003,** *96* (3), 559-564.

Rez, P.; Aoki, T.; March, K.; Gur, D.; Krivanek, O. L.; Dellby, N.; Lovejoy, T. C.; Wolf, S. G.; Cohen, H., Damage-free vibrational spectroscopy of biological materials in the electron microscope. *Nature Communications* **2016,** *7*, 10945.

Lazar, S.; Botton, G. A.; Zandbergen, H. W., Enhancement of resolution in core-loss and low-loss spectroscopy in a monochromated microscope. *Ultramicroscopy* **2006,** *106* (11), 1091-1103.

Zhang, X.; Qin, J.; Xue, Y.; Yu, P.; Zhang, B.; Wang, L.; Liu, R., Effect of aspect ratio and surface defects on the photocatalytic activity of ZnO nanorods. *Scientific Reports* **2014,** *4*, 4596.

Reynolds, D. C.; Look, D. C.; Jogai, B.; Hoelscher, J. E.; Sherriff, R. E.; Harris, M. T.; Callahan, M. J., Time-resolved photoluminescence lifetime measurements of the Γ5 and Γ6 free excitons in ZnO. *Journal of Applied Physics* **2000,** *88* (4), 2152-2153.

Kamarulzaman, N.; Kasim, M. F.; Rusdi, R., Band Gap Narrowing and Widening of ZnO Nanostructures and Doped Materials. *Nanoscale Research Letters* **2015,** *10* (1), 346.

Debanath, M. K.; Karmakar, S., Study of blueshift of optical band gap in zinc oxide (ZnO) nanoparticles prepared by low-temperature wet chemical method. *Materials Letters* **2013,** *111*, 116-119.

Arakha, M.; Roy, J.; Nayak, P. S.; Mallick, B.; Jha, S., Zinc oxide nanoparticle energy band gap reduction triggers the oxidative stress resulting into autophagy-mediated apoptotic cell death. *Free Radical Biology and Medicine* **2017,** *110*, 42-53.

Zhan, W.; Granerød, C. S.; Venkatachalapathy, V.; Johansen, K. M. H.; Jensen, I. J. T.; Kuznetsov, A. Y.; Ø, P., Nanoscale mapping of optical band gaps using monochromated electron energy loss spectroscopy. *Nanotechnology* **2017,** *28* (10), 105703.

White, A. H.; Melville, W., The Decomposition of Ammonia at High Temperatures. *Journal of the American Chemical Society* **1905**, *27*, 373-386.